5-1-2013

Scaling in the immune system

Soumya Banerjee

Soumya Banerjee
Candidate

Computer Science
Department

This dissertation is approved, and it is acceptable in quality and form for publication:

Approved by the Dissertation Committee:

Melanie Moses , Chairperson

Stephanie Forrest

Alan Perelson

Terran Lane

Frederick Koster

Scaling in the Immune System

by

Soumya Banerjee

B.E., Computer Technology, Nagpur University, India, 2003

DISSERTATION

Submitted in Partial Fulfillment of the
Requirements for the Degree of

Doctor of Philosophy
Computer Science

The University of New Mexico

Albuquerque, New Mexico

May, 2013

Dedication

To my father, Tarakeswar Banerjee, for inspiring me to pursue science and making me fall in love with it, showing me the beauty that lies in mathematics, teaching me how to be a good human being as well as so many other things about life. To my mother-in-law, Dr. Clarice Sonali Ghose, for her encouragement and inspiration. To my father-in-law, Dr. Sushil Ghose, for reminding me that there are things more important than science (like cricket). To my teacher, Ms. Achala Satsangi, for making us realize that science can be so much fun and for being the most inspirational and devoted teacher I have ever had in my life. To my wife, Joyeeta Ghose, for her constant support, encouragement and love. Finally to my mother, Kalyani Banerjee, for raising me to be a good human being, inculcating great values in me, inspiring me to pursue my higher studies, constantly encouraging me to excel in life, and for bringing me into this world. Vande Mataram.

"Where the mind is without fear and the head is held high" – Rabindranath Tagore

Acknowledgments

I would like to thank my advisor, Dr. Melanie Moses for her guidance throughout my PhD program. I shall always be indebted to her for giving me the opportunity to fulfill a long cherished dream and having faith in my abilities. I would also like to thank Dr. Stephanie Forrest who first introduced me to the wonder of immunocomputing. Thanks are due to Dr. Frederick Koster for teaching me so much about immunology; every discussion that we had filled me with wonder about the immune system. I am indebted to Dr. Alan Perelson for giving me the opportunity to work closely with him at the Los Alamos National Laboratory and guiding me through the process of mathematical modelling of immune systems. I want to thank Dr. Terran Lane for assisting me with the machine learning aspects of my research. Stimulating interactions with my colleague Diane Oyen helped me understand the machine learning aspects of my research. Thanks are due to Dr. Ruy Ribeiro, Dr. Jeremie Guedj and Dr. Vitaly Ganusov for their guidance and feedback on my work. Finally, I want to thank all the members of the Scalenet lab at UNM, especially Joshua Hecker, Kimberly Kanigel-Winner and Kenneth Letendre, for their constructive comments on my work and years of engaging discussions.

Scaling in the Immune System

by

Soumya Banerjee

B.E., Computer Technology, Nagpur University, India, 2003

Ph.D., Computer Science, University of New Mexico, 2013

Abstract

How different is the immune system in a human from that of a mouse? Do pathogens replicate at the same rate in different species? Answers to these questions have impact on human health since multi-host pathogens that jump from animals to humans affect millions worldwide.

It is not known how rates of immune response and viral dynamics vary from species to species and how they depend on species body size. Metabolic scaling theory predicts that intracellular processes will be slower in larger animals since cellular metabolic rates are slower. We test how rates of pathogenesis and immune system response rates depend on species body size.

We hypothesize that immune response rates are invariant with body size. Our work suggests how the physical architecture of the immune system and chemical signals within it may lead to nearly scale-invariant immune search and response. We fit mathematical models to experimental West Nile Virus (WNV, a multi-host pathogen) infection data and investigate how model parameters characterizing the pathogen and the immune response change with respect to animal mass.

Phylogeny also affects pathogenesis and immune response. We use a hierarchical Bayesian model, that incorporates phylogeny, to test hypotheses about the role of mass and phylogeny on pathogen replication and immune response. We observe that:

1. Hierarchical models (informed by phylogeny) make more accurate predictions of experimental data and more realistic estimates of biologically relevant parameters characterizing WNV infection.

2. Rates of WNV production decline with species body mass, modified by a phylogenetic influence.

Our work is the first to systematically explore the role of host body mass in pathogenesis using mathematical models and empirical data. We investigate the complex interplay between the physical structure of the immune system and host body mass in determining immune response. The modeling strategies and tools outlined here are likely to be applicable to modeling of other multi-host pathogens. This work could also be extended to understand how drug and vaccine efficacy in humans may systematically differ from that in model organisms like mice, in which most initial experimental studies are conducted.

Contents

List of Figures

List of Tables

Glossary

WNV	West Nile Virus.
AIS	Artificial immune system.
CTL	Cytotoxic T-Lymphocyte.
LN	Lymph node.
TCL	Target cell limited model.
AIR	Adaptive immune response model.
ODE	Ordinary Differential Equations.
ABM	Agent Based Model.
MCMC	Markov Chain Monte Carlo.

Chapter 1

Introduction

Many emerging pathogens infect multiple host species [8], and multi-host pathogens may have very different dynamics in different species [9]. Zoonotic diseases that jump the species barrier from animals to humans cause 2.5 billion cases of human illness and 2.7 million human deaths per year [10]. Many emerging diseases are zoonotic in origin.

Understanding how quickly pathogens replicate and how quickly the immune system responds is important for predicting the epidemic spread of emerging pathogens, many of which are zoonotic. While host pathogen interactions have been studied qualitatively using mathematical models, it is not known how the parameters characterizing the immune response and pathogen replication rates change from species to species. Emerging zoonotic diseases originate from species that differ in body size, e.g. birds in avian influenza and cattle in BSE (Bovine Spongiform Encephalopathy). Thus it is important to understand how body size affects immune response and pathogenesis.

Body size can affect pathogenesis in two ways:

1. Host metabolism constrains energy delivery to cells [11, 12] and could influence rates of pathogen replication and immune response rates [6]. The metabolic rate of each cell is constrained by the rate at which nutrients and oxygen are supplied by the cardio-vascular network. The rate at which this network supplies nutrients to each cell (R_{cell}) scales as the body mass (M) raised to an exponent of -1/4: $R_{cell} \propto M^{-1/4}$ such that individual cellular metabolic rates decrease as the body mass increases [11, 12]. This relationship holds over an incredible diversity of body sizes, from 10^{-13} g (microbes) to 10^{8} g (whales). Many biological rates, such as heart rates and reproductive rates, scale as $M^{-1/4}$, while many times such as blood circulation times and life times, scale as $M^{1/4}$ (times) [11].

   Cellular metabolic rate dictates the pace of many biological processes [12]. Cellular metabolism could affect immune system search times by reducing movement and proliferation of immune cells [6]. Rates of DNA and protein synthesis also depend on the cellular metabolic rate and could influence the rate at which pathogens replicate inside infected cells [9]. Using mathematical models and experimental data, we test whether viral replication and immune response varies with species mass. We use West Nile Virus (WNV) as a model pathogen for our studies because it is a generalist pathogen that infects many species in different taxonomic groups and with a range of body sizes.

2. An effective immune response requires efficient detection of pathogens that may be initially localized. The detection of small amounts of pathogen is harder in larger animals due to larger physical spaces. We hypothesize that the immune system is capable of nearly scale-invariant detection and response, i.e. rates of immune response and time taken by the immune system to detect and respond to pathogens do not scale appreciably with host body size. We suggest how: a) the physical architecture of the immune system, comprised of anatomical structures called lymph nodes (that faciliate recognition of pathogen by

immune system cells), and b) chemical signalling within the immune system, guiding immune system cells to sites of infection, enable efficient and nearly scale-invariant detection and response.

WNV pathogenesis also depends on phylogeny, e.g. Passerine species sustain more viremia than non-Passerine species [5]. Hence phylogeny is expected to affect immune response and pathogen replication rates. Viral dynamics may be similar in related species. Modeling techniques that take advantage of relatedness of infected species may produce more accurate results. We aim to incorporate phylogenetic hierarchy to make better estimates of biologically relevant quantities for WNV.

Hierarchical Bayesian models enable modelers to encapsulate knowledge about the underlying biology as priors. Hierarchical models also pool information across disparate individuals from different groups and are well suited for cases where there are a limited number of observations from several individuals. Suitable priors in a hierarchical Bayesian framework can help reduce variance of parameter estimates [13]. A model that incorporates the hierarchal nature of phylogeny and encodes this information as priors in a hierarchical Bayesian model may enable more accurate estimates of parameters characterizing WNV infection.

Hierarchical Bayesian models have been used in image processing [14], ecological modeling [15] and climate modeling [16]. Bayesian non-linear mixed effects models with a single level of hierarchy have been applied to modeling of the within-host response to HIV [17, 18] and influenza [19]. Multilevel data fitting approaches and Bayesian frameworks are expected to be helpful to modeling within-host viral dynamics [20]. However to the best of our knowledge, Bayesian non-linear mixed effects models with multiple levels of hierarchy have not been applied to within-host modeling. Mathematical models that combine within-host experimental data from multiple species, such as the ones presented here, may also be useful in studying other zoonotic diseases and help increase our understanding of these diseases.

Our goals are:

1. to test how the physical architecture of the immune system and chemical signals within it affect immune response times. This is investigated in **Chapters 3** and **4**.

2. to characterize dynamics of WNV in mice using ordinary differential equation models. This is explored in **Chapter 5**.

3. to test if a hierarchical Bayesian model that incorporates phylogeny allows more refined predictions. This is explored in **Chapter 6**.

4. to apply the hierarchical Bayesian model to test the effect of species mass and phylogeny on rates of pathogen replication and immune response in WNV. This is investigated in **Chapter 7**.

1.1 Background on West Nile Virus

We use WNV as a model pathogen for our studies because it is a generalist pathogen that infects many species in different taxonomic groups and with a range of body sizes. WNV is a neurotropic flavivirus that has emerged globally as a significant cause of viral encephalitis. WNV is maintained in an enzootic cycle between mosquitoes and birds [21] but can also infect and cause disease in many other vertebrates including humans. Following its introduction into the United States in 1999, WNV spread rapidly across the North American continent in only four years and more recently has been reported in Mexico, South America, and the Caribbean [22, 23, 24]. Although vaccines are available for animal use, no vaccines or specific therapies for WNV are currently approved for humans [25].

WNV is an enveloped virus with a single-stranded, positive sense, 11-kb RNA genome [25]. WNV is cytopathic and initially infects epidermal Langerhans cells, which then migrate to the draining lymph node and infect macrophages [25]. From the draining lymph node, WNV spreads to the spleen, kidney, and spinal cord and ultimately breaches the blood-brain barrier to infect neurons [25]. The standard pattern of WNV infection in mice is characterized by an initial exponential growth of virus that peaks around 3 to 4 days post infection (DPI), followed by an exponential decline until that leads to undetectable levels of virus by 6 to 8 DPI.

WNV infects a large number of species across different taxonomic groups. This allows us to test the effects of animal body size on pathogen replication and immune response. We focus on data from a study which experimentally infected birds with the same strain of WNV (WNV NY99-6480). The species infected range from 3 gm sparrows to 3 kg geese. Komar et al [5] experimentally infected 25 species of birds with WNV NY99-6480 and took daily measurements of the concentration of infective virions in blood (viremia) over the course of infection. Viremia was reported in plaque forming units (PFU, a measure of the number of infectious virions) over a span of at most 7 days post infection.

The order Passeriforme includes more than half of all bird species. The experimental infection study infected 10 Passerine species and 15 non-Passerine species. The Passerine species were house finches, house sparrows, red winged blackbirds, blue jays, American robins, European starlings, common grackles, black-billed magpies, fish crows and American crows. WNV is exceptionally viremic in corvid species (a family within the order Passeriforme). The corvid species in the study were blue jays, black-billed magpies, fish crows and American crows. The number of individuals infected per species ranged from 1 (American coots) to 8 (American crows).

The experimental infection study included data on 87 individual birds belonging to 25 distinct species. Of the 87 individuals infected, 26 succumbed to infection.

With the exception of one individual (a non-Passerine ring billed gull), all mortality was in Passerine species, primarily corvids.

1.2 Contributions and Organization

The remainder of the dissertation is divided into 7 chapters. The contributions of these chapters are summarized below:

Chapter 2. This chapter outlines our computational approach, the unique computational challenges in this work and our solutions.

Chapter 3. An effective immune response requires efficient detection of pathogens that may be initially localized. The detection of pathogens and response against them is hypothesized to be more challenging in larger animals because the search occurs in a larger physical space. We hypothesize that immune response rates and times do not scale appreciably with host body size. This work suggests how the physical architecture of the immune system may lead to nearly scale-invariant immune search and response. It also proposes an architecture for an engineered distributed system (a multi-robot control system) that is inspired by the physical architecture of the immune system [26]. This chapter was published by Soumya Banerjee and Melanie Moses in *Swarm Intelligence* in 2010 [26].

Chapter 4. Rapid search is crucial for an effective immune response: Immune system cells must find, identify and neutralize pathogens before those pathogens replicate in sufficient numbers to cause disease or death. The adaptive immune system has a small number of pathogen-specific cells that must search for and neutralize initially localized pathogens in a very large tissue space. The immune system uses information signals to accomplish this search quickly. This work

suggests how chemical signals in the immune system accelerate this search. We show that search times are reduced by over an order of magnitude in mice and over two orders of magnitude in humans, suggesting that these signals play an important role in the immune response, especially in larger animals [27]. This chapter was published by Soumya Banerjee, Drew Levin, Melanie Moses, Frederick Koster and Stephanie Forrest in the 10th International Conference on Artificial Immune Systems in 2011 [27].

Chapter 5. The qualitative dynamics of WNV have been best studied experimentally in mice. This chapter describes a method to predict biologically relevant quantities for WNV infection in mice with the intention of gaining a quantitative understanding of WNV dynamics. Our novelty lies in uniquely combining experimental data from knockout and wildtype mice using a succession of increasingly complex models. Despite large uncertainty in imposed bounds on model parameters, our analysis yields tight estimates of a variety of biologically relevant quantities that characterize WNV infection in mice [28]. Our method could be more broadly applicable to modeling of other emerging pathogens with large parameter uncertainty. This chapter was co-authored by Jeremie Guedj, Ruy Ribeiro, Melanie Moses and Alan S. Perelson and is being prepared for submission [28].

Chapter 6. As a first step towards developing a model of WNV dynamics in different species, this chapter develops a novel multi-level hierarchical Bayesian model that incorporates phylogeny. In order to control the effect of noisy data and model uncertainty, this chapter uses a known simple model to generate simulated viremia data with varying amounts of noise. We then infer differential equation model parameters using the hierarchical model. The accuracy of the hierarchical model is calculated by comparing the inferred parameter estimates to the actual parameter values (ground truth from known data). We find

that our multi-level model (with prior information about differences between species) can generate more accurate estimates under some circumstances.

Chapter 7. This chapter extends the multi-level hierarchical model from Chapter 6 by introducing a more realistic mathematical model of viral dynamics and applying it to actual experimental data. We find that the multi-level model produces more accurate predictions of viremia and more realistic estimates of parameters. It also uncovers systematic differences in biologically relevant parameters with species mass and phylogeny.

Chapter 8. This chapter concludes the dissertation by outlining the scaling relationships for rates of pathogen replication and the scale-invariance of immune response rates and times. It also discusses implications for spread of zoonotic diseases and design of human-engineered distributed systems. The chapter also points out promising avenues for future investigations.

Chapter 2

Computational Approach

We apply tools and approaches from complex systems and computer science to study the immune system. An immune response is characterized by non-linear and dynamic interactions between the pathogen and the host immune system. We use both spatially-explicit agent based models (ABM) and computationally tractable ordinary differential equation (ODE) models for simulating the immune system. In this chapter, we outline all the computational techniques used, challenges faced and the mathematical and engineering solutions we used to address those challenges.

2.1 Agent-Based Models

Chapter 3 uses the CyCells [29, 30] ABM platform to simulate the dynamics of trafficking of WNV to the lymph node. The CyCells [29, 30] modeling tool explicitly represents healthy cells, infected cells, and immune system cells, and represents various chemicals released by the immune system as concentrations. The simulation is conducted in a 3-dimensional cubic compartment.

2.2 Differential Equation Models

Chapters 5 to 7 use ODEs to simulate replication of WNV and the host immune response to WNV. ODE models ignore space by assuming that all components are well-mixed but have the advantage of being computationally tractable. The ODEs describing our viral kinetic models were solved numerically using programs written in Matlab [31] and Berkeley Madonna [32]. We used the Runge-Kutta 4 method of integration. The curve-fitting method implemented in Matlab and also available in Berkeley Madonna uses nonlinear least-squares regression that minimizes the sum of the squared residuals between experimental data and ODE model predicted values.

We use two different ODE models to represent dynamics of WNV replication and host immune response:

1. Target cell limited model. The target cell limited model assumes that the concentration of virus reaches a peak and then declines when few susceptible target cells remain. This model is represented by Eqs. 5.1 - 5.4.

2. Adaptive immune response model. The adaptive immune response model assumes that an adaptive antibody response causes the decline of virus concentration after a peak. This model is represented by Eqs. 5.7 - 5.11.

2.3 Hierarchical Bayesian models and Markov Chain Monte Carlo

We use hierarchical Bayesian models to delineate the contribution of species mass and phylogeny to WNV replication and the response of the host to WNV. We use Markov chain Monte Carlo (MCMC) to draw samples from the distributions characterizing

our ODE model parameters since they do not have an analytic closed-form.

The Bayesian inference approach can be described as follows. Assume that a model (in our case a differential equation model describing how virus concentration changes over time in serum) is represented by parameters Θ. The Bayesian approach allows us to include prior knowledge about model parameters in a systematic fashion. If we have information about Θ (for e.g., from experimental evidence) which needs to be incorporated in our analysis, this is represented as a prior probability distribution $P(\Theta)$. Bayes Rule allows us to incorporate the prior knowledge about parameters, $P(\Theta)$, and experimental data, D, to derive a posterior distribution of parameters:

$$P(\Theta|D) = \frac{P(D|\Theta) \cdot P(\Theta)}{P(D)} \tag{2.1}$$

The normalizing constant is chosen such that the posterior distribution, $P(\Theta|D)$, integrates to 1, i.e. $P(D) = \int P(D|\Theta) \cdot P(\Theta) \mathrm{d}\Theta$. We then use MCMC to numerically integrate the terms in Eq. 2.1.

2.3.1 Metropolis-Hastings Sampler

We use two popular MCMC algorithms known as the Metropolis-Hastings sampler and the Gibbs sampler. We use these algorithms to sample from the posterior distribution $P(\Theta|D)$. Let $\Theta^{(t)}$ represent the state of the Markov chain at iteration t of the algorithm. The Metropolis-Hastings sampler uses a proposal distribution $q(\Theta|\Theta^{(t-1)})$ to generate a candidate point, Θ^*, that is conditioned on the previous state of the sampler, $\Theta^{(t-1)}$. In the next step, the algorithm either accepts or rejects the candidate point based on an acceptance probability:

$$\alpha = \min(1, \frac{P(\Theta^*)}{P(\Theta^{(t-1)})} \cdot \frac{q(\Theta^{(t-1)}|\Theta^*)}{q(\Theta^*|\Theta^{(t-1)})}) \tag{2.2}$$

The Metropolis-Hastings algorithm is as follows:

1. Set $t = 1$
2. Generate an initial value u, and set $\Theta^{(t)} = u$
3. Repeat

   $t = t + 1$

   Generate a candidate Θ^* from the proposal distribution $q(\Theta|\Theta^{(t-1)})$

   Evaluate the probability of acceptance, $\alpha = \min(1, \frac{P(\Theta^*)}{P(\Theta^{(t-1)})} \cdot \frac{q(\Theta^{(t-1)}|\Theta^*)}{q(\Theta^*|\Theta^{(t-1)})})$

   Generate a x from a Uniform(0,1) distribution

   If $x \leq \alpha$, accept the candidate solution and set $\Theta^t = \Theta^*$, else set $\Theta^t = \Theta^{(t-1)}$
4. Until $t =$ required number of iterations

The Metropolis-Hastings sampler has the advantage of not requiring knowledge of the normalizing constant, $P(D)$. In our case the parameter Θ is multi-variate and has different components corresponding to the different ODE model parameters. We accept or reject the candidate solution involving all components as a block simultaneously. This is known as a block-wise updating scheme. A component-wise updating scheme updates each component in turn and independently of each other.

2.3.2 Gibbs Sampler

The Gibbs sampler is an algorithm in which all samples are accepted and hence is computationally more efficient than the Metropolis-Hastings sampler. However,

the Gibbs sampler can only be applied in the case when we know the full conditional distribution of each component of the parameter Θ conditioned on all other components.

As an illustrative example, we show the workings of the Gibbs sampler for the joint two-component distribution $g(\theta_1, \theta_2)$. The Gibbs sampler can be used if we can derive the distribution of each component conditioned on the other, i.e. in this case the conditional distributions $g(\theta_1|\theta_2 = \theta_2^{(t)})$ and $g(\theta_2|\theta_1 = \theta_1^{(t)})$. The Gibbs sampler for the case of two-components is as follows:

1. Set $t = 1$

2. Generate an initial value $u = (u_1, u_2)$, and set $\Theta^{(t)} = u$

3. Repeat

   $t = t + 1$

   Sample $\theta_1^{(t)}$ from the conditional distribution $g(\theta_1|\theta_2 = \theta_2^{(t-1)})$

   Sample $\theta_2^{(t)}$ from the conditional distribution $g(\theta_2|\theta_1 = \theta_1^{(t)})$

4. Until $t =$ required number of iterations

We update each component sequentially in turn (systematic-scan Gibbs sampler).

Our approach is to use the Metropolis-Hastings sampler within the Gibbs sampler; this involves using the computationally efficient Gibbs update steps whenever the full posterior conditional distributions are known and using Metropolis-Hastings acceptance steps when the full conditional distribution is not available.

2.4 Bayesian Model Assumptions

The parameters in our ODE models vary over large ranges (frequently over many orders of magnitude). Hence in order to stabilize the variance and also ensure that estimates are positive, we assumed that all ODE model parameters characterizing viral replication and immune response are lognormally distributed.

2.5 Strategies for Computational Efficiency

Investigating scaling in the immune system requires calibrating our ODE models to data from multiple species. We have data for 23 different species comprising 83 individual birds. The samplers are run for 30,000 iterations for each and every individual. Hence the complete Bayesian inference process involves millions of calls to our ODE solvers. We use a number of techniques to ensure that our computations are efficient.

1. We use the computationally efficient Gibbs update steps whenever the full posterior conditional distributions are known and use Metropolis-Hastings acceptance steps when the full conditional distribution is not available. The posterior distribution of ODE parameters at the individual level of the hierarchical Bayesian model does not have an analytic closed-form solution. Hence we use the Metropolis-Hastings sampler to update the the parameters at the individual level. At all other levels of the hierarchical Bayesian model, we are able to derive the full conditional distributions and hence we use Gibbs update steps.

2. ODE solvers use error tolerance thresholds to calculate how much a solution changes from one step of the solver to the next and to determine when to

stop. The two ways of determining error are relative error and absolute error. Smaller error thresholds lead to more accurate solutions but also lead to more solver steps increasing execution time. Hence these error thresholds represent tradeoffs between accuracy and computational efficiency. We experimented with different values of error tolerance thresholds and ultimately chose 1e-3 for the relative error threshold and 1e-6 for the absolute error threshold.

3. Inference via MCMC is a sequential iterative process where the computations in each step depend on results in the previous step. This sequential procedure increases the computational complexity of our programs. However there are computations within an iteration that can be efficiently parallelized. In our case, each iteration of the MCMC procedure generates candidate solutions which are then passed to the different solvers representing different individual birds. The computation done by the ODE solver for each individual is independent of computations done for other individuals. Hence we parallelize these simultaneous ODE calls by using the MATLAB construct for parallel for-loops (parfor), which runs these on multiple cores of the same machine.

4. Finally, the choice of dispersion of the proposal distribution represents tradeoffs between thoroughness of search through the parameter space and computational efficiency. If the variance of the proposal distribution is very large, then the MCMC algorithm can sample from far away regions in the parameter space. However a large proportion of proposed moves will also be rejected since they are likely to be in regions that represent infeasible solutions. Similarly if the variance of the proposal distribution is very small, then the sampler would move around the parameter space slowly which would lead to computational inefficiency. We experimented with different values of variance of the proposal distribution and chose a value of 0.01 for the standard deviation on the log scale.

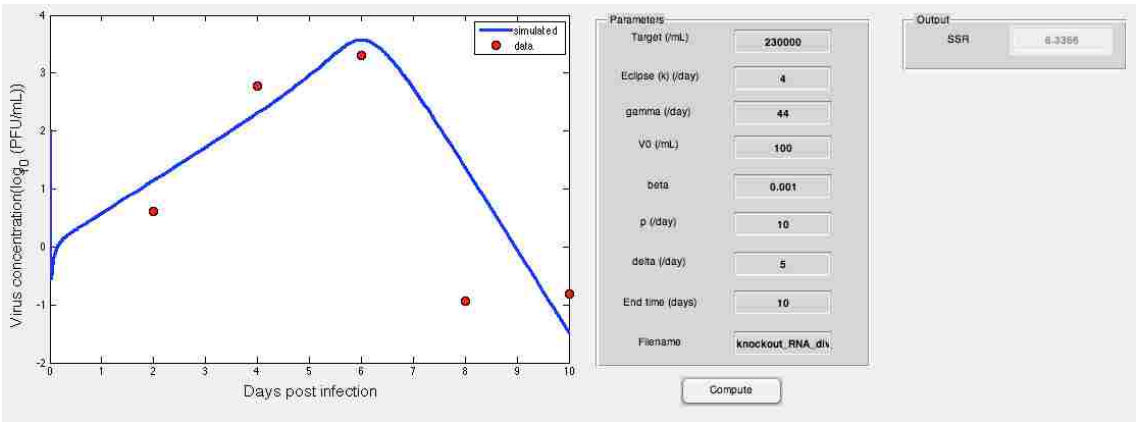

Figure 2.1: Screenshot of graphical user interface to solve ODEs and plot model fits to data.

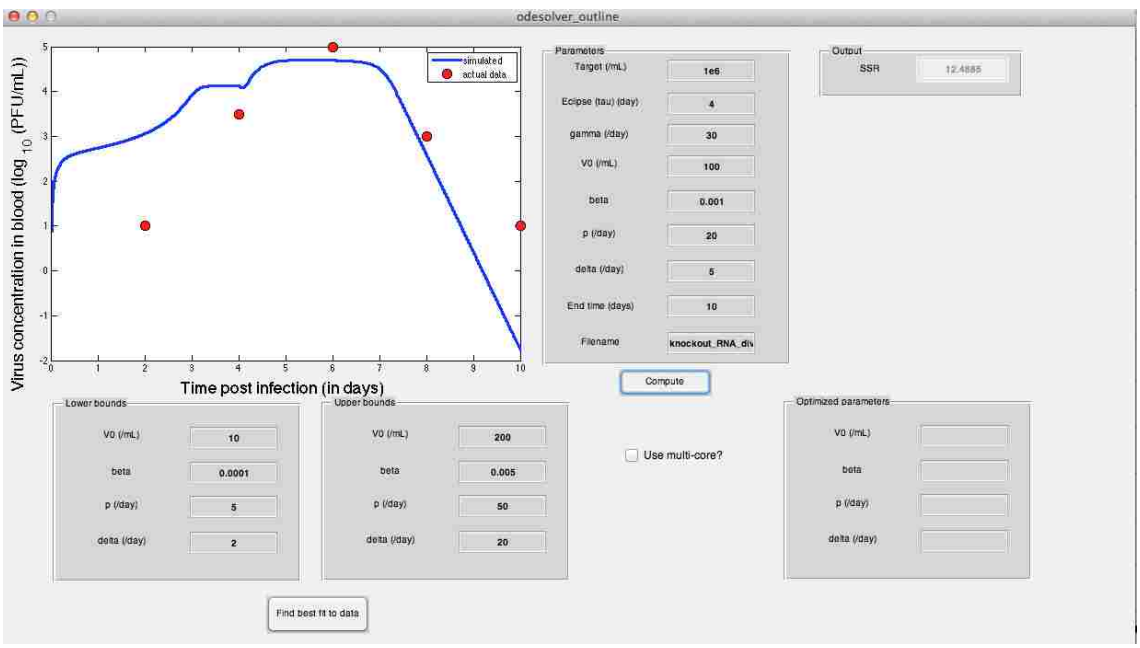

Figure 2.2: Screenshot of tool to generate best-fit ODE parameter estimates while being calibrated to experimental data.

2.6 Tools for Analysis and Modeling

We created a number of tools to facilitate our analysis of data and model results that have been made available online [33]. We expect these tools to be helpful to other researchers in the modeling community. Some of the tools we developed are:

1. We implemented graphical user interfaces in MATLAB that helped us solve ODEs and plot model fits to data. This tool helped us visualize the effects of changing ODE parameters on model fit to data. A screenshot of the interface is shown in Fig. 2.1.

2. We developed a tool that generated best-fit ODE parameter estimates while being calibrated to experimental data. This tool has a graphical user interface which modelers can use to input different initial guesses and parameters for solvers. The tool helped us investigate the effects of different initial guesses on best-fit model parameters. A screenshot of the tool is shown in Fig. 2.2.

3. Finally, the code implementing the hierarchical Bayesian models was made efficient, extendable and modular so that we could: a) add an arbitrary number of species into the model, b) investigate different levels of hierarchy, and c) investigate different hierarchical groupings of species. This necessitated the use of special data structures. The choice of data structures and implementation was also influenced by the unique constraints imposed by parallelizing the code to run on multiple cores.

Chapter 3

Scale invariance of immune system response rates and times

3.1 Abstract

Most biological rates and times decrease systematically with increasing organism body size. We use an ordinary differential equation (ODE) model of West Nile Virus in birds to show that pathogen replication rates decline with host body size, but natural immune system (NIS) response rates do not change systematically with body size. The *scale invariant detection and response* of the NIS is surprising since the NIS has to search for small quantities of pathogens through larger physical spaces in larger organisms, and also respond by producing larger absolute quantities of antibody in larger organisms. We hypothesize that the NIS has evolved an architecture to efficiently neutralize pathogens. We investigate three different hypothesized NIS architectures using an Agent Based Model (ABM). We find that a sub-modular NIS architecture, in which lymph node number and size both increase sublinearly with body size, efficiently balances the tradeoff between local pathogen detection and

global response. This leads to nearly scale-invariant detection and response consistent with experimental data. Similar to the NIS, physical space and resources are also important constraints on distributed systems, for example low-powered robots connected by short-range wireless communication. We show that the sub-modular design principles of the NIS can be applied to problems such as distributed robot control to efficiently balance the tradeoff between local search for a solution and global response or proliferation of the solution. By demonstrating that the lymphatic network of the NIS efficiently balances local and global communication, we suggest a new approach for Artificial Immune Systems (AIS) that uses a sub-modular architecture to facilitate distributed search. This chapter was co-authored by Melanie E. Moses (Department of Computer Science, University of New Mexico). It was published in *Swarm Intelligence*, Volume 4, 2010, pp. 301-318.

3.2 Introduction

Many emerging pathogens infect multiple host species [8], and multi-host pathogens may have very different dynamics in different host species [9]. Understanding how quickly pathogens replicate and how quickly the natural immune system (NIS) responds is important for predicting the epidemic spread of emerging pathogens. We show that pathogen replication rates decline systematically with increasing host body size, but NIS response times do not increase significantly. We discuss how the decentralized architecture of the immune system facilitates parallel search, enabling NIS response times that do not increase substantially with body size.

The NIS solves a search problem in both physical space and antigen space. For the pathogens considered here, the length of the search is determined by the time it takes for a cognate B cell to encounter antigen. Encounter times depend on the size

of the physical space in which the search occurs. This is a difficult search problem since very rare antigen specific NIS cells have to search for small quantities of antigen throughout the body. For example, a mosquito injects 10^5 live virus particles into a vertebrate host that has billions or trillions of cells [34]. The research we describe here suggests that the time for the immune system to detect and neutralize the pathogen is nearly independent of the size of the organism. We call this *scale-invariant detection and response*.

This is counter-intuitive, since if we inject a sparrow and a horse with the same amount of pathogen, the immune system of the horse has to search a much larger physical space to find the pathogen, compared to the sparrow. This research models how different potential architectures of the lymphatic network enable the NIS to mount an effective immune response that neutralizes pathogens in time that is independent of host body size. Physical space and resource limitations can also constrain Artificial Immune Systems (AIS). Our research shows how the optimal design of such AIS can be informed by architectural strategies employed by the NIS.

In addition to the immune system having to search larger spaces in larger organisms, larger body size may be expected to slow immune system response times because the metabolic rate of cells is lower in larger species [12]. The metabolic rate of each cell is constrained by the rate at which nutrients and oxygen are supplied by the cardio-vascular network. The rate at which this network supplies nutrients to each cell (R_{cell}) scales as the body mass (M) raised to an exponent of -1/4: $R_{cell} \propto M^{-1/4}$ such that individual cellular metabolic rates decrease as the body mass increases [11, 12]. The metabolic rate of a cell dictates the pace of many biological processes [12]. This could affect NIS search times by reducing movement and proliferation of immune cells [6]. Rates of DNA and protein synthesis are also dependent on the cellular metabolic rate and could influence the rate at which pathogens replicate inside infected cells [9].

Table 3.1: Four scaling hypotheses of pathogen replication and immune system response rate [6]

H1: Pathogen replication rate $\propto M^0$ NIS search time $\propto M^0$	H2: Pathogen replication rate $\propto M^{-1/4}$ NIS search time $\propto M^0$
H3: Pathogen replication rate $\propto M^0$ NIS search time $\propto M^{-1/4}$	H4: Pathogen replication rate $\propto M^{-1/4}$ NIS search time $\propto M^{-1/4}$

The possibilities that NIS cells and pathogens may move and proliferate at speeds independent of mass ($\propto M^0$) or proportional to cellular metabolic rate ($\propto M^{-1/4}$) lead to four hypotheses, shown in Table 3.1, as originally proposed by Wiegel and Perelson [6].

We combine an ordinary differential equation model, an Agent Based Model (ABM) and empirical results from experimental infection studies on West Nile Virus (WNV) [1, 2, 3] in what is the first test that we are aware of, examining the effects of body size on pathogen replication and immune system response rates. Our results are consistent with H2: pathogen replication rate $\propto M^{-1/4}$ and NIS rates $\propto M^0$.

The remainder of the paper is organized as follows: Section 3.3 gives an introduction to the relevant immunology; our statistical methods are outlined in Section 3.4; Section 3.5 discusses an ordinary differential equation model of pathogen growth and immune response; Section 3.6 discusses the difficulties faced by the NIS in searching space; we use an ABM to derive scaling relations for NIS cell detection and migration times in Section 3.7; the results are summarized in Section 3.8; Section 3.9 explains how a sub-modular NIS architecture balances fast search times and fast communication to recruit NIS cells, leading to scale invariant detection; Section 3.10 discusses the applications and implications for this work in distributed AIS using an example of multi-robot control, and lastly we make concluding remarks in Section 3.11.

3.3 A Brief introduction to the immune system

The NIS has two main components: the innate immune system and the adaptive immune system. The innate immune system is the first line of defense of an organism and consists of complement proteins, macrophages and dendritic cells (DC) [35]. The adaptive immune system consists of T helper cells, B cells and cytotoxic T cells. The area of tissue that drains into a lymph node (LN) is called its draining region (DR). The lymphatic system collects extra-cellular fluid called lymph from tissues and returns it to blood [35]. DCs sample the tissue in DRs for pathogens, and upon encountering them, migrate to the nearest LN T cell area to present antigen to T helper cells. Cognate T helper cells specific to a particular pathogen are very rare (1 in 10^6 NIS cells) [36]. Upon recognizing cognate antigen on DCs, T helper cells proliferate and build up a clonal population in a process called clonal expansion. While proliferating, T helper cells also migrate to the LN B cell area to activate B cells. Cognate B cells specific to a particular pathogen are also very rare. They need to recognize cognate antigen on follicular dendritic cells and also need stimulation from cognate T helper cells. After recognition, cognate B cells undergo clonal expansion and differentiate into antibody-secreting plasma cells [35].

This difficult search through the large physical space is facilitated by infected site inflammation, chemokines and preferential expression of adhesion molecules which guide NIS cells to sites of pathogen invasion [35]. The infected site LN recruits NIS cells from other LNs and blood through high endothelial venules. We refer to the recruitment time as communication overhead between LNs. Some pathogens do not invoke all the arms of the immune system, e.g. some bacteria are efficiently eliminated by the innate immune system. We focus here on pathogens, like WNV, that elicit an antibody response. However, the arguments put forward in this paper would apply also to other pathogens that spread systemically throughout the body and evoke a cytotoxic T cell or other response (see Section 3.9).

We are interested in the physical structure of the NIS, and we hypothesize that evolutionary pressures have shaped NIS architecture to minimize the time taken to unite rare antigen-specific NIS cells with their pathogens. This requires both rapid detection of the initial pathogens and also rapid clonal expansion to produce sufficient T helper cells to activate a critical number of B cells. These B cells will then undergo clonal expansion and differentiate into antibody-secreting plasma cells. Hence this paper focuses primarily on the uptake of antigen by DCs in DR, recognition of antigen on DCs by T cells in LN, the subsequent process of clonal expansion and recruitment of B cells from other LNs.

3.4 Statistical methods

We use ordinary least squares (OLS) regression to test whether our model predictions are consistent with hypothesized scaling relationships and, where possible, biological measurements. We calculate the r^2 value, where r is the Pearson correlation coefficient and the r^2 quantifies the proportion of variation that the independent variable explains in the dependent variable. We test how empirical data from literature and results of our simulation scale with mass by taking the logarithm of both variables and doing an OLS regression. We report whether the scaling exponent is consistent with -0.25, 0, or both. We test for significance at the alpha = 0.05 level. The mean is reported after testing all log-transformed datasets for normality using the Jarque-Bera test [37].

3.5 An ordinary differential equation model for viral dynamics

A standard Ordinary Differential Equation (ODE) model was developed to observe how viral proliferation rates and immune response rates scale with body size, and model results were parameterized to empirical levels of virus in blood [38]. Data on viral proliferation was taken from studies which used the same West Nile Virus strain to experimentally infect 25 different species with body mass ranging from 0.02 kg (house finch) to 390 kg (horse), and the viral load was monitored each day in blood serum (reported in plaque forming units - a measure of the number of infectious virions) over a span of 7 days post infection (d.p.i) [1, 2, 3]. In the model, p = rate of virion production per infected cell, γ = innate immune system mediated virion clearance rate, ω = adaptive immune system proliferation rate, and t_{pv} = time to attain peak viral concentration. Equations (1) to (4) are shown below

$$\frac{dT}{dt} = -\beta TV \tag{3.1}$$

$$\frac{dI}{dt} = \beta TV - \delta I \tag{3.2}$$

$$\frac{dV}{dt} = pI - c(t)V \tag{3.3}$$

$$c(t) = \begin{cases} \gamma & , \quad t < t_{pv} \\ \gamma e^{\omega(t-t_{pv})} & , \quad t \geq t_{pv} \end{cases} \tag{3.4}$$

Target cells T are infected at a rate proportional to the product of their population size and the population size of virions V, with a constant of proportionality β. The loss in the target cell population is balanced by a gain in the infected cell population. Infected cells I die at a rate δI. Virions are produced by infected cells at a rate p and cleared by the immune system at the rate $c(t)V$. The action of the immune

system is decomposed into an innate response (γ) before the virus concentration attains a peak, and an exponential adaptive immune response after peak due to clonal expansion characterized by a proliferation rate ω. This paper focuses on p as pathogen replication, and γ and ω as immune system response.

Empirical data show that time to peak viral concentration (t_{pv}, time between infection and peak viral concentration in blood) for WNV empirically occurs between 2 - 4 days post infection (Fig. 3.1) [1, 2, 3]. If this peak were due to target cell limitation, then we would expect t_{pv} to increase with host mass M since larger animals have more target cells. However, t_{pv} is likely to be determined by WNV specific antibodies, which have a critical role in WNV clearance [39]. If the peak is determined by a threshold presence of antibodies, then it implies that t_{pv} is determined by the time for cognate B cells to recognize antigen, proliferate and produce antibodies: $t_{pv} = t_{detect} + t_{prolif}$. Empirically, t_{pv} is independent of host mass [1]. The time t_{pv} is highly conserved, ranging only between 2 and 4 days post infection across different hosts that range in mass from 0.02 kg (house finch) to 390 kg (horses). Since there is no statistically significant relationship between t_{pv} and M (Fig. 3.1)(p-value testing significance of the slope - 0.35, 95% CI on slope - [-0.037, 0.0607]), then the data are consistent with the hypothesis that $t_{pv} \propto M^0$. Hence empirical data for WNV supports the hypothesis that NIS response rates are independent of M. One explanation that has been proposed is *preferential metabolism*, i.e. LNs are supplied energy at a rate which is independent of host body mass so that the metabolic rates of B cells and T cells in LN are independent of mass [6].

Other empirical data suggests that pathogen replication rates scale as $M^{-1/4}$ for a variety of pathogens in a variety of hosts, including WNV in birds and mammals [9]. The Cable et al study shows that times for a pathogen to cause symptoms or death is proportional to $M^{1/4}$ (where times are inverses of rates, mean exponent = 0.21, Table 1, [9]). Together, these observations reject all hypotheses in Table 3.1

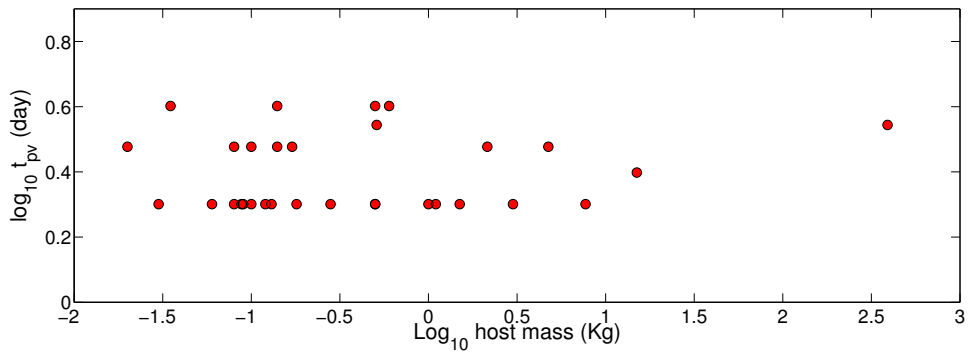

Figure 3.1: Plot of $log_{10}\ t_{pv}$ (empirically measured time between infection and peak viral concentration in blood, units of day) vs. log_{10} host body mass M. p-value testing significance of the slope = 0.35, 95% confidence interval on slope = [-0.037, 0.0607], data from [1, 2, 3]

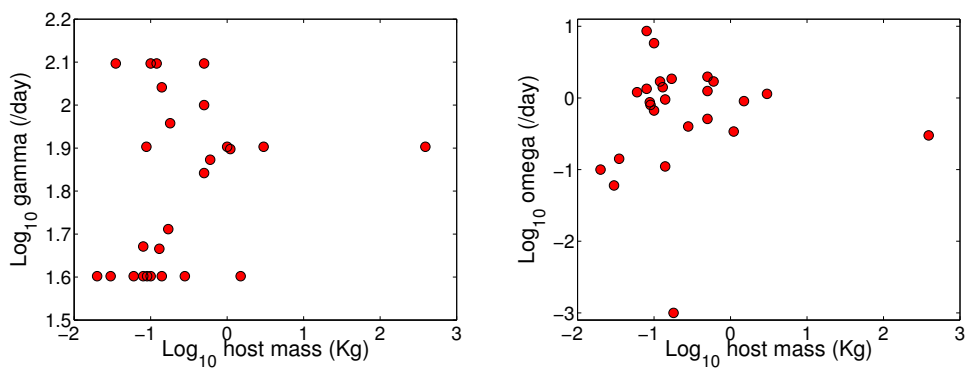

Figure 3.2: Left Panel: plot of $log_{10}\ \gamma$ (model estimated innate immune system mediated pathogen clearance rate, units of day^{-1}) vs. log_{10} host body mass M (p-value testing significance of the slope = 0.4238, 95% confidence interval on slope = [-0.04, 0.146]). Right Panel: plot of $log_{10}\ \omega$ (model estimated adaptive immune system cell proliferation rate, units of day^{-1}) vs. log_{10} host body mass M (p-value testing significance of the slope = 0.7242, 95% confidence interval on slope = [-0.347, 0.4319])

except H2: pathogen replication declines with $M^{-1/4}$ and immune response times are invariant with respect to M. Ideally we would test all four hypotheses simultaneously using the ODE model described by Equations (1) to (4). However, the ODE has too

Table 3.2: Estimated ODE model parameters for great-horned owl (where PFU is Plaque Forming Units)

$V_0\left(\frac{\text{PFU}}{\text{mL}}\right)$	$\beta\left(\frac{1}{\frac{\text{PFU}}{\text{mL}}*\text{day}}\right)$	$p\left(\frac{1}{\text{PFU}*\text{day}}\right)$	$\delta\left(\frac{1}{\text{day}}\right)$	$\gamma\left(\frac{1}{\text{day}}\right)$	$\omega\left(\frac{1}{\text{day}}\right)$	$t_{pv}\left(\frac{1}{\text{day}}\right)$
2.95	10^{-7}	524.97	1.19	91.99	2.7	3

many parameters to simultaneously test both hypotheses without overfitting the data. Since our main goal is to determine the scaling of the NIS response rates and times, we fit the data by choosing initial parameter estimates consistent with pathogen replication rates scaling as $M^{-1/4}$, and then fit the model to the data.

The ODE model was fit to the viral load data for each of 25 species [1, 2, 3] for days 1 - 7 and the model parameters were estimated using non-linear least squares regression. The Berkeley Madonna® [32] software package was used to generate the fits and we assigned the parameter value to the mass of the species to do an OLS regression. The scaling relations found were: $p \propto M^{-0.29}$ (the predicted exponent of -0.25 is in the 95% CI, $r^2 = 0.31$, p-value testing significance of slope = 0.0038). The innate immune system mediated pathogen clearance rate (measured day^{-1}, γ) and adaptive immune system cell proliferation rate (measured day^{-1}, ω) were independent of host mass M (Fig. 3.2)(p-values testing significance of the slope - 0.4238 and 0.7242 respectively, 95% CI on slope - [-0.04, 0.146] and [-0.347,0.4319] respectively). A sample parameter estimate and model prediction is shown in Table 3.2 and Fig. 3.3.

These findings from our ODE model and empirical data are consistent with hypothesis H2: pathogen replication rates decline in larger hosts, but immune response is independent of host mass (scale-invariant detection and response). This raises the question: what mechanisms make NIS rates independent of host body mass and metabolism? The problem of slower metabolism in larger hosts can be circumvented

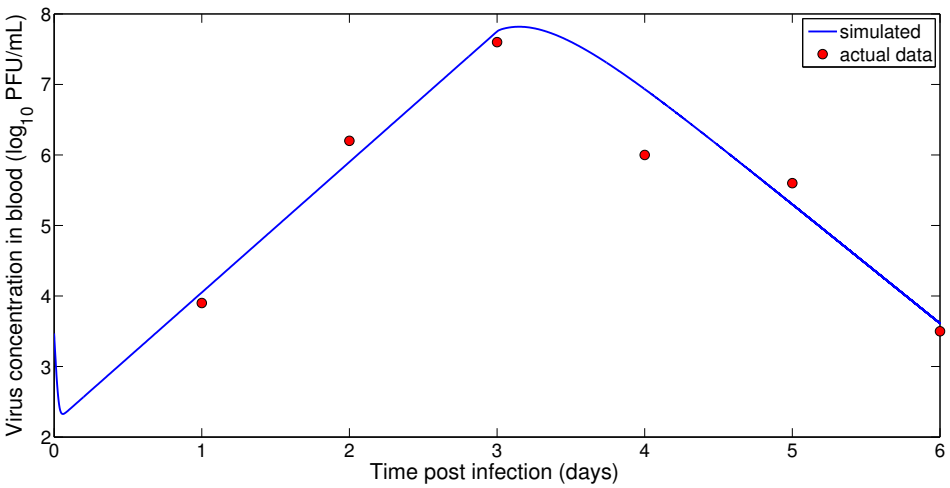

Figure 3.3: A sample plot of virus concentration in blood vs. time post infection (solid line - predicted ODE model output, circles - actual experimental data for a great-horned owl (data from [1]). Y axis - virus concentration in log_{10} PFU/mL of blood, X axis - days post infection.

in immune response if LNs have *privileged metabolism*, i.e. they consume energy which is independent of host mass [6]. However, even if immune system cells are not constrained by the lower mass specific metabolism in larger organisms, it remains to be explained how larger spaces can be searched in invariant time.

3.6 Searching for a needle in a haystack

The NIS is confronted with a very difficult search problem. Extremely rare B cells or T cells specific to a particular antigen (1 antigen-specific T cell in 10^6 T cells)[40] search for initially rare antigen in localized tissue. A constant number of virions is injected into a host by mosquitoes, regardless of host size, for WNV [34] and other pathogens spread by mosquito vectors. Our analysis of the ODE model and the empirical t_{pv} suggest that the NIS in bigger organisms can find this fixed number of

virus particles in approximately the same time as in smaller organisms, i.e. a horse finds those virions in a body (i.e. 'haystack') 10,000 times larger than a sparrow's body, but in the same time.

By way of introduction we define a *completely modular system* as one that is composed of self-contained units that are a fixed size and do not need to communicate, and a *module* as a LN and its DR. To simplify our models, we assume that each LN has a single DR and a DR drains into a single LN. Perfectly parallel search is easily achievable if an immune response is completely modular at the LN level and systemic communication in the immune system does not generate more overhead in larger systems. Completely modular systems have no overhead of communication and hence achieve perfectly parallel search [41] since search is in a space of the same size and is replicated in parallel. However, experimental evidence suggests that the NIS is not modular at the LN level (see Section 3.9) [42, 7, 43].

A conceptually similar concept of modularity has been proposed in *protecton theory* [44]. A *protecton* is a modular unit of protection consisting of 10^7 B cells of different specificities per mL of volume and is iterated proportionally to the size of the organism, i.e. if one samples 1 mL of a tadpole and 1 mL of an elephant, the same set of 10^7 B cells will be found in each, but the elephant will have more copies of the protecton. This modular design reduces the time taken to build up a population of effector cells by clonal expansion. The protecton is a theoretical concept that the density and diversity of lymphocytes is constant across organisms. However, theory does not address how the lymphocytes constituting a protecton migrate through the body or how much communication occurs between lymphocytes or LNs. This further motivates the question of investigating whether there is modularity at the level of LN that would help to parallelize the search process. Sections 3.7 and 3.8 explore the empirical architecture of LN organization, and explain why a purely modular architecture is not optimal.

3.7 Agent based model to explore how LN size affects NIS response time

The general model of immune system dynamics in the LN and its DR are shown in Fig. 3.4 and summarized as follows:

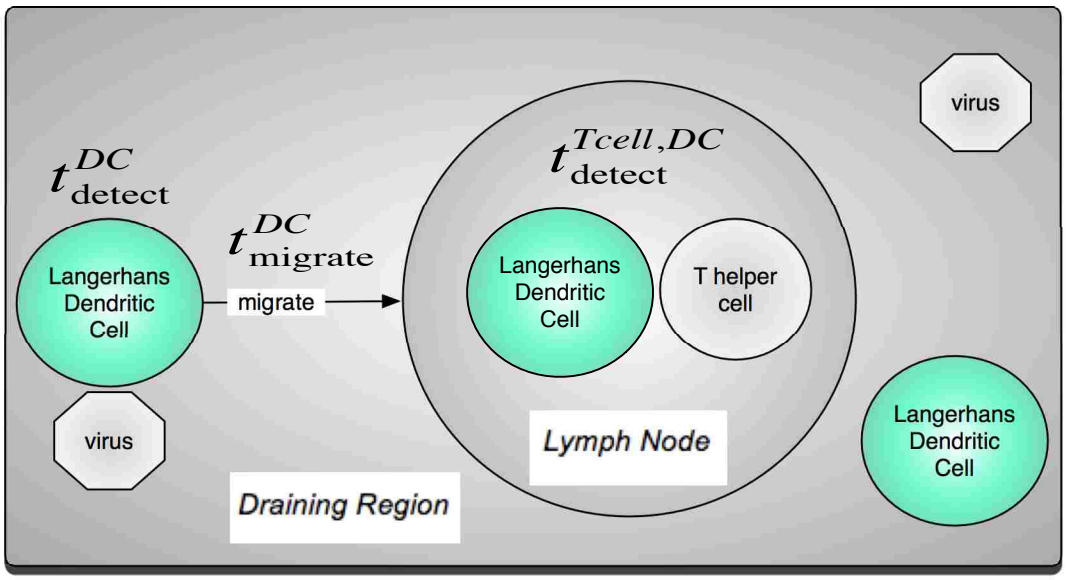

Figure 3.4: Immune system dynamics within a lymph node and its draining region.

1. Stage 1: DCs randomly search for antigen in a local DR. The time taken to detect antigen is denoted by t^{DC}_{detect}.

2. Stage 2: DC migrates to a local LN T cell area along a chemotactic gradient. The time taken to migrate is $t^{DC}_{migrate}$.

3. Stage 3: Antigen-specific T cell in a LN detects antigen on DC and the time taken to detect is $t^{Tcell,DC}_{detect}$. T cells then activate cognate B cells which undergo clonal expansion to produce antibody-secreting plasma cells.

Table 3.3: The parameters used in the agent based model together with a short description of their role and default value (L - literature, F - fit to data)

Description	Value	Source
Side length of cubic compartment (DR)	$1000\mu m$ to $4000\mu m$	L [42]
Side length of cubic compartment (LN)	$250\mu m$ to $1000\mu m$	L [42]
Duration of a time step	60 sec	F
Number of antigen specific B cells in a lymph node of 10^6 B-cells	1	L [40]
Density of DC in DR	$1250/mm^3$	L [45]
Amount of antigen in DR	100	L [34]
Radius of T cell	$10\mu m$	L [40]
Radius of antigen-presenting DC	$30\mu m$	L [40]
Speed of T cell	$0.1664\mu m/sec$	L [40]
Speed of antigen-presenting DC in LN	$0.0416\mu m/sec$	L [40]
Speed of antigen-presenting DC in DR	$0.0832\mu m/sec$	L [46]
Sweep and sense distance of antigen-presenting DC (measured from cell center)	$50\mu m$	L [40]

Total time to detect antigen is given by

$$t_{detect} = t^{DC}_{detect} + t^{DC}_{migrate} + t^{Tcell,DC}_{detect} \tag{3.5}$$

We consider the time spent by the draining infected site LN in recruiting other NIS cells to it as the time spent in communication (t_{comm}) (see Section 3.9).

We use an ABM to investigate how organization of the lymphatic network minimizes the time to detect antigen t_{detect} and t_{comm}, leading to scale-invariant detection and response.

We note that the total volume of organs and fluids in mammals both scale proportional to M [47, 11], so in our models, we assume that LN volume and the total volume of lymph in the entire body are both proportional to M. Thus, the number of LN multiplied by the volume of each LN is proportional to M. Additionally, the volume of a DR is determined by M (which is proportional to body volume, given that tissue density is constant across animals)[47] divided by the number of LN, i.e., for a fixed size M, more LN result in a smaller DR for each LN.

In order to explore how the spatial arrangement of LNs affects time to detect antigen, we use the CyCells [29, 30] ABM to simulate viral replication in a 3D compartment representing the LN and DR. We simulated DCs, T cells, viruses and LNs, and explicitly modeled DC migration from tissue to LN along a chemotactic gradient, and random walk of DC and T cells in LN T cell area. The model parameters are summarized in Table 4.1.

The assumptions that we make are: a) initially, we ignore migration of antigen specific B cells from other LNs. We consider how such systemic responses change the NIS architecture in the next section; b) there is a fixed chemotactic gradient for DCs to migrate into the LN; c) for simplicity, we ignore pathogen replication in the tissue since WNV does not replicate until after it spreads to the LN and other organs; d) DCs and T cells perform random walks in LN T cell area [48]; and e) LNs have *preferential metabolism* [6], i.e. inside a LN, NIS cells have speed and proliferation rates that are invariant with host mass M.

3.8 Results

We first use an ABM to calculate the detection and migration times in Eqn. (5) for mice and then show how each of these times scale with LN and DR dimensions. We then use these scaling relations to derive analytical expressions for detection,

Table 3.4: Simulated values in mice for DC antigen detection, DC migration and DC-T cell interaction

Times	Dimensions (DR, LN)	Value (simulation)
t_{detect}^{DC}	$4000\mu m$, $1000\mu m$	Mean = 26 minutes, SD = 32 minutes, 10 simulations
$t_{migrate}^{DC}$	$4000\mu m$, $1000\mu m$	Mean = 3.7 hours, SD = 1.3 hours, 10 simulations
$t_{detect}^{Tcell,DC}$	$4000\mu m$, $1000\mu m$	Mean = 15.1 hours, SD = 6 hours, 10 simulations

Table 3.5: Scaling relations for time for DC antigen detection, DC migration and DC-T cell interaction (l_{DR} = length of DR compartment, l_{LN} = length of LN compartment).

Times	Dimensions (DR)	Scaling Relation	Statistics
t_{detect}^{DC}	$1000\mu m$, $2000\mu m$, $4000\mu m$	$\propto (l_{DR} - l_{LN})^0$	$p > 0.05$ $^+$
$t_{migrate}^{DC}$	$1000\mu m$, $2000\mu m$, $4000\mu m$	$\propto (l_{DR} - l_{LN})^1$	$r^2 = 0.97, p < 0.001$ $^+$
$t_{detect}^{Tcell,DC}$	$1000\mu m$, $2000\mu m$, $4000\mu m$	$\propto l_{LN}^0$	$p > 0.05$ §

migration and communication times for three hypotheses of LN organization.

Table 3.6: Scaling relations for LN and DR parameters and how $t_{migrate}^{DC}$ depends on DR and LN dimensions (N - number of LNs, V_{lymph} - volume of lymph, V_{LN} - volume of LN). § - taken from empirical data [7]

LN Architecture	N	$V_{lymph} \propto N * V_{LN}$	V_{LN}	$V_{DR} \propto M/N$	$t_{migrate}^{DC} \propto l_{DR} - l_{LN}$	$t_{comm} \propto M/V_{LN}^2$
Model 1	M^1	M^1	M^0	M^0	M^0	M^1
Model 2	M^0	M^1	M^1	M^1	$M^{1/3}$	M^{-2}
Model 3	$M^{1/2§}$	M^1	$M^{1/2}$	$M^{1/2}$	$M^{1/6}$	$M^{-1/2}$

3.8.1 The base case model of a typical lymph node and scaling up

A DR was simulated as a cubic compartment of side $4000\mu m$ with a cubic LN of length $1000\mu m$. The mean time taken by DCs to detect antigen and the time taken by an antigen-specific T cell to recognize antigen on DC are shown in Table 3.4 (due to the prohibitively high execution time of the ABM, we took the average of 10 model realizations). These are in agreement with experimental observations in mice [40]. The total time to detect antigen ($t_{detect} = t^{DC}_{detect} + t^{DC}_{migrate} + t^{Tcell,DC}_{detect}$) is then around 19 hours. This is in agreement with experimental studies in mice [49] and consistent with our observation that peak viral concentration occurs in day 2 to 4 for WNV across organisms, given our hypothesis that the peak occurs due to WNV-specific NIS cells, which must first have come into contact with WNV in the LN.

The DR and LN regions were then scaled up and we observed how DC detection, migration and T cell interaction times scaled with the size of the DR and LN. We simulated 3 cubic DRs: DR of length $1000\mu m$ with LN of length $250\mu m$, DR of length $2000\mu m$ with LN of length $500\mu m$, and DR of length $4000\mu m$ with a LN of length $1000\mu m$. The observed scaling relations are in Table 3.5 and are consistent with DC migration time scaling linearly with the mean distance from DR to LN. The time for DC to detect antigen specific T cell in LN was found to be uncorrelated with the size of the LN.

We now explore 3 competing hypotheses of lymphatic system organization (Fig. 3.5).

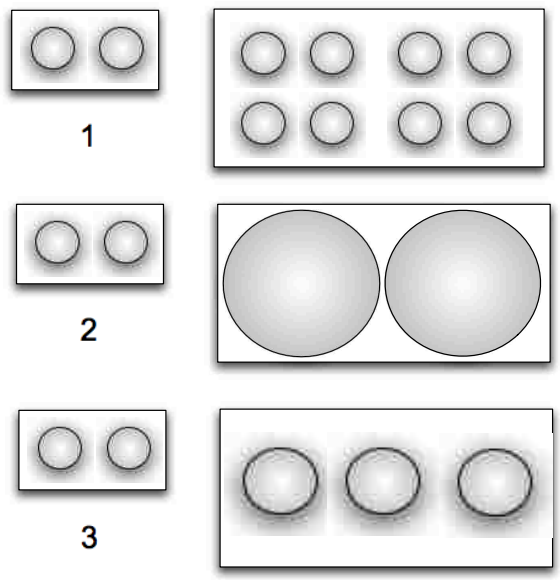

Figure 3.5: The 3 different hypotheses of scaling of lymph node size and numbers. (1) Completely Modular Detection Network: base organism with 2 LNs and another organism 4 times as big with 4 times the number of lymph nodes each of the same size as the base organism. (2) Non-Modular Detection Network: organism 4 times bigger has the same number of LNs but each is 4 times bigger. (3) Hybrid Sub-Modular Detection Network: organism 4 times bigger has more LNs each of which are also bigger.

3.8.2 Model 1: Completely modular detection network

In our first model, we assume that the lymphatic network forms a *completely modular network* containing LN of constant size and number of LN proportional to organism size M. Using the scaling relationship for $t^{DC}_{migrate}$ from Table 3.5 and noting that in this model the LN and DR dimensions do not change with organism size gives us $t^{DC}_{migrate} \propto M^0$. Since the ABM predicts that detection times in LN do not depend on LN dimensions (Table 3.5) we have $t_{detect} \propto M^0$ and hence the completely modular architecture gives us perfect scale-invariant detection. The predicted relations are summarized in Table 3.6.

3.8.3 Model 2: Non-modular detection network

The second model is the other extreme, that LNs are arranged in a detection network with a constant number of LN (all animals have the same number of LNs, however the size of LNs is larger in larger animals). In this model, the DR volume increases proportional to organism mass, and the average distance that a DC has to travel from the DR to the LN increases with organism mass as $M^{1/3}$ (Table 3.6). Hence $t^{DC}_{migrate} \propto M^{1/3}$. Since DC migration times are approximately 4 hours in mice, this model predicts that DC migration times in horses (which are 25,000 larger than mice) will be 30 times more than that in mice. This would necessitate migration times that are 5 days in horses and greater than the total observed time for antibody response. Hence the hypothesis of complete lack of modularity in the NIS is inconsistent with observations.

3.8.4 Model 3: Hybrid sub-modular architecture

This architecture lies midway between Model 1 and Model 2. In this model LNs increase in both size and in numbers as animal size increases, and so does the size of the DR. Table 3.6 gives the predicted relation for $t^{DC}_{migrate} \propto M^{1/6}$. This will lead to migration times that are only 5 times longer in horses (around 20 hours) than in mice. It is not implausible that detection should take so long in a horse, and these slight increases in detection time might be compensated for by slower rates of exponential growth by the pathogen, as predicted by our ODE model (Section 3.5). Hence the sub-modular architecture produces detection times which are consistent with our empirical observations (scale-invariant detection), since the difference between 4 hours and 20 hours cannot be resolved on the basis of measurements of viral load taken every 24 hours.

3.9 Sub-modular architecture balances tradeoff between local and global communication

The limited published empirical data that we could find suggest that the mammalian NIS has a hybrid sub-modular architecture (Model 3). There is a trend of increasing LN size and number as animal size increases, for example, 20g mice have 24 LN averaging 0.004g each, and humans are 3000 times bigger and have 20 times more LN, each 200 times bigger [42, 7]. Data from elephants (with LN approaching the size of an entire mouse) and horses (with 8000 LN) also support the hypothesis that LN size and number both increase with body size (Model 3) [43, 7]; however, data for more species are required to statistically reject any of our 3 models.

We hypothesize that the NIS is submodular (consistent with Model 3) because it is selected not just to minimize time to detect pathogens (achieved by Model 1), but also to minimize the time to produce a sufficient concentration of antibody in the blood (Ab_{crit}). A horse 25,000 times larger than a mouse must generate 25,000 more absolute quantities of antibody (Ab) in order to achieve the same concentration of antibody in the blood (where blood volume is $\propto M$)[47]. A fixed antibody concentration is required to fight infections like WNV that spread systemically through the blood. We can now consider that the NIS has evolved to minimize two quantities: the time to detect antigen (t_{detect}), and the time ($t_{produce}$) to produce Ab, where Ab is proportional to M (Ab is the absolute quantity of antibody required to neutralize the pathogen in blood).

In all pathogens which evoke the adaptive immune system, the rate limiting step is the recognition of antigen on DCs by antigen-specific T helper cells within the LN T cell area [36]. The time taken in this recognition step impacts other downstream processes like activation of B cells since T helper cells activated by DCs must migrate to the B cell area to activate B cells. If organisms of all body sizes activated the

same number of initial B cells prior to clonal expansion, the time for a fixed number of B cells to produce Ab would be $\propto log_2 M$ (since B cells reproduce exponentially through clonal expansion). For example, since it takes 4 days of exponential growth of activated B cells to produce sufficient anti-WNV neutralizing antibody in mice [39], then the corresponding time for a horse would be more than 2 months, should the same number of initial B cells be activated prior to clonal expansion. This conflicts with empirical data on horses [2]. We assume that the NIS of larger organisms has to activate a larger number of initial B cells (B_{crit}) $\propto M$, in order to build up the critical density of antibodies in a fixed period of time. We now ask how the NIS can activate B_{crit} in our three models.

In Model 1, LNs are a fixed size, and therefore contain a fixed number of B cells, and the smallest LNs (e.g. in mice) contain on the order of a single B cell that recognizes any particular pathogen. Thus, activating B_{crit} to fight an infection like WNV that is initially localized in a single DR, requires recruiting B cells from distant LN. We consider this activation of B cells from remote LN as communication overhead. In general, the number of LNs that a single infected site LN has to communicate with (N_{comm}) in order to recruit more B cells is proportional to the amount of antibody required to neutralize the pathogen divided by the number of B cells resident in a LN (Num_{Bcell}): $N_{comm} \propto Ab/Num_{Bcell}$. Noting that $Ab \propto M$ and $Num_{Bcell} \propto V_{LN}$ we have $N_{comm} \propto M/V_{LN}$

The rate at which new B cells from other LN enter into infected site LN through the blood or lymphatic vessels ($rate_{comm}$) is proportional to the volume of the LN, $rate_{comm} \propto V_{LN}$ (assuming that a larger LN will have proportionally more high endothelial venules and hence can recruit at a higher rate). The time spent in communicating with other LNs and recruiting and activating other B cells (t_{comm}) is then given by

$$t_{comm} = N_{comm}/rate_{comm} \propto M/V_{LN}^2 \tag{3.6}$$

Hence in Model 1, there are increasing costs to communicating with other LN as the organism gets bigger ($t_{comm} \propto M$); it carries out efficient search but is not optimized for antibody production.

Model 2 (non-modular detection network) compensates for the limitation of physically transporting NIS cells over larger distances by making LNs bigger in larger organisms ($V_{LN} \propto M$). This increases the rate of influx of B cells ($rate_{comm} \propto V_{LN} \propto M$) and also situates more NIS cells inside the infected site LN. Since all the necessary NIS cells that need to be activated are within the LN, this architecture has no communication cost. However, as shown above (Section 3.8.3), Model 2 leads to DC migration times that are prohibitively long for large animals ($t_{migrate}^{DC} \propto M^{1/3}$).

The architecture that strikes a balance between the two opposing goals of antigen detection (local communication) and antibody production (global communication) is Model 3 (hybrid sub-modular architecture). It minimizes $T = t_{detect} + t_{produce}$, where t_{detect} = time taken to detect antigen, and $t_{produce}$ = time taken to produce antibody = t_{comm} (since the time taken to produce antibodies is equal to the time taken to recruit B cells or communicate with other LNs; after recruitment starts and cognate T cells recognize antigen on DCs, T cells can migrate to the B cell area and activate B cells in parallel to the recruitment process described earlier).

We can solve for the total time ($T = t_{detect} + t_{produce}$) to detect antigen and produce B cells using Eq. (7) and the scaling relationship for $t_{migrate}^{DC}$ from Table 3.5 giving:

$$T = t_{detect}^{DC} + a(l_{DR} - l_{LN}) + t_{detect}^{Tcell,DC} + bM/V_{LN}^2 \tag{3.7}$$

where a and b are constants, l_{DR} = length of DR, l_{LN} = length of LN, V_{LN} = volume

of LN, M = organism mass, and N = number of LNs. This becomes

$$T = t_{detect}^{DC} + cV_{LN}^{1/3} + t_{detect}^{Tcell,DC} + bM/V_{LN}^{2} \tag{3.8}$$

where c is a constant, and l_{DR} and l_{LN} scale as $V_{DR}^{1/3}$ and $V_{LN}^{1/3}$ respectively since V_{LN} and V_{DR} scale isometrically, as M/N.

Differentiating with respect to V_{LN} and setting the derivative to zero to find the minimum T, gives

$$V_{LN} \propto M^{3/7} \tag{3.9}$$

Since the amount of lymph is proportional to host body mass ($N * V_{LN} \propto M$), then

$$N \propto M^{4/7} \tag{3.10}$$

These predictions are consistent with the few empirical data we were able to obtain. Similar arguments would also apply to other pathogens that spread systemically throughout the body and need to activate a number of B-cells or cytotoxic T cells proportional to M. We note that $N \propto M^{1/2}$ was predicted by Perelson and Wiegel [50], but that analysis did not explicitly consider an optimization to simultaneously minimize detection time and time to produce the critical number of Ab.

In summary, due to the requirement of activating increasing number of NIS cells for antibody production in larger organisms, there are increasing costs to global communication as organisms grow bigger. The semi-modular architecture (Model 3) balances the opposing goals of detecting antigen using local communication and producing antibody using global communication between LNs. This leads to optimal antigen detection and antibody production time, and nearly scale-invariant detection and response.

3.10 Relevance to artificial immune systems

The natural immune system utilizes an architecture that functions within constraints imposed by physical space. Physical space is also an important constraint on artificial immune systems, especially in applications used to connect inexpensive low-powered sensors using short-range wireless communication [51]. Such spatial networks are being increasingly used in environmental monitoring, disaster relief and military operations [51]. These networks might operate under constraints of resource and physical space, similar to an NIS. Although there are systematic differences between an NIS and an AIS [52], the design of the AIS can be informed by architectural strategies employed by their biological counterpart.

3.10.1 Original system

As a concrete example of an application where space is a constraint and scaling of performance with system size is an important design criterion, we consider an AIS approach to control multiple robots tasked with obstacle avoidance [53]. The robots communicate with software agent(s) in a server upon encountering an obstacle. The agents transmit rule-sets of actions to robots to help overcome their obstacles, and agents also share information globally amongst themselves by migrating to other computer servers. Some analogies between this AIS and an NIS are: the obstacle problem presented by a robot is analogous to an antigen, the rule-set of actions transmitted by an agent correspond to antibodies, the robots are akin to DCs, software agents correspond to B cells, the computer servers themselves are analogous to LNs, and the physical area 'serviced' by a single computer server corresponds to a DR. The system is diagrammed in Fig. 3.6 (modified from [53]).

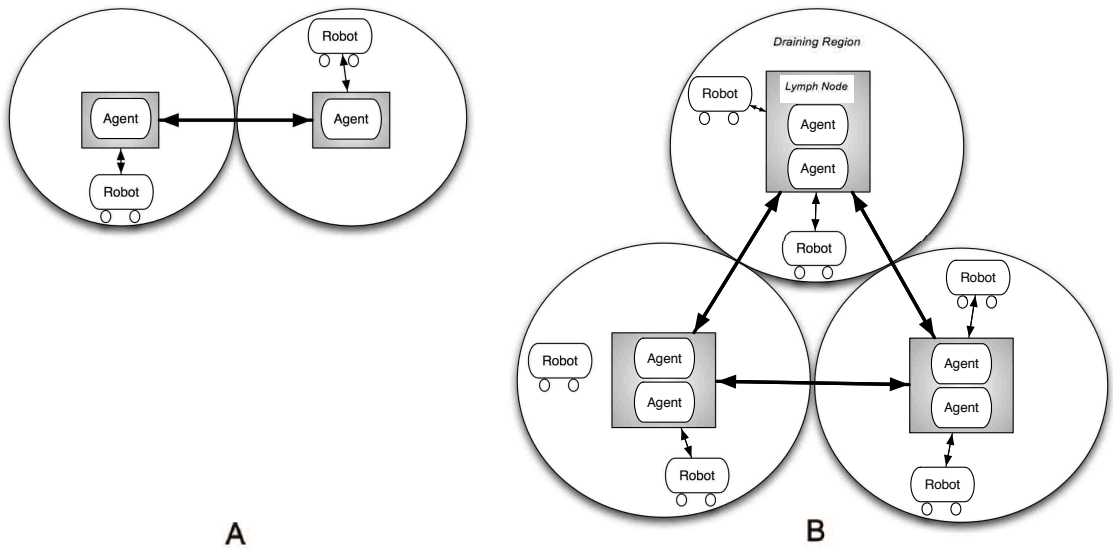

Figure 3.6: (A) Left Panel: a scaled down version of the multi-robot AIS system. The shaded regions are artificial LNs (computer servers) and the unshaded regions are the artificial DR. Light arrows denote communication between robots and servers (local communication) and bold arrows denote communication between servers (global communication). (B) Right Panel: a scaled up multi-robot AIS system with sub-modular architecture. Note that the number of artificial LNs and their size (the number of robots they service and the number of software agents they have in memory) both increase with the size of the system.

3.10.2 Modifying the original system using a sub-modular architecture

We are interested in an architecture that minimizes the time taken by a robot to transmit information about an obstacle (local detection), the time taken by a computer server to transmit back an initial rule-set of actions (local response) and the time taken by a computer server to communicate good rule-sets to other agents (global response). There are two potential communication bottlenecks: communication between robots and computer servers, and communication between computer servers.

Overcoming the bottleneck in (local) communication between robot and server requires many small DRs. A bottleneck in (global) server communication requires a few large servers. If both local and global communication are constrained, the architecture which balances these opposing requirements is sub-modular, i.e. the number of servers increases sublinearly with system size and the capacity of each server (bandwidth, memory and number of robots serviced by each server) increases sublinearly with system size (shown in Fig. 3.6). The four ways in which communication can be bottlenecked are outlined below:

1. High Capacity Robot Bandwidth, High Capacity Server Bandwidth: Assuming that robots have high bandwidth to communicate with computer servers and software agents can communicate with each other over a channel with high bandwidth, we see that trivially any of the architectures would suffice.

2. Limited Robot Bandwidth, High Capacity Server Bandwidth: Assuming communication between robots and computer servers is a bottleneck mandates a small fixed size DR, i.e. a computer server servicing a small number of robots to reduce contention and transmission time. Since communication between servers is not constrained, we can have the number of servers scaling linearly with system size, giving Model 1 (completely modular network) as the optimal architecture.

3. High Capacity Robot Bandwidth, Limited Server Bandwidth: Assuming communication between computer servers is a bottleneck stipulates a fixed number of computer servers to reduce communication overhead. Since communication between robots and servers is not constrained, we can have the DR size (number of robots serviced by a single server) and LN size (number of agents in a single server) scaling with system size. Hence the optimal architecture is Model 2 (non-modular detection network).

4. Limited Robot Bandwidth, Limited Server Bandwidth: A bottleneck in robot and server communication demands a small DR and lots of servers, whereas a bottleneck in server communication requires fewer large servers. The architecture that balances these opposing requirements is Model 3 (hybrid sub-modular architecture), i.e. the number of servers and their size (number of robots serviced by each server) increases with system size (3.6).

The local communication time within an artificial DR is a function of the number of robots (d) serviced by a single artificial LN

$$t_{local} = f(d) \tag{3.11}$$

The function f will depend on constraints on communication between robots and servers, influenced, for example, by how robot requests are queued on the server and the distance over which low power robots can send and receive messages. The global communication time between artificial LNs is also a function of the number of LNs in the system (n/d) where n is the total number of robots in the entire system

$$t_{global} = g(n/d) \tag{3.12}$$

The function g depends on communication constraints between servers. For low latency and high bandwidth connections among servers, t_{global} may not scale appreciably. However, low power servers distributed in remote environments, may preclude broadcast communication such that t_{global} increases with n/d. An increase in the size of an artificial LN (and hence the number of robots serviced, d) would reduce t_{global} at the cost of t_{local}. The size and number of artificial LNs to balance local and global communication depends on the precise functions f and g mediating local and global communication.

Although we have provided only one example, this research is widely applicable to other distributed systems AIS applications. In recent work, we have extended our work to modify peer-to-peer systems with a sub-modular architecture [54].

In summary, understanding the tradeoff between fast search for pathogens and fast production of antibodies is important for AIS that mimic the NIS. If the goal of an AIS is only search or detection in physical space with a local response, then a completely modular design (Model 1) will be optimal. If an AIS searches in physical space but requires a global response after detection, a sub-modular architecture (Model 3) optimizes the tradeoff between local search and global response and will lead to faster search and response times ($T = t_{local} + t_{global}$). Our analysis sheds light on the relationship between physical space and architecture in resource-constrained distributed systems.

3.11 Conclusions

Host body size constrains pathogen replication rates due to the physical characteristics of transportation networks that supply infected and normal cells with energy. Host body size also constrains NIS detection and response times by increasing the physical size of search spaces. The NIS is comprised of rare antigen-specific immune system cells that it must utilize to search for initially small numbers of pathogens localized in a large physical space. The NIS solves this classic search for a 'needle in a haystack' in time that is almost invariant of the size of the organism. The decentralized nature of the lymphatic network also helps in efficient pathogen detection by acting as a small volume of tissue where DCs can efficiently present antigen to T cells. The NIS must also respond to the antigen by producing antibodies (in the case of WNV) proportional to the mass of the organism. From empirical data, that time also appears independent of body size.

We use an ODE model to show that NIS response rates are independent of host body size and pathogen replication rates decrease with body size. We examine three different hypothesized NIS architectures using an agent based model, to explain the scale-invariant detection and response times of the NIS. The sub-modular detection network strikes a balance between the two opposing goals of antigen detection (local communication) and antibody production (global communication), and is consistent with observed numbers and sizes of LN. This submodular architecture of the lymphatic network must simultaneously provide systemic protection to the entire body while protecting each local volume of tissue equally well. Thus, the lymphatic architecture lies between the extremes of the fully centralized cardiovascular network (in which blood is oxygenated in a single location) and the fully decentralized concept of the protecton (in which a fixed number and diversity of lymphocytes protects every volume of tissue).

We demonstrated that a submodular architecture effectively balances the tradeoff between local search for a solution and global distribution of the solution in distributed robot control. In addition to incorporating NIS inspired distributed search algorithms into AIS, we suggest that AIS can replicate the submodular architecture used by the NIS to balance the tradeoff between local and global communication.

3.12 Acknowledgements

We acknowledge fruitful discussions with Dr. Alan Perelson, Dr. Stephanie Forrest, Dr. Jedidiah Crandall and Kimberly Kanigel, helpful reviews from the ICARIS 2009 conference and four anonymous referees for their insightful comments. We are also grateful to Dr. Nicholas Komar for sharing his experimental data with us. MEM and SB were supported by a grant from the National Institute of Health (NIH RR018754) to the University of New Mexico Center for Evolutionary and Theoretical

Immunology. SB would also like to acknowledge travel grants from RPT, SCAP and PIBBS at the University of New Mexico.

Chapter 4

The Value of Inflammatory Signals in Adaptive Immune Responses

4.1 Abstract

Cells of the immune system search among billions of healthy cells to find and neutralize a small number of infected cells before pathogens replicate to sufficient numbers to cause disease or death. The immune system uses information signals to accomplish this search quickly. Ordinary differential equations and spatially explicit agent-based models are used to quantify how capillary inflammation decreases the time it takes for cytotoxic T lymphocytes to find and kill infected cells. We find that the inflammation signal localized in a small region of infected tissue dramatically reduces search times, suggesting that these signals play an important role in the immune response, especially in larger animals. This chapter was co-authored by Drew Levin, Melanie E. Moses, Frederick Koster and Stephanie Forrest (Department of Computer Science, University of New Mexico). It was published in the 10th International Conference on Artificial Immune Systems (ICARIS), *Lecture Notes in Computer Science*, Volume

6825, 2011, pp. 1-14.

4.2 Introduction

Rapid search is crucial for an effective immune response: Immune system cells must find, identify and neutralize pathogens before those pathogens replicate in sufficient numbers to cause disease or death. The adaptive immune system has a small number of pathogen-specific cells that must search for and neutralize a small number of initially localized pathogens in a very large tissue space. We investigate how inflammatory signals accelerate this search.

The adaptive immune response must conduct two "searches" to neutralize pathogens. First, recirculating antigen-specific T and B cell precursors must interact with antigen-loaded dendritic cells, and the architecture of the lymph node facilitates this interaction [55, 54, 26]. The second search is T cells activated in the lymph node efficiently finding and neutralizing infected cells in tissue with the help of inflammatory signals. In this paper we analyze these two searches in response to influenza infection in the lung.

CTLs are activated within the infected site LN and are released into the bloodstream where they travel through a branching network of arteries until they reach a capillary in the lung. Capillaries in infected regions of the lung are permeated by an inflammatory signal which causes CTLs to exit the capillary and enter the lung tissue, where a chemokine gradient guides the CTL to infected cells. When CTLs recognize the antigen displayed on the surface of infected cells, they neutralize those cells. The information represented by the inflammatory signals is local, and occurs in an initially small region of the lung surface, possibly as small as a few mm^2 in a 100 m^2 surface area in a human lung [56]. We ask how much the local inflammatory signal reduces the time for CTLs to find the site of infection and eradicate the in-

fluenza pathogen. Without an inflammation signal indicating which capillaries are near infected tissue, CTLs would have to exit capillaries in random locations and begin a slow random walk (at speeds measured in microns per minute) through the large area of lung tissue to search for the site of infection. With the inflammatory signal, CTLs can exit the relatively fast flow of the circulatory network only when they are in close proximity to infected cells.

In this paper we describe two sets of models. The first (null) model predicts how long it would take for CTLs to find infected cells by searching via a random walk through the entire lung tissue. The second set of models are simplified representations of how inflammatory signals guide CTL search in real immune systems. This second set of models is parametrized from experimental data. By comparing predictions of the null model to the more realistic model with inflammation, we estimate how much the inflammatory signal reduces the time for CTLs to find and eradicate influenza.

We use ordinary differential equation (ODE) and agent-based models (ABM) to quantify the value of the inflammatory signal, measured as the decrease in the time it takes for CTLs to both find and eradicate virus from the lung. The ABM incorporates the spatial aspect of virus spread and CTL mediated killing of infected cells, and the ODE model can scale up to realistic cell population sizes. In both cases, we first model an immune response without inflammatory signals where CTLs exit to tissue at the first capillary they encounter and search by random walks until they find a chemokine gradient that guides them to the infected cells. Second, we model an immune response with inflammatory signals where CTLs exit to tissue only when the capillary has an inflammatory signal. If there is no signal, CTLs recirculate through the cardiovascular network until they find an inflamed capillary. We suggest that localized signals like the inflammatory signal are enormously important to immune function. Here we take a first step toward quantifying the value of that signal in terms of time required to get T cells to sites of infection and to control influenza

infection. This has important consequences for understanding the role of information signals in immune systems more generally, and also the role that local information signals can play in other complex biological systems [57, 58] and in artificial immune systems where decentralized search requires effective use of local signals to solve computational problems [54, 26].

The remainder of the paper reviews relevant features of the immune system (Section 4.3), outlines our hypotheses (Section 4.4), and describes the models (Sections 4.5 and 4.6). Section 4.5 presents the ODE model and compares its predictions to empirical data. Section 4.6 uses the ABM to verify some of the ODE predictions and produce more realistic spatially explicit simulations, including pathogen spread during the CTL search. We conclude by quantifying how much inflammatory signals improve immune response in these models.

4.3 A Review of the Relevant Immunology

This study characterizes how a key type of adaptive immune cells (cytotoxic T lymphocytes, also called $CD8^+$ T cells or CTLs) [59] search for and neutralize a common respiratory tract pathogen (influenza) in the principal target organ, the lung (Fig. 4.1). Among the many immune cells and molecules involved in providing defense against influenza [60], there is a complex set of interactions to guide CTLs to the site of infection and to produce chemokines and other information signals to help contain the infection. We simplify the array of chemokines with a single signal that causes inflammation and attracts CTLs to site of infection.

Infection begins when influenza virus is inhaled into the lung. It enters epithelial cells lining the airways and the air sacs (alveoli) of the lung. Epithelial cells initiate the first line of innate immune defense through the activation of interferon and the secretion of chemokines to attract inflammatory cells such as macrophages [61].

Inflammation increases local blood flow to the infected region and amplifies the chemokine signal. To initiate the adaptive immune response, resident lung dendritic cells capture virus and carry it to the draining lymph nodes (LN). LNs provide a dense tissue in which T and B lymphocytes and antigen-loaded dendritic cells encounter each other efficiently. Antigen-specific CTLs are activated within the LN, undergo cell division, and leave the LN to enter the blood circulation. We focus on the response of cytotoxic T lymphocytes (CTLs) because recovery from influenza pneumonia in wildtype mice has been shown to require neutralization of infected cells by CTLs [62].

The cardiovascular network in the lung follows the fractal branching of the airways.The branching arterioles end in a capillary network which nourishes the airsacs (alveoli) of the lung. The capillary density in mouse lung is approximately $5000/cm^2$ (estimated from [56]). The surface area of a mouse lung is approximately $100cm^2$ giving 500,000 capillaries in the mouse lung. Capillary density decreases as $M^{-1/4}$ where M is organism body mass [11, 56] and since humans are 10,000 times larger than mice, the capillary density in a human lung is $500/cm^2$. The surface area of a human lung is approximately $100m^2$ and hence the number of capillaries in a human lung is approximately $5 \cdot 10^8$.

The CTL flow through the arterial network without any signal to guide them to the tiny fraction of capillaries near the initial infection. If an activated CTL reaches an inflamed capillary, it exits the capillary into lung interstitial tissue. The tissue surrounding inflamed capillaries also contains a chemokine gradient which the CTL follows to locate infected epithelial cells and reduce viral replication. The chemotactic signals are composed of cytokines and chemokines which provide a region of attraction larger than that provided by antigen and infected cells. If an activated CTL reaches an uninflamed capillary, it may wander short distances through the capillary network. If it still does not encounter an inflammatory signal, it recirculates

through the blood and eventually returns to another capillary in the lung. The recirculation time for mice is 6 seconds and 60 seconds for humans [47].

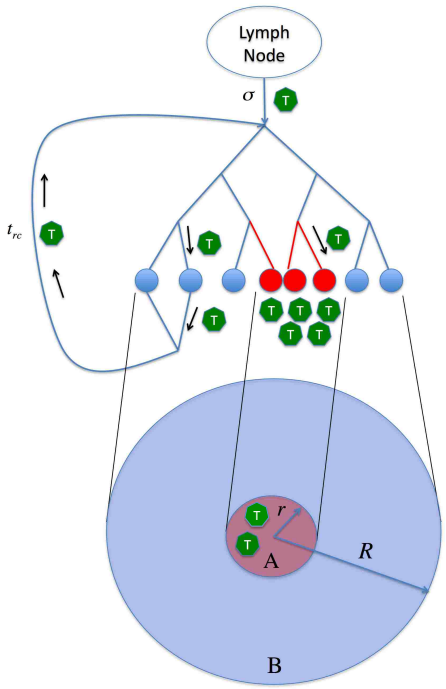

Figure 4.1: A region (A of radius r) of infected tissue, chemokines and inflammatory signals, surrounded by region B which does not have any infected cells, inflammation or chemokines. CTLs (green hexagons) leave the LN at rate σ and travel through the branching arteries to capillaries. If capillaries are inflamed (in region A) CTLs exit capillaries and search for infected cells (small red circles) in lung tissue. If the capillaries are not inflamed (in region B) the CTLs recirculate.

4.4 Goals and Hypotheses

Inflammatory signals and chemotactic gradients are examples of signals that serve to guide search processes in the adaptive immune system. We hypothesize that these and other signals enable the activated immune cells to find and neutralize pathogens

more quickly than in the absence of such signals. More specifically, we aim to quantify the benefit provided by the inflammation in the capillaries, which allows circulating CTLs to know that they have reached a site of infection.

We examine a hypothetical immune response without inflammatory signals (CTLs searching for infected tissue by randomly walking through lung tissue) and a more realistic immune response with inflammatory signals (CTLs recirculate through the arterial network until the presence of inflammation signals them to exit near infected tissue). We study how long it takes for the first CTL to find the infected region, how quickly CTLs accumulate in infected tissue, and how many epithelial cells become infected in a specified time period. We quantify the value of the information signal as the ratio of these values with inflammatory signal to those values without the signal. We use ODE and ABM to estimate the value of the inflammation signal. The ODE can model large numbers of cells, so we use ODEs to compare the value of the inflammatory signal in mice and humans. We then use an agent based model to investigate the dynamics of infection growth and spatial interactions between cells in the mouse.

4.5 Ordinary Differential Equation Model

In this section we analyze how quickly CTLs arrive at the site of infection with and without an inflamation signal using an ODE model. We represent the region of infection as a circular area (region A) of radius r of tissue expressing a general chemotactic signal. This region is surrounded by a region of uninfected tissue (a concentric circle of radius R (region B)) without inflammation or chemokines.

Any activated CTLs that flow to capillaries in region A will have an inflammatory signal that causes the CTL to exit the capillary and a chemokine gradient that will direct those CTLs to infected cells. In contrast, CTLs that arrive in the lung via

capillaries in region B will have no inflammatory signal and no chemokines to guide them to the infected cells in region A. We assume that CTLs that exit into tissue do not go back into circulation.

There are several simplifying assumptions in the ODE model. It ignores viral replication and assumes that the infected region A is a fixed size. It also ignores the movement of CTLs inside capillaries, and instead assumes that CTLs either immediately sense inflammation and exit into tissue or immediately recirculate. The model also ignores CTL death in the lung.

The dynamics of the system are represented by coupled ODEs. We parameterize the ODEs to consider two cases. In the first case, CTLs search for virus using only the random walk (null model). In the second case, CTLs in region A receive an inflammation signal that allows them to exit and follow the chemotactic gradient, while CTLs in region B continue to recirculate through the lymph system until they find an inflamed capillary in region A as in Fig. 4.1.

4.5.1 ODE Model 1: CTL Search Without an Inflammation Signal

In this scenario there is no signal to direct CTLs to an infected region, therefore CTLs always exit into tissue as soon as they reach a capillary. The capillaries are assumed to be uniformly distributed throughout the lung, and a single activated lymph node is assumed to produce activated CTLS at a fixed rate of σ CTLs per hour. The infection is in a region of constant radius r, and the lung surface is a circle of radius R. The time taken for CTLs to circulate through the lymph system is denoted by t_{rc}. The combined system is represented by the following differential equations:

$$\frac{dN_c}{dt} = \sigma - \frac{N_c}{t_{rc}} \tag{4.1}$$

$$\frac{dN_w}{dt} = \frac{(R^2 - r^2) \cdot N_c}{R^2 \cdot t_{rc}} - \frac{D \cdot N_w}{\pi((2/3(R-r)+r)^2 - r^2)} \tag{4.2}$$

$$\frac{dN_f}{dt} = \frac{r^2 \cdot N_c}{R^2 \cdot t_{rc}} + \frac{D \cdot N_w}{\pi((2/3(R-r)+r)^2 - r^2)} \tag{4.3}$$

Equation (4.1) describes the change in the number of recirculating activated CTLs in the cardiovascular system (N_c) due to the rate of production of new CTLs in the LN (σ) and time it takes CTLs to travel to the capilaries (t_{rc}). Since the relevant time step in this setting is the minimum time taken for CTLs to complete one circuit through the arterial and venous circulation system (the recirculation time t_{rc}) and is different from the simulation time step (dt), all rate constants are divided by t_{rc}.

Equation (4.2) describes the change in the number of CTLs (N_w) that are doing a random walk in tissue and searching for infected cells. The change in N_w is due to the rate at which CTLs exit into region B from circulation (a fraction of $\frac{N_c}{t_{rc}}$) and the rate at which these searching CTLs find region A. The fraction of circulating CTLs that enter capillaries in region B is given by the relative area of region B ($\frac{R^2-r^2}{R^2}$). The rate at which CTLs find region A is calculated as follows: an average CTL in region B will be at a distance 2/3 from the periphery of region A (obtained by integrating over all CTLs at each distance in region B). The mean area that this CTL will cover before reaching region A is given by the quantity $\pi((2/3(R-r)+r)^2 - r^2)$, and the mean time in which this area is covered is this quantity divided by the diffusion constant for random walk (D), again adjusted for the recirculation time. The reciprocal of this time gives the rate at which a single CTL enters region A. To complete the analysis

we multiply this quantity by the number of searching CTLs. Finally, Equation (4.3) describes the change in the number of CTLs (N_f) that have found infected cells (in region A). This is composed of the searching CTLs from Equation (4.2) that find the infected region and the fraction of the recirculating CTLs from Equation (4.1) that enter capillaries in region A (represented by the area of region A relative to the total lung area). We use the model to study the arrival of CTLs at the site of infection, first in the mouse lung and then in the human lung.

In order to numerically integrate Equations (4.1)-(4.3) we first estimate the diffusion rate of CTLs. Since we are not aware of any published values for diffusion rates of activated CTLs within tissue, we used measured mean square displacements of T cells within the LN [63]. Following Beauchemin et al. [63], the equation relating mean square displacement of a random walking particle in two dimensions at time t is given by $\mid m \mid = \sqrt{4Dt}\frac{\Gamma(\frac{3}{2})}{\Gamma(\frac{1}{2})}$ where $\mid m \mid$ is the mean square displacement, D is the diffusion constant and Γ is the gamma function. We estimated D as $56(\mu m)^2/h$ in the LN [63], and we use this value to characterize the random walk in lung tissue.

We estimate the parameter σ from experimental data (detailed in the next section) as 864 activated CTLs per hour, and the time to recirculate (t_{rc}) is 6 seconds [64]. The area of infection has a radius (r) of 1 mm (personal observation for seasonal strains in mice) and the total lung surface is represented by a circle with a radius of 10 cm (R) [56].

The model shows that there is a steady state of approximately 2 circulating activated CTL. So few CTLs are in circulation because they exit the LN approximately 1 every 4 seconds and spend only 6 seconds in blood before immediately exiting the blood to search in the lung. We numerically simulated the ODE system and found that the time for the first CTL to reach the site of infection (region A) is approximately 12 hours post activation in the LN (Fig. 4.2, Panel A). Approximately 10 CTLs find the infected region at day 5 post activation.

Next we use ODE Model 1 to predict how quickly CTLs arrive at the infected site in a human. Human body mass is approximately 10,000 times larger than a mouse. Human lungs are a corresponding 10,000 times greater area, so R becomes 10 meters [56]. We assume that the initial area of infection r remains the same 1mm^2. CTL recirculation time (t_{rc}) increases to 60 seconds [64].

In order to calculate the rate of CTL production from LN (σ) we scale the (σ) estimated for mice by a factor of $M^{3/7}$ following [26]. This scaling assumes that LNs in larger animals are larger and have more high endothelial venules to release activated CTLs at a faster rate. From this we estimate σ as approximately 45000 CTLs per hour. Numerically simulating the ODE system, we predict the time for a CTL to find an infected cell in a human lung as approximately 90 days, which is much longer than the actual time taken to resolve influenza infections (approximately 10 days) [62].

4.5.2 ODE Model 2: CTL search with an Inflammatory Signal

Here we model an immune response with inflammatory signals. CTLs exit capillaries and enter lung tissue only when there is an inflammatory signal in the capillary. All other parameters are identical to ODE Model 1. The system is represented by the following differential equations:

$$\frac{dN_c}{dt} = \sigma - \frac{r^2 \cdot N_c}{R^2 \cdot t_{rc}} \tag{4.4}$$

$$\frac{dN_f}{dt} = \frac{r^2 \cdot N_c}{R^2 \cdot t_{rc}} \tag{4.5}$$

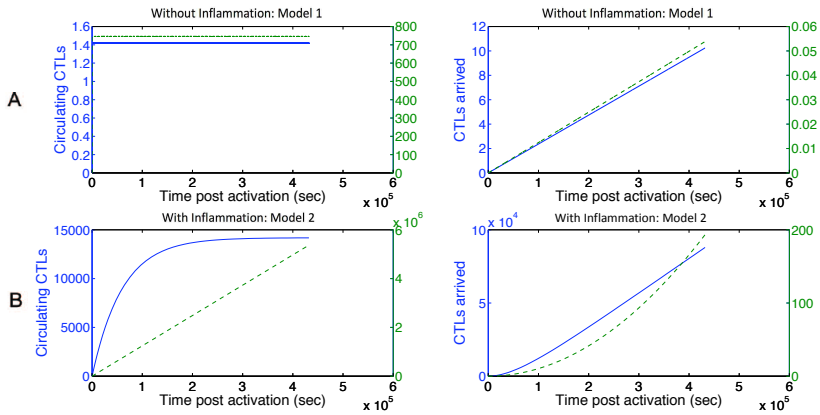

Figure 4.2: Row A: The number of circulating CTLs (N_c) and CTLs that have arrived at the site of infection(N_f) vs. time post activation of the first CTL in LN for CTLs searching without an inflammatory signal (ODE Model 1) for mice (blue, left axis) and humans (green dotted, right axis). The number of recirculating CTLs reaches a steady state because once they enter the lung they never recirculate. Row B: N_c and N_f vs. time post activation for CTLs circulating in the presence of inflammatory signals (ODE Model 2 fit to experimental data) for mice (blue, left axis) and humans (green dotted, right axis). Note the difference in y-axis scale between the two rows.

Equation (4.4) describes the change in the number of circulating activated CTLs circulating in the cardiovascular system (N_c). (N_c) changes due to the addition of new CTLs from the LN at rate (σ), and the loss of CTLs from circulation that exit capillaries expressing inflammatory signals and enter infected tissue (region A). Equation (4.5) describes the increase in the number of CTLs that find infected cells. This is the same as the loss term from the pool of recirculating CTLs from Equation (4.4).

We fit Model 2 to experimental numbers of CTLs in lung at various time points post infection for influenza in mice [62]. The fitting procedure found free parameters that minimized the mean squared error between the model and the data. We only considered data up to the peak of CTL activation and did not consider the decline

of CTLs after the infection is cleared.

Model 2 (Equations 4.4 and 4.5) was solved numerically using Berkeley Madonna [32]. The curve fitter option in Berkeley Madonna (Runge-Kutta 4, step size = 0.0004 sec) was used to establish the best-fit parameter estimates. The curve-fitting method uses nonlinear least-squares regression that minimizes the sum of the squared residuals between the experimental and predicted values of N_f.

Next we compared model output for mice and humans. For mice, we fixed r to 1 mm, R to 10 cm, and the recirculation time (t_{rc}) to 6 seconds. We then estimated the LN rate of output of CTLs (σ). The best fit estimate for σ was approximately 864 activated CTLs per hour. Model output is shown in Fig. 4.2 Panel B (a list of all ODE model parameters is given in Table 4.1). Numerically simulating the ODE system, we estimated the time taken for the first CTL to reach infected tissue to be approximately 15 minutes (Fig. 4.2 Panel B). Approximately 80000 CTLs find the infected region at day 5 post activation. We modeled CTL search in the human lung using the same values as in ODE Model 1 (R = 10 meters, t_{rc} = 60 seconds and σ = 45000 CTLs per hour) and numerically simulated the ODE system. The predicted time for an activated CTL to discover an infected cell in a human lung is approximately 8 hours, and the number of CTLs that reach the lung by 5 days post activation in the LN is approximately 190.

In summary, the presence of an inflammatory signal and a chemokine gradient around infected cells results in a earlier first discovery of infection by activated CTLs in both mice and humans. In mice, the first CTL with inflammation arrives in 15 minutes compared to 12 hours without it, a 48-fold speedup. The inflammation signal reduces search time in humans more than in mice: The first CTL with inflammation arrives in 8 hours compared to 90 days without it, a nearly 270-fold speedup.

Table 4.1: The parameters used in the ODE and ABM for mice with a short description of their role and default value (§ measured in human cell lines)

Description	Value	Source
Release rate of activated CTLs (σ)	$864/h$	Fit to data in [62]
CTL recirculation time (t_{rc})	$6\ s$	[47]
CTL diffusion coefficient (D)	$56(\mu m)^2/h$	Calculated from [63]
Radius of lung area (R)	$10cm$	[56]
Radius of circle lung infected area (r)	$0.1cm$	Personal observation
Length of cubic ABM simulation compartment	$2000\mu m$	Model parameter
Time between infection and secretion §	$10.5h$	[65]
Duration of productive infection §	$17.15h$	[65]
ABM virus secretion rate §	$2.6\ virions/h$	[65]
ABM CTL sensing radius	$10\mu m$	Model parameter
ABM Epithelial cell diameter	$10\mu m$	Model parameter
ABM CTL diameter	$4\mu m$	Model parameter

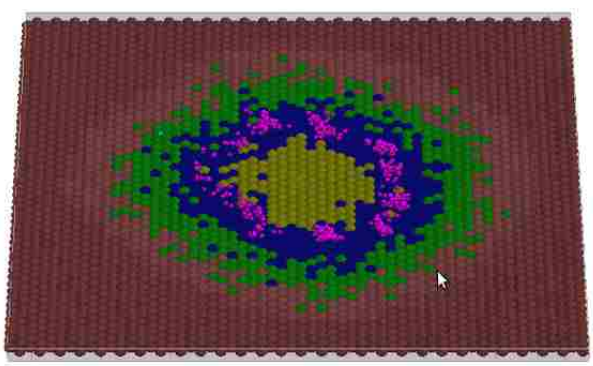

Figure 4.3: A snapshot of the CyCells ABM in action. The epithelial cell layer is made up of healthy cells (dark red), infected incubating cells (green), virus expressing cells (blue), and dead cells (yellow). The area of lighter red surrounding the infection shows that free virus particles (semi-transparent white) are present. T-cells (pink) are seen swarming over locations with high virus concentration.

4.6 Agent Based Model

The ABM extends the earlier results to consider spatial and stochastic effects of CTL migration and recirculation, also incorporating infection spread and CTL mediated

killing of infected cells. The CyCells [29, 30] modeling tool explicitly represents healthy cells, infected cells, and CTLs, and represents cytokines, chemokines, and virus as concentrations. We model the release of virions from infected cells, diffusion of chemokines and inflamatory signals, and chemotaxis of CTLs up a chemokine gradient. A screenshot of the graphical representation is shown in Fig. 4.3.

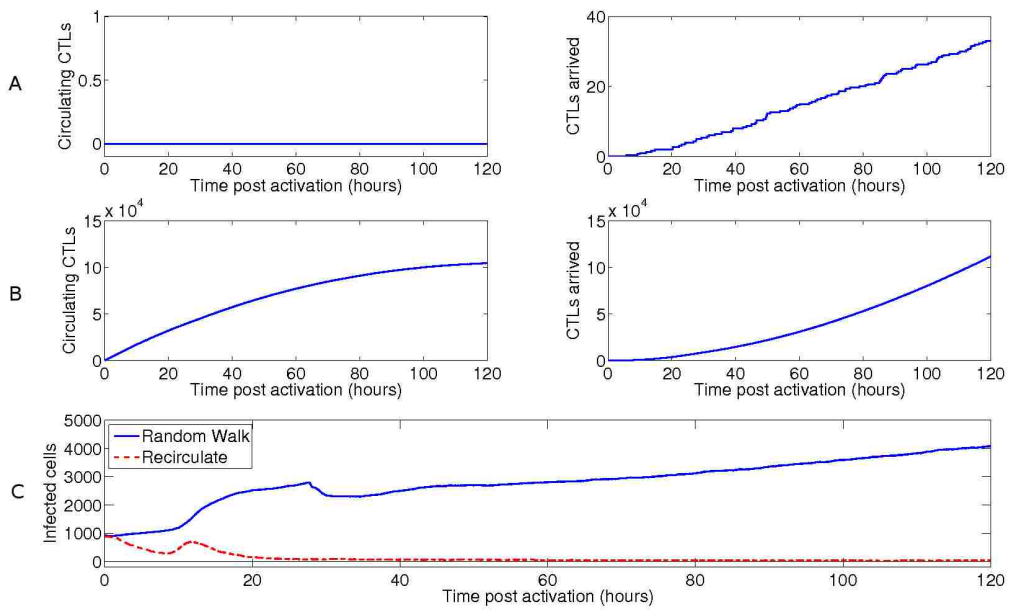

Figure 4.4: Panel A: Plot of the number of recirculating CTLs (N_c) and CTLs that have found infected cells (N_f) vs. time post activation for CTLs only walking randomly (ABM 1). Panel B: Plot of N_c and N_f vs. time for CTLs only recirculating (ABM 2). Panel C: Plot of the number of infected cells over time for ABM 1 and ABM 2. The population bumps in Panel C during the first day post activation are an artifact of the model initialization scheme and do not affect the final results.

4.6.1 ABM Model 1: Dynamics without Inflammation

We start by modelling a $2mm$ by $2mm$ grid with an area of infection that represents five days of growth in the absence of a secondary immune response. After five

days, specific CTLs become activated and enter the grid at a random location at $\sigma = 864/hour$, scaled down to adjust for the $4mm^2$ subset of the $10cm \times 10cm$ area of the mouse lung. In ABM Model 1, there is no inflammatory signal, so CTLs that enter the grid immediately exit the capillary and begin a random walk through lung tissue. Infected cells produce virions which then infect healthy cells. Virus infected cells are differentiated into two populations: infected cells that are incubating but not secreting virus, and expressing cells that are actively producing new virions. The parameters describing rate of infection of healthy cells are taken from a previous study [65] (summarized in Table 4.1). Our primary results comparing system dynamics with and without inflammation signals do not depend on these parameters.

The time taken for the first CTL to detect an infected cell is 90 minutes. 33 CTLs find the infection five days post activation (Fig. 4.4 Panel A). There are 4,077 infected cells five days post activation.

4.6.2 ABM Model 2: Dynamics with Inflammation and CTL Recirculation

Next we study an immune response with inflammatory signals. We simulated an influenza infection using the same parameters as ABM 1, but allowed CTLs to recirculate until they encountered an inflammation signal. We evaluate the value of the inflammatory signal by comparing the results of ABM 1 and ABM 2.

The time taken for the first CTL to find an infected cell is 3.3 minutes. The number of CTLs which find infected cells in 5 days is 111,572 compared to 33 in ABM 1 (Fig. 4.4 Panel C). The number of infected cells remaining in the simulation is much lower for ABM 2 (46.7) compared to ABM 1 (4,077). Hence the value of the inflammation signal is a reduction in the number of infected cells at day 5 (from approximately 4,077 without an inflammatory signal to approximately 47 with the

Table 4.2: The effect of inflammation on the time taken by CTLs to first detect infection, the number of CTLs that arrive in the infected region by day 5 post activation and the number of infected cells in the simulated lung tissue by day 5 post activation. ABM means and standard deviations are from three independent runs of each ABM.

Mice		Without Inflammation	With Inflammation	Benefit of Inflammation
Time to first detection	**ODE**	12 hr	15 min	**48**
	ABM	90 min ± 31.3 min	3.3 min ± 1.9 min	**27**
Arrived CTLs	**ODE**	10	80,000	**8,000**
	ABM	33 ± 4.6	111,572 ± 1,536	**3,380**
Infected cells	**ODE**	-	-	-
	ABM	4,077 ± 518	46.7 ± 4.7	**87**

Humans		Without Inflammation	With Inflammation	Benefit of Inflammation
Time to first detection	**ODE**	90 days	8 hr	**270**
Arrived CTLs §	**ODE**	0.05	190	**3,800**
Infected Cells §	**ODE**	-	-	-

signal).

4.7 Discussion

4.7.1 Summary of Results

In this study we used ODE and ABM models to quantify how much inflammation of infected tissue improves the adaptive immune response. This is measured in terms of three different values: how much the inflammatory signal speeds up the arrival of the first CTL at the site of infection; how much the inflammatory signal increases the number of CTLs that find the site of infection five days after CTL activation; and how much the inflammatory signal decreases the number of infected cells at five days after CTL activation. We used ODE and ABM models to quantify these improvements in mice and the results are summarized in Table 4.2. The speed up for the first CTL to arrive in the infected region in a mouse is tens of times faster in both the ODE

and ABM models. The number of CTLs that reach the infected region by day five post activation is thousands of times faster in both models. The ABM includes CTL mediated killing of infected cells and predicts that with an inflammatory signal, the number of infected cells at day five is 87 times lower.

We scaled up the ODE model to make the same predictions for the human lung which is 10,000 times larger than the mouse lung. The ODE models predict that with an inflammatory signal the speed up in arrival of the first CTL humans is 270 times faster and 3800 times more CTL arrive at the site of infection at day five. Thus, the inflammatory signal improves the CTL search much more in the human than in the mouse.

4.7.2 Caveats and Limitations

We have made many simplifying assumptions in our models. We have ignored death of activated CTLs. We have assumed that LNs produce activated CTLs at a constant rate. We have ignored the time that activated CTLs spend in transit through a capillary network before going back into circulation if there is no inflammation. Because our interest is in the effect of a single signal (the inflammation signal the causes CTL to exit circulation and enter lung tissue near the site of infection), we ignore a vast array of signaling mechanisms and complex interactions between innate and adaptive immune system cells.

However, our assumptions and simplifications do not affect our primary conclusions about the relative speed of CTL search with and without an inflammatory signal. For example including a death rate of activated CTLs would give us a slightly higher estimate of the rate at which LNs release activated CTLs (σ) which would decrease search times with and without an inflammatory signal. Incorporation of a time dependent rate (σ) would give us more accurate production rates, but, again,

this would change search times with and without an inflammatory signal in similar ways. Our conclusions that inflammation greatly speeds up CTL search in the lung depends primarily on two assumptions: first the relative speed of the random walk of CTL in the lung vs the speed of circulation, and second, the initial size of the infected region and its rate of growth.

4.7.3 Conclusions

Together, the ODE and ABM allow us to quantify the value of an information signal in biologically relevant terms. The local inflammation signal in the capillary allows search to be faster because it allows CTLs to recirculate when they arrive in capillaries in uninflamed regions of the lung. Because the lung surface area is so large, and CTL that have exited capillaries move so slowly relative to circulating CTL, this information signal drastically changes the ability of CTL to search the lung quickly. It allows CTL to effectively search the large surface area of the lung in the relatively fast flow of the blood circulatory system, and to exit only very near the site of infection. Further, because the human lung is 10,000 times larger than the mouse lung, the search for an initially small site of infection is much more difficult. This work shows that the effect of the local inflammatory signal is much larger in the search for influenza in the human lung vs the mouse lung. This suggests that the role of inflammation, chemokines and other immune signals may be different in humans and mice. Understanding these differences is important because so much knowledge of immunology and vaccine design depends on experimental work in mouse models.

The implications of this work extend beyond CTL search for influenza in the lung. An effective immune response often requires finding rare localized sites of infection. Models can make important contributions to our understanding of immune function by explaining how the multitude of immune signaling mechanisms improve such

search processes.

By understanding the role of information signals in the immune system we can build models that allow us to understand how immune systems form distributed information exchange networks to search, adapt and respond to infections. Without central control, the interactions among millions of communicating components enable immune systems to search and respond to complex, dynamic landscapes effectively. We hypothesize that ant colonies, immune systems and other complex biological systems use common informational strategies to allocate components effectively to tasks and direct their search in space [57].

Our approach may be useful for developing decentralized search in Artificial Immune Systems [54, 26]. We anticipate that a quantitative characterization of information flow and its effect on performance will help us understand why systems of different sizes and in different environments use different information, organizational structures and strategies to accomplish similar tasks.

4.8 Acknowledgements

We thank Neal Holtschulte for suggesting the use of ODEs to model recirculation. This work is supported by grants from the National Institute of Health (NIH RR018754), DARPA (P-1070-113237) and National Science Foundation (NSF EF 1038682).

Chapter 5

Estimating Biologically Relevant Parameters under Uncertainty for Within-Host West Nile Virus Infection

5.1 Abstract

West Nile virus (WNV) is a neurotropic flavivirus that has emerged globally as a significant cause of viral encephalitis. Currently, little is known about the within host viral kinetics of WNV during infection. We used a series of increasingly complex mathematical models to examine WNV dynamics in mice. To the best of our knowledge, this is the first effort to model within-host dynamics of WNV. The novelty of our approach lies in combining viremia measurements for knockout and wildtype mice by fitting a target cell limited model to knockout mice and adaptive immune response model to wildtype mice. This approach reduces the number of parame-

ters that need to be estimated by the immune response model and leads to tighter bounds on model predictions. Despite large uncertainty in model parameters, our analysis yields tight estimates of a variety of biologically relevant quantities that are composed of non-linear combinations of model parameters, e.g. the within-host basic reproductive number, R_0, is between 1.7 to 7.1, the infectious virion burst size or the average number of infectious virions released over the lifespan of a productively infected cell is between 1.8 to 12.8 plaque forming units, and the number of cells infected per infectious virion is approximately 0.9. Previous studies have demonstrated the critical role played by the humoral immune response in conferring protection in WNV infected hosts by reducing the peak viral load in blood. Not only is peak viral load an important determinant of the outcome of the infected individual, it is also a key determinant of transmission to mosquito vectors and epidemic spread. The models presented here are a first step in gaining a quantitative understanding of the role of the humoral immune response in reducing host infectivity and consequently the epidemic spread of WNV. This chapter was co-authored by Jeremie Guedj, Ruy Ribeiro, Melanie Moses and Alan S. Perelson and is being prepared for submission.

5.2 Introduction

West Nile virus (WNV) is a flavivirus that has emerged globally as a significant cause of viral encephalitis. It is maintained in an enzootic cycle between mosquitoes and birds [21] but can also infect and cause disease in horses and other vertebrates including humans. Infection of humans is associated with febrility that can progress to lethal encephalitis [66, 67, 68]. Following its introduction into the United States in 1999, WNV rapidly spread across North America, and more recently WNV has been reported in Mexico, South America, and the Caribbean [22, 23, 24]. Between 1999 and 2010, there were a total of 1.8 million illnesses in humans of which 1308

resulted in deaths [69]. Although vaccines are available for animal use, no vaccines or specific therapies for WNV are currently approved for humans [25].

WNV is an enveloped virus with a single-stranded, positive sense, 11-kb RNA genome [25]. Since it was first isolated in 1937 [70], substantial attention has been given to its structure, its genome, the mechanisms of viral entry and dissemination, the immune response it elicits and its epidemiology (reviewed in [25]). However, information regarding the kinetics of WNV infection is limited. WNV is cytopathic and initially infects epidermal Langerhans cells, which then migrate to the draining lymph node where macrophages are infected [25]. From the draining lymph node, WNV spreads to the spleen, kidney, and spinal cord and ultimately breaches the blood-brain barrier to infect neurons [25].

Viral titers in serum indicate that the peak of virus replication occurs before the virus has spread to the spleen and kidneys (analysis of data from [71]). Hence virus growth until the peak appears to be mostly driven by replication in Langerhans cells and macrophages [72]. The kinetics of WNV infection in mice is characterized by an initial exponential growth of serum virus that peaks at 3 to 4 days post infection (DPI), followed by an exponential decline that leads to undetectable levels of virus by 6 to 8 DPI.

Both T and B cell responses are important in controlling WNV infection [71, 73, 25]. Viral specific immunoglobulin M (IgM) is detected just before the virus titer peak, approximately 3 to 4 DPI, and immunoglobulin G (IgG) is detected around 8 DPI [71]. The effect of induced IgM is to lower peak viremia and reduce the time to peak viremia [71]. A cytotoxic T cell response does not appear until 6 DPI, well after the peak of virus replication[74]. Our goal is to quantitatively describe the interplay between viral dynamics and the immune response in the early phase of WNV infection.

Mathematical models have proven to be useful tools in the analysis of viral infections. For example, the dynamics of human immunodeficiency virus (HIV) infection were poorly understood until mathematical models were developed. These models were used to analyze the kinetics of viral load decline in patients under therapy and were able to estimate the rate of HIV replication, the number of virus particles produced and cleared daily, and the average life span of infected cells[75, 76, 77, 78]. Similar models have been used to analyze the effects of interferon and ribavirin on hepatitis C virus (HCV) dynamics [79, 80, 81] as well as the effect of drugs on hepatitis B virus (HBV) kinetics [82, 83, 84]. These models took advantage of the fact that HIV, HCV and HBV infection produce prolonged chronic diseases where the virus population attains steady state. Perturbation of the steady state by drug administration helped to reveal the underlying kinetics of viral production and clearance. In contrast, WNV produces an acute infection of short duration. Previous work has applied modeling strategies to understand the kinetics of acute infection in influenza [85, 86, 87]. To date there are no within host models of WNV infection.

Here, based on data obtained during experimental infection of mice, we develop kinetic models of WNV infection. We proceed systematically to estimate rates of viral replication, innate immunity and adaptive immune response. We first use empirical data to estimate a parameter characterizing the rate of clearance of WNV by innate immune responses in the first 90 minutes of infection. Next, we analyze data from a knockout experiment in which there was no humoral (IgM) response in order to characterize WNV infection dynamics in the absence of the initial adaptive response. Then we incorporate these parameters into a model to characterize the kinetics of the humoral response from experimental data in wild type mice. Using this approach we estimate some parameters in isolation, and then incorporate those parameters into a more complex model that includes an adaptive immune response. Thus, we avoid the problem of needing to fit more parameters in our final model than can be identified from the data.

We use a computationally intensive method to estimate ranges of parameters that could possibly have generated the observed viremia curves. The problem is computationally challenging since the potential parameter space is very large and tradeoffs between model parameters complicate parameter estimation. We reduce the parameter space that needs to be explored by imposing constraints from experimental data. Our computational framework incorporates the large uncertainties in imposed bounds on model parameters. We then explore this space by parameterizing our models with millions of feasible parameter combinations, and comparing the resulting predicted viremia curves to empirical data.

5.3 Materials and Methods

5.3.1 Study data

The data examined here came from three experimental infection studies of WNV[71, 73, 4]. In order to estimate the infectious viral decay rate, we use a **viral decay study** which intravenously inoculated wild type (C57BL/6) mice with 10^5 plaque forming units (PFU) of WNV 3356 NY2000 [4]. Serum was collected 5 mins, 15 mins, 45 mins and 90 mins post infection. Blood samples were centrifuged at 8,000 rpm for 5 min, and serum was collected and frozen at -80°C until tested for virus by plaque assay on Vero cells.

The second set of studies (**wildtype and knockout mouse studies**) were based on experimental infections of wildtype and IgM knockout mice. In these studies, wild type and knockout (sIgM$^{-/-}$ C57BL/6J) mice were subcutaneously inoculated with 100 PFU of a strain closely related to the one used in the viral decay study (WNV 3000.0259 NY2000) [71]. Serum was collected every other day until 10 DPI and titrated for virus by plaque assay on BHK-21 cells. The wildtype and knockout

mouse study measured viremia in terms of both viral RNA and PFU but the latter had fewer measurements. Since the viral decay study measured infectious virus (PFU), we converted all RNA measurements in the wildtype and knockout mouse study to PFU. We calculated the ratio of RNA copies per mL of blood for knockout mice to the viral titer in PFU per mL of blood for knockout mice at day 2 and 4 post infection from the experimental data. For WNV, we found that approximately 500 RNA copies on average corresponded to an infectious unit (PFU). Hence we scaled the viral measurements for wildtype mice, originally measured in RNA copies per mL of serum, to account for the fact that not all viral particles produce infections.

Finally, in order to determine the effect of the antibody response, we used an **antibody titer study** that subcutaneously inoculated wildtype (C57BL/6J) mice with 100 PFU of WNV 3000.0259 NY2000 [73]. Serum was collected every other day until 12 DPI and neutralizing antibody titers were determined by a standard plaque reduction neutralization assay [88]. The amount of antibody (measured in units of plaque reduction neutralization titer for 50% inhibition, $PRNT_{50}$) was determined.

5.3.2 Fitting models to data

The ordinary differential equations describing our viral kinetic models (Eqs. 5.1 - 5.4 and Eqs. 5.7 - 5.11) were solved numerically in Matlab [31]. The Runge-Kutta 4 method of integration was employed with a step size of 0.0004. The curve-fitting method uses nonlinear least-squares regression that minimizes the sum of the squared residuals between the experimental and predicted values of $\log_{10}$PFU/mL of serum. We weighed all the data points equally in our fitting procedure since no uncertainty was provided for the experimental viral titers.

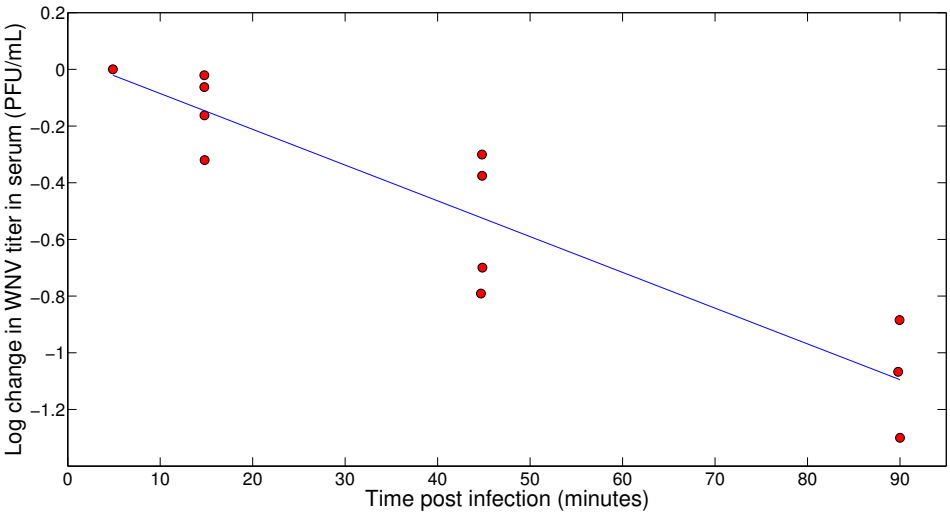

Figure 5.1: Equation 5.5 fit to data from the viral decay study [4] where viral titers in serum were measured within the first 90 minutes following intravenous inoculation of mice with WNV. Best fit using linear least-squares regression ($r^2 = 0.85$ and p-value $= 2 \times 10^{-5}$).

5.3.3 A target cell limited model

We first analyze WNV dynamics in immunodeficient (IgM knockout) mice incapable of antibody response. We assume that the infection is target-cell limited in these mice, i.e. the concentration of virus reaches a peak and then declines when few susceptible target cells remain. Models of target cell limited acute infection have been developed for both HIV [92] and influenza A virus infection [85]. Here we use a target cell limited model with an eclipse phase, given by the following differential equations:

$$\frac{dT}{dt} = -\beta TV \tag{5.1}$$

$$\frac{dI_1}{dt} = \beta TV - kI_1 \tag{5.2}$$

Table 5.1: Input parameters to model

Parameters	Description	Estimated Ranges	Source
γ	WNV clearance rate	$\leq$ 44.4/day (95% confidence interval 29.5 - 54) also varied with values 10/day, 20/day and 44.4/day	Fit to viral decay study [4]
$t_{1/2}$ $(= ln2/\gamma)$	Half-life of free virus	$\geq$ 22.5 minutes (95% confidence interval 18.5 - 33.8)	Calculated
η	Rate of IgM production	54.7/day	Fit to antibody titer study [73]
T_0	Initial target cell density	2.2×10^4 - 2.4×10^6/mL	Estimated from [89]
k	Rate of transition from I_1 to I_2	2.4 - 4/day	Estimated from [90, 91]

$$\frac{dI_2}{dt} = kI_1 - \delta I_2 \tag{5.3}$$

$$\frac{dV}{dt} = pI_2 - \gamma V - \beta TV \tag{5.4}$$

where T is the number of uninfected target cells, I_2 is the number of productively infected cells, and V is the viral titer in serum. Target cells become infected by virus at rate βTV, where β is the rate constant characterizing infection. The initial viral titer and the initial number of target cells are denoted V_0 and T_0, respectively. The initial number of infected cells is assumed to be zero. The separation of infected cells into two classes, I_1 cells that are infected but not yet producing virus and I_2 cells that produce virus, is similar to that in a model proposed earlier for influenza infection [85]. This separation increases the realism of the model, since delays in the production of virus after the time of initial infection are part of the viral life cycle

(the eclipse phase).

The parameter $1/k$ is the average transition time from I_1 to I_2. Productively infected cells (I_2) release virus at an average rate p per cell and die at rate δ per cell, where $1/\delta$ is the average life span of a productively infected cell. Free infectious virus is cleared at rate γ per infectious unit per day, for example by phagocytosis or loss of infectivity and is lost by entering cells during the infection process at rate βTV. The effects of innate immune responses and T cell responses are not explicitly described in this model, but are implicitly included in the clearance rate of virus (γ) and the death rate of infected cells (δ). Since virus requires some time to infect cells, produce progeny, and lead to the death of infected cells, immediately after intravenous inoculation virus titers decline because virus is not yet being produced but is still being cleared as described by

$$\frac{dV}{dt} = -(\gamma + \overline{\beta T_0})V \tag{5.5}$$

where $\overline{T_0}$ is the density of infectible target cells in blood and $\overline{\beta}$ is the infection rate constant of WNV for such target cells. Thus immediately after infection we expect an exponential decline in viral titer with rate $\gamma + \overline{\beta T_0}$. Viral titers in serum within the first 90 minutes following intravenous inoculation of mice with 10^5 PFU of WNV were reported in Fig. 7 of ref. [4] (viral decay study). Using this data, we estimate $\gamma + \overline{\beta T_0} = 44.4$/day (Fig. 5.1). Thus $\gamma \leq 44.4$/day and the half-life of free virus ($t_{1/2} = ln2/\gamma$) is ≥ 22 minutes.

Since the viral decay study used intravenous inoculation and measured viremia in blood until 90 minutes post infection, the infectible cell types are different from a study that uses a footpad inoculation route. It is also difficult to estimate what proportion of virus gets into organs and lymph nodes and the proportion of all infectible cells that are reached in the first 90 minutes after inoculation. Hence the

target cell density for intravenous inoculation ($\overline{T_0}$) in the viral decay study is probably different from the target cell density for footpad inoculation in the wildtype and knockout mice (T_0). Since the rate constant of infection depends on the infectible cell types, the corresponding rate constants of infection (β and $\overline{\beta}$) are also probably different in the two settings. Since we are unaware of any data that would allow us to independently estimate $\overline{\beta T_0}$, we fixed γ at various values ≤ 44.4/day and examined the sensitivity of our estimates of other model parameters to this choice. We also iterated through values of the eclipse phase duration ($1/k$) ranging from 6 hours to 10 hours and varied $1/\delta$ from 1 hour to 72 hours (see 5.3.6 Biological constraints on model parameters).

For biologically feasible combinations of parameters, we generate a viremia curve, and compare it to empirical data from the knockout mice study [71] in order to identify a set of the target cell limited model parameters (V_0, β, p and δ) that could have generated the empirical data.

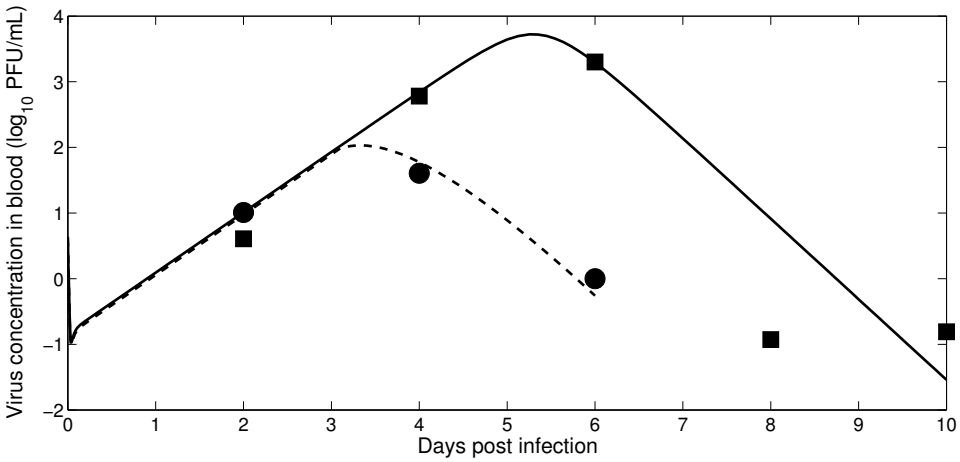

Figure 5.2: Model fit to data from wildtype and knockout study using one representative best-fit parameter estimate. The solid line is the target cell limited model fit to data (squares) from knockout mice. The dotted line is the model including a humoral response fit to data (circles) for wild type mice.

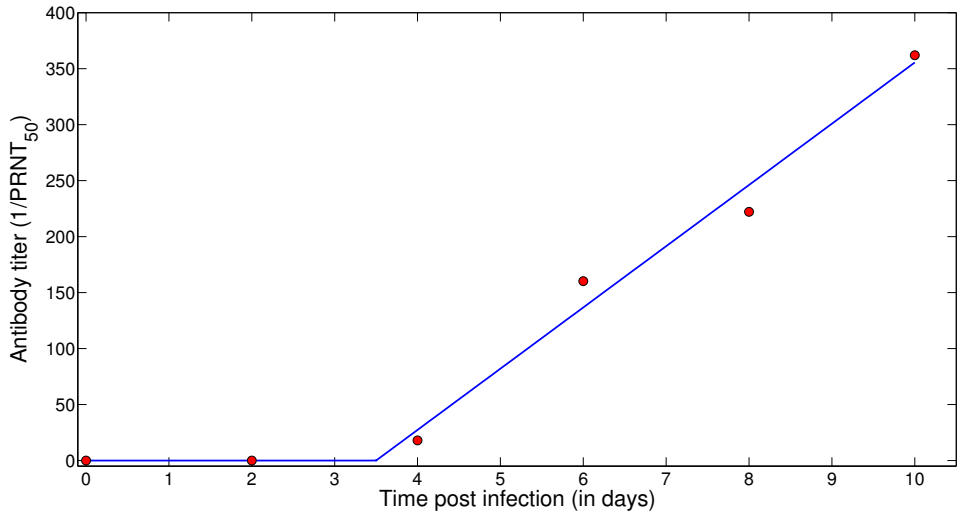

Figure 5.3: Fit of the function $A(t)$ given by Eq. 5.6 to the neutralizing antibody data (circles) from the antibody titer study.

5.3.4 Model incorporating an adaptive immune response

Humoral immunity is an essential component of the immune response to WNV, as neutralizing antibodies limit dissemination of infection [71, 73]. Diamond et al. [73] (antibody titer study) infected wild type mice subcutaneously with WNV and measured titers of neutralizing antibody as shown in Fig. 5.3. The data can be described by the following piecewise linear function:

$$A(t) = \begin{cases} 0 & , \quad t < t_i \\ \eta(t - t_i) & , \quad t \geq t_i \end{cases} \tag{5.6}$$

The level of neutralizing antibody at time t, $A(t)$, measured by the plaque reduction neutralization test (PRNT) is 0 before time t_i and increases linearly with time after that with rate η. This equation was fit to the antibody titer data (Fig. 5.3)

and η and t_i were estimated (Table 5.1).

The target cell limited model given by Eqs. 5.1-5.4 can be generalized to include neutralizing antibody. We assume that neutralizing antibody, A, binds virus, V, and neutralizes it with rate constant ρ, so that infectious virus is lost at rate $\rho A(t)V$. The model including neutralizing antibody consists of the following differential equations:

$$\frac{dT}{dt} = -\beta TV \tag{5.7}$$

$$\frac{dI_1}{dt} = \beta TV - kI_1 \tag{5.8}$$

$$\frac{dI_2}{dt} = kI_1 - \delta I_2 \tag{5.9}$$

$$\frac{dV}{dt} = pI_2 - \gamma V - \beta TV - \rho A(t)V \tag{5.10}$$

$$A(t) = \begin{cases} 0 & , \quad t < t_i \\ \eta(t - t_i) & , \quad t \geq t_i \end{cases} \tag{5.11}$$

Note that Eqs. 5.7-5.9 are the same as Eqs. 5.1-5.3. This model has many more parameters than we can estimate reliably from experimental data in wildtype mice. The basic target cell limited model (Eq. 5.1 - 5.4) has fewer parameters but is not biologically realistic for wildtype mice. Both models can fit the experimental dataset equally well. In order to reliably estimate parameters, we used a target cell limited model to analyze data from knockout mice (knockout study, [71]) in which there is no humoral response. This allowed us to estimate key parameters in a target cell limited model related to WNV replication in the absence of a humoral response. Then we applied the model incorporating a humoral immune response to analyze data obtained from wildtype mice (wildtype study, [71]), while fixing the parameters obtained from the fits to the knockout mice. This leaves fewer parameters to estimate in the model with an adaptive immune response. This unique combination

of knockout experimental data and models allows us to reliably estimate parameters for the more complex adaptive immune response model.

For the model with a humoral response, we estimated the parameters V_0, ρ and t_i. We re-estimated V_0 in this model because a different experiment was analyzed.

5.3.5 Estimation of initial target cell density (T_0)

Subcutaneously inoculated WNV initially infects Langerhans cells [93] and keratinocytes [94] in skin. Langerhans cells then migrate to the draining lymph node and lead to infection of cells that have not been definitely identified but are thought to be macrophages and follicular dendritic cells [93]. A study silencing early viral replication in dendritic cells and macrophages showed suppression of WNV replication [72] suggesting that these two populations are the major target cells for WNV.

We obtain a rough estimate of the initial density of target cells (T_0) based on several dendritic cell types. We found estimates for the number of different dendritic cell subsets ($CD8^-$, $CD8^+$ and $CD8^{int}$) 1 day after infection with mouse mammary tumor virus to be approximately 3000 in the draining popliteal lymph node [89]. Here we assume that WNV infection will lead to a similar density of lymph node dendritic cells. In order to account for other subsets of dendritic cells and macrophages, we set the number of a target cells to a value an order of magnitude higher than this (30,000). We estimate the density of target cells by multiplying the number of target cells by 22, the estimated number of lymph nodes in mice [95] and then dividing it by the total blood volume which is approximately 3 mL (the blood volume in mice is approximately 95 mL/kg of body weight [96] and the weight of C57BL/6J mice is approximately 30 grams [97]). This gives us an initial target cell density of $T_0 = 2.3 \times 10^5$/mL. Given the uncertainty in this estimate, in our analysis we vary

T_0 by an order of magnitude above and below this value.

5.3.6 Biological constraints on model parameters

In order to reduce the parameter space that needs to be explored we constrained the range of various parameters based on experimental data. We constrained the duration of the eclipse phase ($1/k$) and the duration of productive infection of an infected cell ($1/\delta$) in the following manner. The duration of the eclipse phase for neuronal cells infected in-vitro with WNV is 6 to 8 hours [91]. Experimental data in-vivo suggests that WNV completes one round of replication in dendritic cells within 12 hours in mice [90]. Hence the duration of the eclipse phase in-vivo is less than 12 hours in mice. We constrained the eclipse phase to be between 6 hours and 10 hours.

WNV infection can cause both cytolysis and profuse budding in infected cells [98]. Hence infected cells may continue to produce virus (due to viral budding) even after the first round of WNV replication. In order to simulate this, we set the upper bound on the productive lifespan of an infected cell ($1/\delta$) to 3 days. We also fixed the minimum productive lifespan of an infected cell in a model with an eclipse phase ($1/\delta$) to be 1 hour.

Bounds on the initial density of inoculated virus (V_0) were set in the following manner. The wildtype and knockout mice study inoculated 100 PFU of WNV into the mouse footpad. Assuming complete absorption into blood (3mL in mice) gives an upper bound for V_0 of approximately 33.3 PFU/mL. For the lower bound, we assume 1% absorption into whole tissue (30 mL in mice) and obtain approximately 0.01 PFU/mL.

Finally, the time of initiation of the IgM response (t_i) was constrained from the antibody titer study [73]. The study measured antibody titers on alternate days post infection and the first measurable antibody titer occurred at 4 DPI. Hence we

constrained t_i to be between 2 to 4 days.

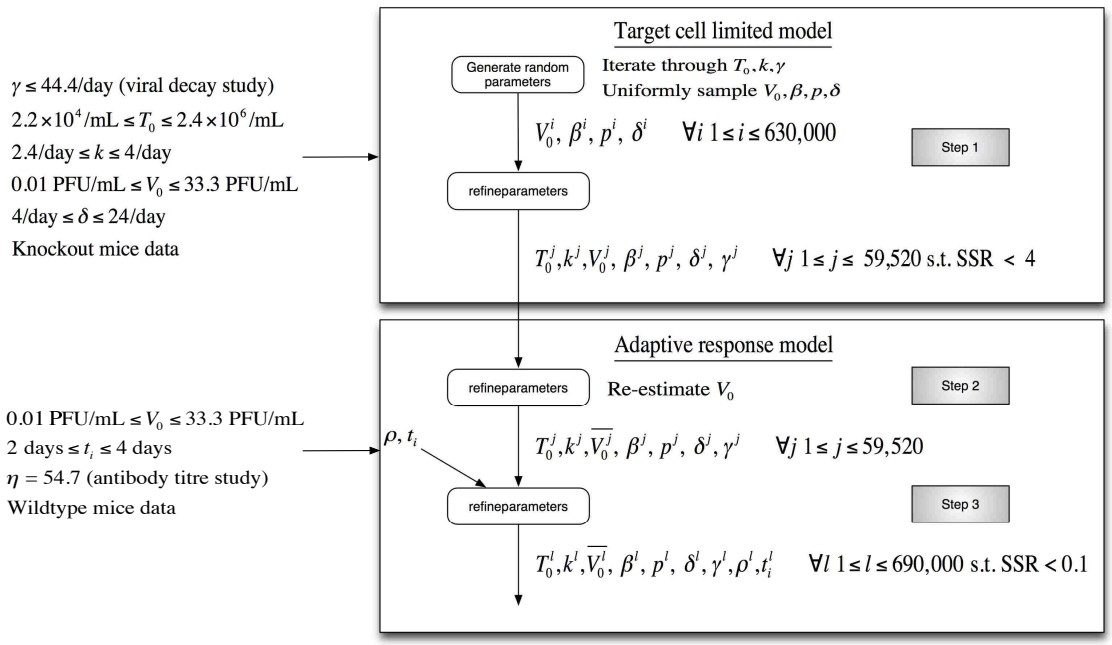

Figure 5.4: Outline of the computational approach.

5.3.7 Computational Approach

We set up a framework to explore the biologically plausible parameter space. We use a computationally intensive method to sample feasible combinations of parameters from which we generate viremia curves. We compare each curve to empirical data in order to identify a set of parameters that could have generated the empirical data.

We are interested in determining the plausible range of biological parameters and not the single set of parameters that give the best fit. Hence we do not use optimization techniques like genetic algorithms [65] but instead generate samples uniformly at random from the intervals imposed from biology. Each of these samples

was given as input to a subroutine we developed, *refineparameters*, which was used to search for parameter sets that produce viremia curves consistent with observed data. The subroutine (written in Matlab [31]) creates a search grid consisting of new guesses for model parameters centered around the initial guesses it takes as input. Each grid cell represents an initial guess which was used as input to a Matlab optimization function (*lsqcurvefit*). The grid was created by varying the guessed model parameters by a specified percentage either on the log scale or numerical scale and then combining each parameter combination with all other possible combinations of the remaining parameters. It then searched for combinations of input model parameters that generate viremia curves consistent with observed data by calling the Matlab optimization routine *lsqcurvefit* on each initial guess for model parameters represented by a grid cell. The subroutine imposes biological constraints on model parameters (described in Section 5.3.6, Biological constraints on model parameters). The computational approach is outlined in Figure 5.4. The steps of the method are:

Step 1: Iterating through values of T_0, k and γ and generating random guesses for V_0, β, p and δ. We iterated through specific values of T_0, k and γ in order to determine how those parameters affect the parameters we are interested in predicting. We varied T_0 from 2.2×10^4/mL to 2.4×10^6/mL. We varied the duration of the eclipse phase ($1/k$) from 6 to 10 hours, and we varied the viral clearance rate (γ) from 10/day to 44.4/day (Table 5.1). For each of seven values of T_0, three values of k, and three values of γ, we generated guesses uniformly at random for the parameters (V_0, β, p, δ) within their biologically realistic ranges. We divided each parameter into 10 intervals on the log scale, and generated 10 random guesses within those intervals. Each parameter value was then combined with all combinations of the remaining parameters to generate 10^4 random guesses for the parameters (V_0, β, p, δ) for each value of T_0, k and γ, giving a total of $7 \times 3 \times 3 \times 10^4 = 630,000$ random guesses. These random initial guesses were then provided to the subroutine *refineparameters*, that searched for parameter sets (V_0, β, p, δ) that produce viremia

curves consistent with observed data. We retained all solutions that yielded a sum of squared residual less than a threshold ($4[log_{10}\text{PFU/mL}]^2$) that was chosen to give visually good fits (59,520 solutions). These sets of solutions that yielded good fits to the knockout mice data were then sent as input to Step 2.

Step 2: Re-estimating V_0 for the immune response model. The sets of model parameters (V_0, β, p, δ) (59,520 solutions) estimated for the target cell limited model were then used to estimate a corresponding set of parameters (V_0, ρ, t_i) for the immune system model. For each set of model parameter estimates (β, p, δ) from the target cell limited model, the parameter V_0 was re-estimated for the immune response model since the day 2 viremia for wildtype mice was lower than the day 2 viremia for knockouts. The subroutine *refineparameters* was given the list of 59,520 solutions (V_0, β, p, δ) from Step 1. The search grid was created by varying the values of V_0 from the target cell limited model by $\pm$ 50% on the log scale with 30 samples. We took the best value of V_0 ($\overline{V_0}$) for a given combination (β, p, δ). The final output from this step is a new list of solutions ($\overline{V_0}$, β, p, δ). This gave a new set of 59,520 combinations of ($\overline{V_0}$, β, p, δ) where only $\overline{V_0}$ is re-estimated. These solutions are the input to Step 3.

Step 3: Estimating immune response parameters ρ and t_i. In this step, for each set of model parameter estimates (V_0, β, p, δ) from the output list of Step 2 (59,520 solutions), the immune response parameters (ρ, t_i) were estimated by a new call to *refineparameters*.

The subroutine *refineparameters* was given the list of all solutions ($\overline{V_0}$, β, p, δ) from Step 2. The search grid was created by varying ρ and t_i uniformly along the constraints (ρ varying from $0 - 50\text{PRNT}_{50}^{-1}\text{day}^{-1}$ and t_i trying from 2 - 4 days) and then combining each combination of ρ (25 values) with all other possible combinations of t_i (9 values). The bound on ρ was found to be sufficient since ρ co-varied with model parameters like δ on which we had good biological constraints.

From the list of $25 \times 9 \times 59,520 = 13,392,000$ solutions, we retained all solutions that yielded a sum of squared residual less than a threshold ($0.1[log_{10}\text{PFU/mL}]^2$) that was chosen to give visually good fits. This threshold is lower than the one for the target cell limited model since there are fewer data points available for the wildtype study. These sets of solutions that yielded good fits to data were then used to calculate ranges of model parameters for the immune system model (wildtype mice) (Tables 1 and 2). The final output of this step is a set of combinations of (V_0, β, p, δ, ρ, t_i) filtered by a threshold of sum of squared residuals. These sets of solutions that yielded good fits to data were then used to calculate ranges of model parameters for the knockout mice and wildtype mice (Tables 5.1 and 5.2). The computational approach is outlined in Figure 5.4.

5.4 Results

5.4.1 Target cell limited model

The estimated ranges of model parameters are shown in Tables 5.1 and 5.2. The model fit to the data using one representative best-fit parameter estimate is shown in the solid line in Fig. 5.2. The ranges of model parameters generated after varying T_0 an order of magnitude above and below the default value (2.3×10^5/mL) and varying $1/k$ from 6 to 10 hours are reported in Tables 5.1 and 5.2, and the histograms of the estimated model parameters are shown in Fig. 5.6.

Despite considerable uncertainty in imposed bounds on model parameters (the initial target cell density, T_0, is allowed to vary by two orders of magnitude), we are still able to calculate biologically relevant quantities with tight bounds. The infectious virion burst size (p/δ) or the average number of infectious virions released over the lifespan of a productively infected cell was estimated to be between 1.8 and 12.8

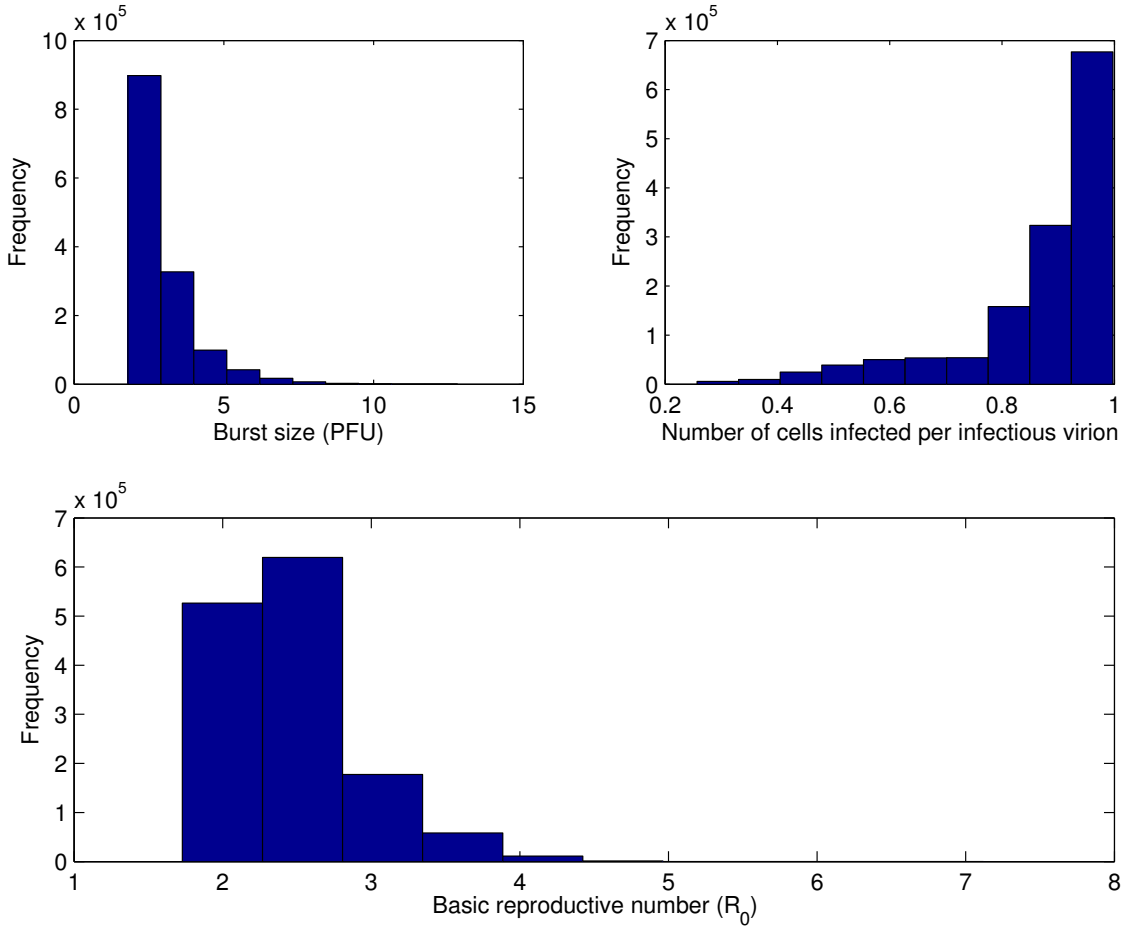

Figure 5.5: Histograms of biologically relevant quantities estimated by our approach. Top Left - Infectious virion burst size (in PFU). Top Right - Average number of cells infected per infectious virion. Bottom - Basic reproductive number (R_0).

PFU. Since we estimated the ratio of WNV RNA copies to PFU to be approximately 500, this implies that on average an infected cell produces approximately 900 to 6400 RNA copies over its productively infected lifetime. We also estimated the average number of cells infected by an infectious virion ($\beta T_0/(\gamma+\beta\cdot T_0)$) to be approximately 0.9. Even though our model parameter estimates (like the productively infected cell lifetime, $1/\delta$) are no tighter than the imposed biological constraints, we are still able

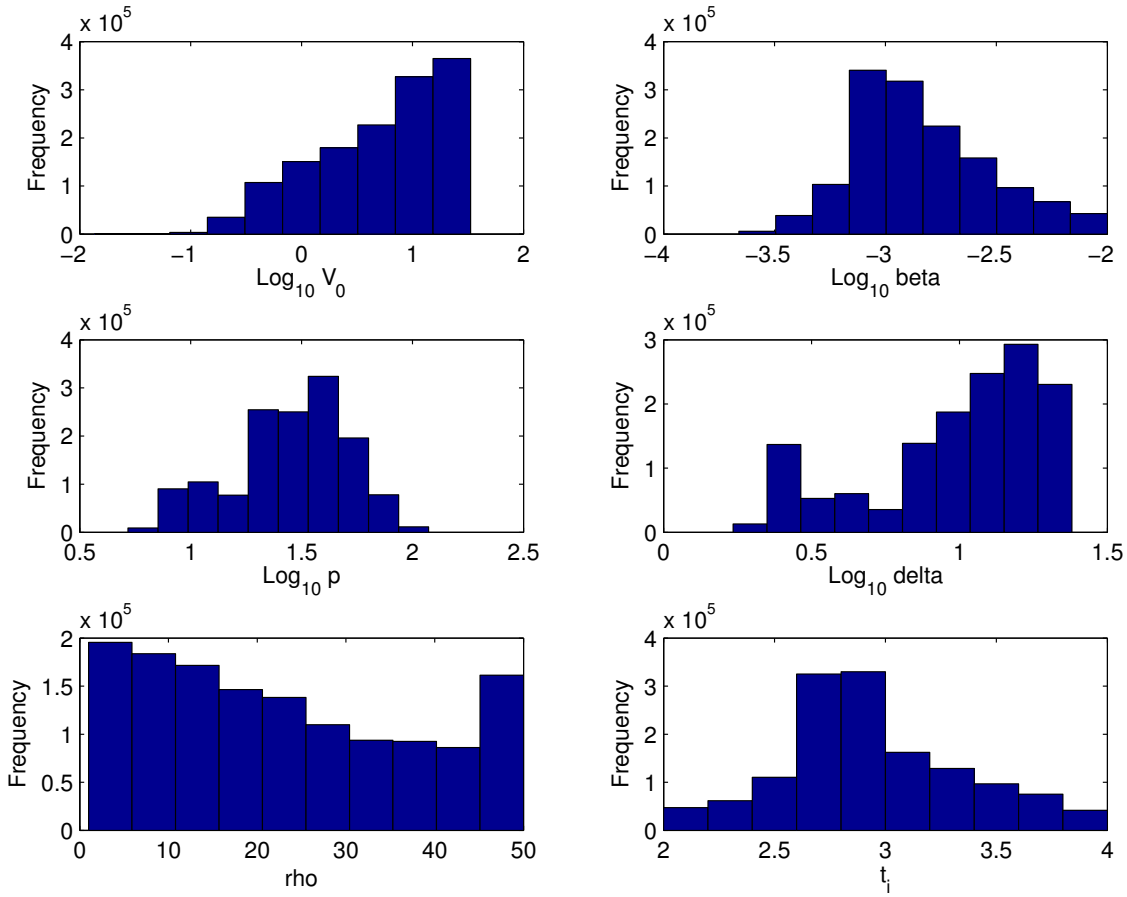

Figure 5.6: Histograms of estimated model parameters (V_0, β, p, δ, ρ, t_i) from the target cell limited model and model with humoral response.

to predict biologically relevant quantities with reasonable precision.

We also estimated the basic reproductive number (R_0). This number represents the average number of second generation infections produced by a single infected cell placed in a population of susceptible cells. If R_0 is greater than 1, then an infection can be established, whereas an infection rapidly dies out if R_0 is less than 1. For the target cell limited model (Eqs. 5.1-5.4), R_0 is given by [99]:

$$R_0 = \frac{p\beta T_0}{\delta(\gamma + \beta \cdot T_0)} \tag{5.12}$$

Using Eq. 5.12 we estimated the value of R_0 to be between 1.7 and 7.1 with an average of 2.5 (Table 5.2).

Despite considerable variation in individual model parameters, the estimates of the biologically relevant quantities like the basic reproductive number, burst size and number of cells infected by an infectious virion are tightly bound (Fig. 5.5). These biologically relevant quantities are combinations of model parameters. Fitting the model to data reveals correlations between model parameters (Fig. 5.7). Without the fitting of models to data and with the imposed biological constraints, we would expect the basic reproductive number to vary from 1 to 30 (variation with fitting is 1.7 to 7.1) (Fig. 5.5). Similarly we would expect the infectious virion burst size to vary from 1 to 30 PFU (variation with fitting is 1.8 to 12.8 PFU) (Fig. 5.5).

We observed that model parameters had tradeoffs with each other (Fig. 5.7). This precluded estimation of unique values for the model parameters. However this also helped us to constrain additional model parameters, since they depend on parameters that we could put experimental bounds on. For example, the rate constant for infection β, for which we have no experimental bounds, has a statistically significant relationship with the initial density of inoculated virus, V_0 (Fig. 5.7, p-value < 0.001, $r^2 = 0.12$). The experimental bounds on V_0 constrain feasible values of β.

Additionally, the virus production rate, p, has a statistically significant relationship with the productively infected cell death rate, δ (Fig. 5.7, p-value $= 0$, $r^2 = 0.27$). Such tradeoffs preclude estimation of unique model parameter values and imply that there is a family of solutions. The estimated ranges of model parameters in conjunction with the correlation plots between model parameters define the family of solutions that have good fits to data.

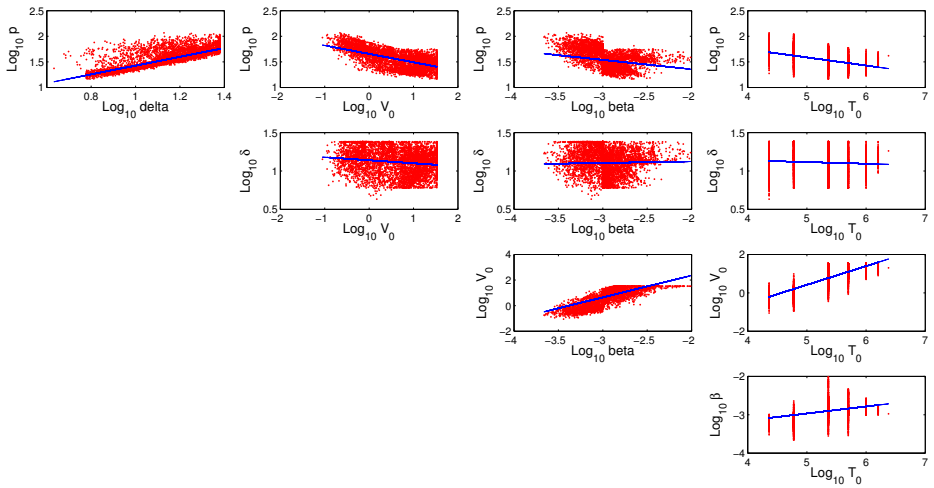

Figure 5.7: Correlation between target cell limited model parameters (T_0, V_0, β, p, δ).

Table 5.2: Imposed biological constraints and estimated output ranges, mean and standard deviation of model parameters

Statistic	V_0	β	δ	p	ρ	t_i	R_0	p/δ
Bound	[0.01, 33.3]	$[10^{-5}, 10^{-2}]$	[0.3, 24]	[0.3, 120]	[1, 50]	[2, 4]	[1, 30]	[1, 30]
Range	[0.01, 33.3]	$[2 \times 10^{-4}, 9 \times 10^{-2}]$	[1.7, 24]	[5.2, 118.2]	[1, 50]	[2, 4]	[1.7, 7.1]	[1.8, 12.8]
Mean	5.2	1.5×10^{-3}	9.9	28.1	22.7	2.9	2.5	3
SD	4	2	2	1.8	15	0.4	0.4	1

where bounds are the imposed biological constraints, range is the minimum and maximum estimated value, mean and SD (standard deviation) are of parameter estimates, V_0 is the inoculated virus density (PFU/mL), β is the rate constant of infection [(PFU/mL)$^{-1}$day^{-1}], δ is the death rate of productively infected cells (day^{-1}), p is the virus production rate (PFU/mL), ρ is the efficacy of antibody neutralization (PRNT_{50}^{-1}day^{-1}), t_i is the time of initiation of IgM response (days post infection), R_0 is the basic reproductive number (Eq. 5.12) and p/δ is the infectious burst size (average number of virus particles produced over the lifetime of an infected cell, PFU)

5.4.2 Model incorporating an adaptive immune response

The model with an adaptive antibody response has two additional parameters, ρ (efficacy of adaptive IgM neutralization, $\text{PRNT}_{50}^{-1}\text{day}^{-1}$) and t_i (the time of initiation of the adaptive IgM response, days). The initial density of inoculated virus, V_0, is also re-estimated. The best-fit ranges of these parameters are given in Table 5.2. The model fit to the data using one representative best-fit parameter estimate is shown by the dotted line in Fig. 5.2.

5.4.3 Caveats and Limitations

Our adaptive immune response model combines data from two different strains of mice (both conducted in the Diamond lab under the same experimental conditions). We assume that the parameters β, p, δ estimated from the target cell model are unchanged in the wild type mice with an IgM immune response. All variation in viremia prior to the peak is attributed to differences in the inoculated dose (V_0). Additionally, combining data from the two mice strain studies required us to convert the RNA measure from the wildtype and knockout study [71] into a PFU measure used in the viral decay study [4] (detailed in Study Data).

We also eliminate parameter values that generate viremia curves with sum of squared residuals above a threshold. Our thresholds are chosen based on visual fit, which is subjective. Finally, in our calculation of biological bounds on productively infected cell lifetimes, we assume that WNV is cytopathic in-vivo and that an infected cell is lysed after WNV completes one round of replication. WNV has been shown to be cytopathic in-vitro in K562, Neuro 2a [100] and neuronal cells [101]. However WNV infection in-vitro is cytopathic only at low infectious doses in another cell line (Vero cells) [98].

5.5 Discussion

Here we describe a method to predict biologically relevant quantities for WNV while having large uncertainty in biological bounds imposed on model parameters. We use a novel approach to combine knockout experimental data and mathematical models. A humoral immune response contributes to the successful clearing of WNV infection [71]. However a mathematical model incorporating a humoral response has many more parameters than we can estimate reliably from the available experimental data in wildtype mice. A basic target cell limited model has fewer parameters but fails to capture a progressively increasing rate of virus clearance due to a humoral response. Both models can fit the experimental dataset equally well. In order to reliably estimate parameters, we first analyzed data from knockout mice (using a target cell limited model) in which there is no anti-WNV IgM response, and hence no IgM-IgG switch to produce a primary IgG response [35]. This allowed us to estimate key parameters in a target cell limited model related to pathogen replication in the absence of a humoral response. Then we applied a more sophisticated model incorporating a humoral immune response to analyze data from wildtype mice while fixing the parameters obtained from the fits to the knockout mice. This allowed us to estimate (fewer) parameters related to the adaptive immune response. Hence this unique combination of knockout experimental data and models allows us to reliably estimate model parameters.

We then set up a framework to explore large parameter spaces after imposing constraints from biology. There is considerable variation in model parameters even after imposing biological constraints, e.g. the initial density of target cells, T_0, is allowed to vary by two orders of magnitude. The optimization routine, which generates best-fit model parameters, is sensitive to the initial guesses for parameters provided to it. Hence we sample model parameters (V_0, β, p and δ) uniformly at random from the imposed biological ranges and these randomly generated parameters are used as

initial guesses for the optimization routine. Finally we select those model parameters that give predictions consistent with our goodness of fit threshold. The problem of estimating the ranges of model parameters is computationally challenging since this requires solving differential equations millions of times. Such computationally hard problems have been solved using other approaches in other diseases [102, 103, 104].

Despite considerable variation in model parameters (the initial target cell density, T_0, is varied by two orders of magnitude), we are able to calculate biologically relevant quantities with tight bounds. We calculated the basic reproductive number, R_0, which indicated that a single infected cell produces between 1.7 to 7.1 new infections. The infectious virion burst size (p/δ) or the average number of infectious virions released over the lifespan of a productively infected cell was estimated to be between 1.8 and 12.8 PFU. Since we estimated the ratio of WNV RNA copies to PFU to be approximately 500, this implies that on average a productively infected cell produces approximately 900 to 6400 RNA copies over its productively infected lifetime. Finally, we also estimated the average number of target cells infected by an infectious virion ($\beta T_0/(\gamma + \beta \cdot T_0)$) to be approximately 0.9. Even though our individual model parameter estimates (like the productively infected cell lifetime, $1/\delta$) are no tighter than the imposed biological constraints, we are able to predict biologically relevant quantities with reasonable precision.

How are we able to predict biologically relevant quantities with certainty even though there is uncertainty around model input parameters? Fitting the model to data produces combinations of parameters that can explain the data. The fitting process eliminates combinations of model parameters that cannot explain the data and hence reveals correlations between estimated model parameters. The biologically relevant quantities are combinations of model parameters. Without the fitting of models to data and with the imposed biological constraints, we initially guessed that the basic reproductive number, R_0, could vary from 1 to 30 (variation with fitting is

1.7 to 7.1) and the infectious virion burst size could vary from 1 to 30 PFU (variation with fitting is 1.8 to 12.8 PFU) (Fig. 5.5).

We examined the dependence of model parameters on each other and observed trade offs between model parameters. (Figure 5.7). This would normally complicate parameter estimation, but we used this to further constrain model parameters on which we have no known constraints. For example, increasing the infectious virus production rate (p) tended to increase the estimated productively infected cell death rate (δ). This is not surprising since the same total count of virus production per cell can be achieved by increasing p but having the cells live a shorter time, i.e., also increasing δ. There are biological bounds on many of these parameters and we used the fact that parameter estimates are correlated to constrain parameters for which we do not have biological constraints (like the production rate p). In the previous example, we have good bounds on δ and since p and δ are correlated, we could put bounds on p also.

Our method of estimating biologically relevant quantities despite uncertainty in imposed bounds on model parameters could be more generally applicable to modeling of other diseases where it is difficult to impose tight biological bounds on parameters. We may be able to predict biologically relevant quantities for other pathogens with a lot more certainty than individual model parameters. The process of fitting models to data should reveal parameter correlations. Such correlations between model parameters help our computational framework find tighter constraints within the imposed biological bounds.

Our modeling makes suggestions for further experimental work. More frequent measurement of viremia and in-vitro measurements of infectious virus decay and the viral production rate would give more accurate parameter estimates. In-vitro experiments where the initial target cell density, T_0, can be accurately measured would help in getting precise estimates of parameters that vary with it, like the

infected cell death rate, δ (Figure 5.7).

The humoral immune response has a critical role in conferring protection in WNV infected hosts [71]. It reduces the peak viral concentration in blood as well as the time taken to reach peak viremia. Peak viremia is an important epidemiological determinant for the spread of WNV [5], which is mosquito vector borne. Above a threshold peak viremia of 10^5 PFU/mL of blood, a host is capable of infecting an uninfected mosquito, which in turn can infect other uninfected hosts and maintain WNV in an enzootic cycle [5]. Hence hosts that can sustain peak viremia above this threshold and for a longer duration are pathogen reservoirs. As evidenced in Fig. 5.2, in the presence of an induced IgM response the peak viremia and the time to peak viremia are both reduced compared with the kinetics seen in the IgM deficient mice. The models presented here are a first step towards a quantitative understanding of the role of the humoral immune response in reducing host infectivity and the epidemic spread of WNV.

5.6 Acknowledgments

We thank Dr. Michael Diamond for sharing his experimental data with us. Portions of this work were performed under the auspices of the U.S. Department of Energy under contract DE-AC52-06NA25396 and supported by NIH grants AI078881, AI028433, the National Center for Research Resources and the Office of Research Infrastructure Programs (ORIP) through grant 8R01-OD011095-21, contract HHSN 272201000055C, grants from the National Institute of Health (NIH RR018754) under the UNM COBRE Center for Evolutionary and Theoretical Immunology, DARPA (P-1070-113237) and National Science Foundation (NSF EF 1038682).

Chapter 6

A Proof of Concept for Multi-Level Hierarchical Bayesian Estimates of Within-Host Viral Dynamics

6.1 Introduction

Multilevel models like hierarchical Bayesian models reduce estimation error when they are informed by group level knowledge [13]. Hierarchical Bayesian models take between and within subject variation into account simultaneously. These models pool information across disparate individuals from different groups and are well suited for cases where there are a limited number of observations from several individuals. Hierarchical Bayesian models have been used in image processing [14], ecological modeling [15] and climate modeling [16]. Bayesian non-linear mixed effects models with a single level of hierarchy have been applied to modeling of the within-host response to

HIV [17, 18] and influenza [19]. However to the best of our knowledge, Bayesian non-linear mixed effects models with multiple levels of hierarchy have not been applied to within-host modeling. Multilevel data fitting approaches and Bayesian frameworks are expected to be helpful to modeling within-host viral dynamics [20].

We use a multi-level hierarchical Bayesian model that has three taxonomic levels and is a natural fit to the hierarchical structure of experimental data. Phylogeny and life history are important determinants of the pathogenesis of WNV. Passerine species sustain more viremia than non-Passerine species [5]. Old World species are more susceptible to WNV infection than New World species [105]. We aim to use hierarchy to make better estimates of biologically relevant quantities for WNV. Using a very simple model operating on simulated data, this chapter compares a multi-level hierarchical Bayesian non-linear mixed effects model to an aggregated Bayesian model. We compare estimates of Ordinary Differential Equation (ODE) model parameters in hierarchical versus aggregated models.

Hierarchical Bayesian models encapsulate knowledge about the underlying biology as priors. Suitable priors in a hierarchical Bayesian framework can help reduce variance of parameter estimates [13]. In some cases use of prior information can help identify parameters that otherwise might be unidentifiable [18]. A model that incorporates the hierarchal nature of phylogeny, life history and mass of infected species, and encodes this information as priors in a hierarchical Bayesian model may enable more accurate estimates of parameters characterizing WNV infection.

Modeling of biological systems is complicated by the effects of noisy experimental data and the difficulty of creating models that completely capture biological realism. In order to control the effect of noisy data and model uncertainty, this chapter uses a known model to generate simulated data with varying amounts of noise. The hierarchical Bayesian model then incorporates known information about differences between species as priors and then infers the model parameters. The accuracy of the

Bayesian model can be calculated by comparing its parameter estimates to the actual parameter values (ground truth). Given known data, this chapter focuses on the circumstances under which a hierarchical Bayesian approach (with prior information) can generate more accurate estimates of model parameters than simple Bayesian models.

This chapter aims to refine and validate the hierarchical Bayesian models to be used in the next chapter, which will use these models on actual experimental data. The goals of this chapter are:

1. To implement a novel multi-level hierarchical Bayesian model to estimate parameters in a mathematical model of viral dynamics.

2. To outline the circumstances under which a multi-level hierarchical Bayesian model with biologically motivated priors can generate more accurate estimates of parameters (in a simpified viral dynamics model) than aggregated Bayesian models without hierarchy. The models are compared based on the accuracy of estimated parameters at different levels of the hierarchy. We use the sum of squared residuals between model predicted values and ground truth values to measure accuracy.

3. Provide a foundation to test model parameters characterizing WNV infection and host immune response for dependence on host body mass. The following chapter (Chapter 7) will use a multi-level Bayesian model to estimate parameters characterizing WNV infection from real experimental data.

6.2 Materials and Methods

6.2.1 Overview of Methods

The Bayesian inference approach can be described as follows. Assume that a model (in our case a differential equation model describing how virus concentration changes over time in serum) is represented by parameters Θ. The Bayesian approach allows us to include prior knowledge about model parameters in a systematic fashion. If we have information about Θ (e.g., from experimental evidence) which needs to be incorporated in our analysis, this is represented as a prior probability distribution $P(\Theta)$. Bayes Rule allows us to incorporate the prior knowledge about parameters, $P(\Theta)$, and experimental data, D, to derive a posterior distribution of parameters:

$$P(\Theta|D) = \frac{P(D|\Theta) \cdot P(\Theta)}{P(D)} \tag{6.1}$$

The multi-level hierarchical Bayesian model mimics the hierarchical nature of phylogeny. There are three levels in the hierarchical tree representation: individual, species and genus (Fig. 6.3). Each level of the tree has an equation describing the distribution of model parameters (differential equation model, Eq. 6.2). The differential equation and hierarchical Bayesian models are explained in greater detail in the next section.

Our goal is to compare two different hierarchical Bayesian models: a multi-level model that has three levels of hierarchy (individual, species and genus) (Fig. 6.3) and an aggregated model with two levels of hierarchy (all individuals of all species pooled together under a single genus) (Fig. 6.2). We compare the accuracy of parameter estimates with respect to ground truth at the individual, species and genus level. We also experiment with different degrees of variation of parameters between species

and within species.

6.2.2 Ordinary Differential Equation Model

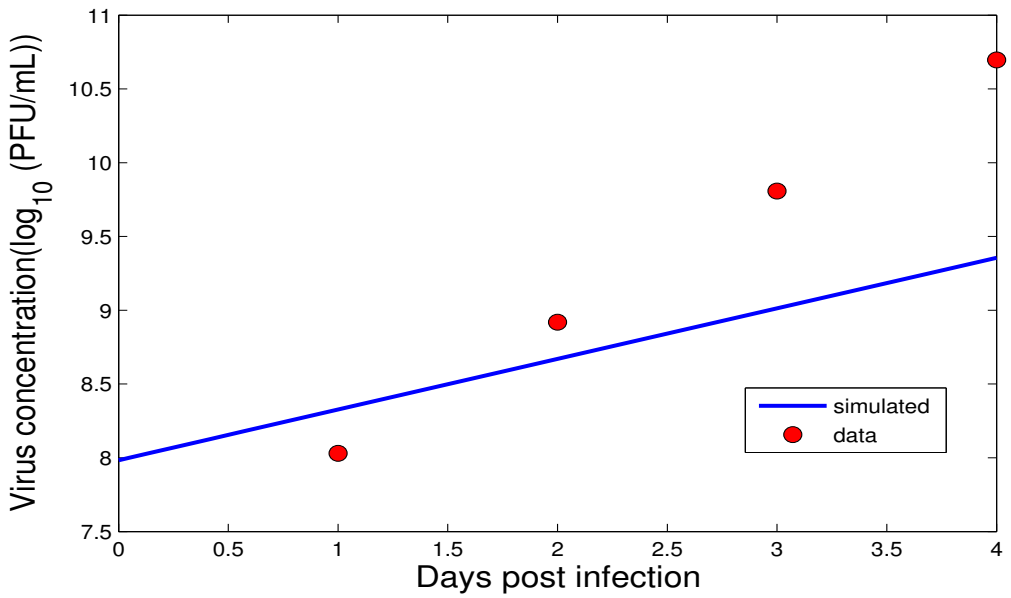

Figure 6.1: A sample ODE prediction for virus concentration (in log_{10} PFU/mL) over time post infection (line) and simulated ground truth virus concentration (points).

We use a very simple model that simulates only viremia in serum, given by the following differential equation:

$$\frac{dV}{dt} = a \cdot V \tag{6.2}$$

where V is the viral titer in serum in PFU/mL for a particular avian species. The rate of increase in viral titer is given by a. The initial viral titer is denoted V_0. The mass of the avian species is given by M. Assuming that an initial mosquito

inoculated dose (V_{dose}, in PFU) is diluted in the whole body, gives the relationship $V_0 = V_{dose}/M$. The Bayesian model infers (V_{dose},a,M) from the viral titer data. The ordinary differential equations describing our viral kinetic models were solved numerically in Matlab [31]. The Runge-Kutta 4 method of integration was employed with a step size of 0.0004. Fig. 6.1 shows a sample plot of the ODE prediction of virus concentration over time compared to simulated viral concentration reported every day for four days. All model parameters and virus concentration are logged (base 10) in order to stabilize variance and ensure positive estimates from the Bayesian inference.

6.2.3 Simulated Data

Table 6.1: Different combinations of between and within species variance

Variance	High within species variance	Low within species variance
High between species variance	(2.5,2.5)	(2.5,0.5)
Low between species variance	(0.5,2.5)	(0.5,0.5)

Number denotes variance on log_{10} scale

We generated simulated data in which viral titer increases with time as the infection progresses. We simulate data for 10 distinct groups (species) each having 3 individuals (for a total of 30 individuals). The initial mosquito inoculated dose, V_{dose}, is generated for the individuals by 30 independent draws from a normal distribution $Normal(3.6, 1)$ (where p is the mean and q the variance in a normal distribution $Normal(p, q)$). We combined two levels of between-species variance with two levels of within-species variance to generate 4 sets of simulated viral titer data (Table 6.1). Each simulated dataset was generated in the following manner: we drew 10 species-level values from a distribution based on a particular value of between-species variance; centered around each of these 10 values, we drew 3 more individual-level

values based on the chosen value of within-species variance. This process yields 30 values (10 species each having 3 individuals) of ODE parameters, which are then given to an ODE solver. The ODE solver generates a virus concentration that varies over time (post infection) from which we take four samples to generate our ground truth data.

All draws of (V_{dose},a,M) are independent of each other in the data generation process. Each individual has its own set of parameters (V_{dose},a,M), which are then given to the ODE solver that generates sampled data points from a simulated virus curve. The data generation process produces a different virus titer curve for each individual.

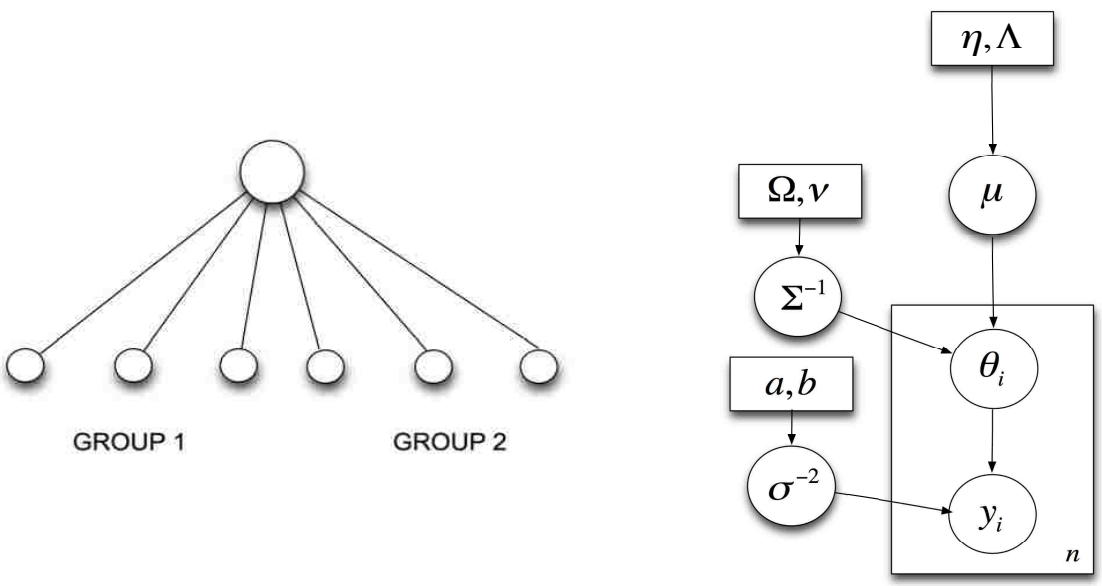

Figure 6.2: Left Panel: Aggregated model with two groups combined. Each group has three individuals. Also shown are the genus, species and individual levels. Right Panel: Plate diagram for the aggregated model. The plate denotes iteration of parameters and the number in the plate shows the number of iterations.

6.2.4 Constraints on Model Parameters

The initial viral titer, V_{dose}, is constrained to be within 3 and 3×10^4 PFU/mL. The rate of increase in viral titer, a, is constrained to lie within 0.01 and 100 /day, and the mass, M, is constrained to be between 10^{-20} and 10^{20} kg.

6.2.5 Hierarchical Bayesian Model

Aggregated model

Given a population of individuals that belong to the same group, the hierarchical Bayesian model assumes that the dynamics of infection of each individual is characterized by parameters (θ_i to θ_n for n individuals) that are drawn from a common species-level distribution (μ).

The aggregated model has 10 species of 3 individuals each. The species are aggregated to form a tree of height 2. The model is shown graphically in Fig. 6.2 (Left panel). There are two levels in the hierarchical tree representation: individual and all species combined into a single genus. Each level of the tree has an equation describing the distribution of ODE model parameters (Eq. 6.2). The ith individual has a parameter θ_i that represents the mean of (V_{dose},a,M) for a particular individual. This parameter θ_i is then drawn from the genus level distribution (all species aggregated) with mean μ. The mathematical details of the aggregated model are given in Appendix A.

Multi-level hierarchical model

We also implemented a novel multi-level hierarchical model that has 3 taxonomic levels and is a natural fit to the hierarchical structure of the data. This model has

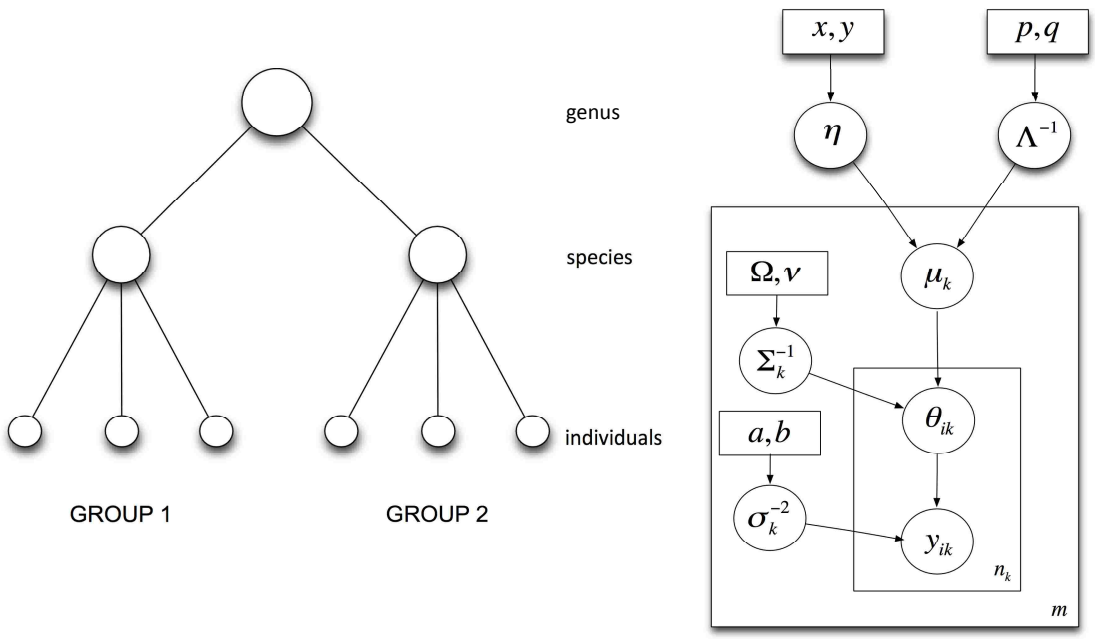

Figure 6.3: Left Panel: Multi-level hierarchical model with two groups. Each group has three individuals. Also shown are the genus, species and individual levels. Right Panel: Plate diagram for the multi-level hierarchical model. The plate denotes iteration of parameters and the number enclosed in the plate shows the number of iterations.

10 groups (species) of 3 individuals each. The groups are arranged hierarchically to form a tree of height 3. The model is shown graphically in Fig. 6.3 (Left panel) with three levels in the hierarchical tree representation: individual, species and genus (Fig. 6.3, Right panel). Each level of the tree has an equation describing the distribution of ODE model parameters (Eq. 6.2). The ith individual has a parameter θ_i that represents the mean of (V_{dose},a,M) for a particular individual. This parameter θ_i is then drawn from a species-level distribution with mean μ. Finally, the species-level estimate is itself drawn from a genus-level distribution centered around η. The mathematical details of the multi-level model are given in Appendix B.

MCMC implementation

We are interested in inferring the posterior distribution of ODE parameters given data ($P(\Theta|D)$, Eq. 6.1). However the distribution does not have an analytic form. MCMC techniques enable us to sample from a target distribution; the approximation gets better as more samples are drawn. We combine the Metropolis-Hastings algorithm and the Gibbs sampler. The Gibbs sampler is a type of MCMC algorithm that divides the parameters into a number of components and at each iteration sequentially updates each of them by conditioning on the others. The Metropolis-Hastings (M-H) algorithm updates Θ, and the Gibbs sampler updates all the remaining variables. We use a blockwise update scheme where proposed new values of parameters (from the M-H algorithm) are either all updated simultaneously or all reverted to their previous values. The M-H algorithm draws a subsequent sample from the target distribution centered around a proposal distribution. Our proposal distribution is a multi-variate normal distribution centered around the current value of θ_i.

The choice of dispersion of the proposal distribution is important. If the dispersion is high, many MCMC moves will be rejected and the procedure will take longer to converge. If the dispersion is low, the chain may not explore the parameter space thoroughly [106, 107]. The standard deviation of the proposal distribution is chosen to be 0.01 on the log scale (base 10) for all the parameters. If a value returned by the proposal distribution is outside of the imposed bounds for ODE parameters, we reflect the value back into range. Convergence is checked informally based on graphical techniques [108].

All models were run for 3,000 iterations. This constitutes a single "run" of the Bayesian model. One run of the Bayesian model may be more efficient when a number of initial samples are discarded (burn-in) and when some number of consecutive samples are not considered (thinning) [106]. The initial 300 iterations were discarded

(burn-in phase). Of the remaining 2,700 samples we retained every fifth sample. The same random number seed was used for both the models.

6.3 Results

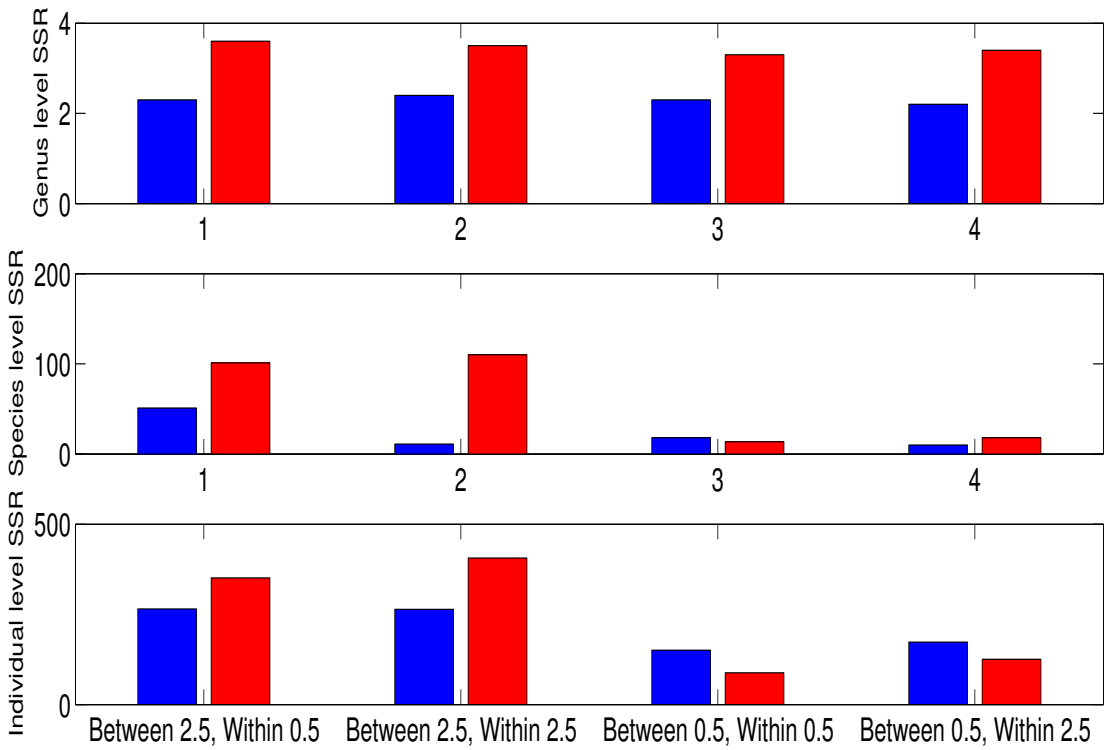

Figure 6.4: Performance on predicting genus, species and individual mean for ODE parameter M: Multi-level model (blue) vs. aggregated model (red). Y-axis - sum of squared residuals between predicted mean and actual mean (ground truth), X-axis - variance between and within species (log scale) as described in Table 6.1.

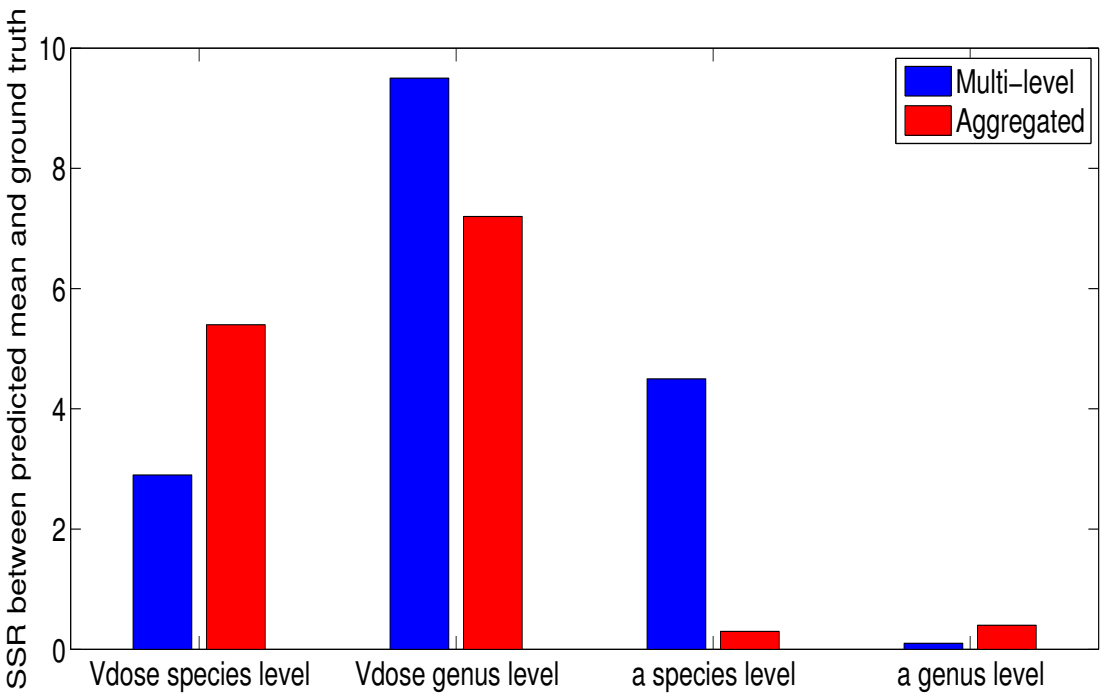

Figure 6.5: Performance on predicting species and genus level means for ODE parameters V_{dose} and a when there is high between-group and low within-group variance in M: Multi-level model (blue) vs. aggregated model (red). Y-axis - sum of squared residuals between predicted mean and actual mean (ground truth).

6.3.1 Estimates for ODE parameter M

The data generation phase produces ODE parameters by drawing from normal distributions with known mean and variance (ground truth). The exact values of ODE parameters generated from the probabilistic draw constitute the sample truth.

Fig. 6.4 demonstrates the performance (defined as the sum of squared residuals between predicted mean and actual mean) of the multi-level and aggregated models at predicting genus, species and individual level means for the parameter M. All analysis presented in the tables is from the same run.

We look at 4 different datasets that have varying amounts of between and within species variation (shown in Table 6.1). The species-level performance is measured by summing the sum of squared residuals between actual and predicted means over all species. Similarly, the individual-level performance is measured by summing the sum of squared residuals between actual and predicted means over all individual.

The multi-level model consistently makes better predictions of the genus level mean value of M than its counterpart, regardless of the amount of variation between and within species, as evidenced by lower sum of squared residuals for blue bars (Fig. 6.4).

We observe that if there is high between-group and low within-group variance in M (Fig. 6.4), the multi-level model makes better predictions of ground truth at the genus, species and individual levels than the aggregated model. In fact, given large variation between species, the multi-level model appears to make more accurate predictions at all levels. However, the aggregated model makes better predictions at the species and individual level when there is less variation between species.

6.3.2 Estimates for ODE parameter V_{dose}

Fig. 6.5 shows the sum of squared residuals between predicted and actual mean at the species and genus level for V_{dose}. The results shown here are for the case where there is high between-group variance and low within-group variance in M. We focus on this case because we expect our actual experimental data (Chapter 7) to have high between-group and low within-group variance. The multi-level model performs better at predicting species level means but is outperformed by the aggregated model at the genus level. The results for V_{dose} were similar given other variations in M.

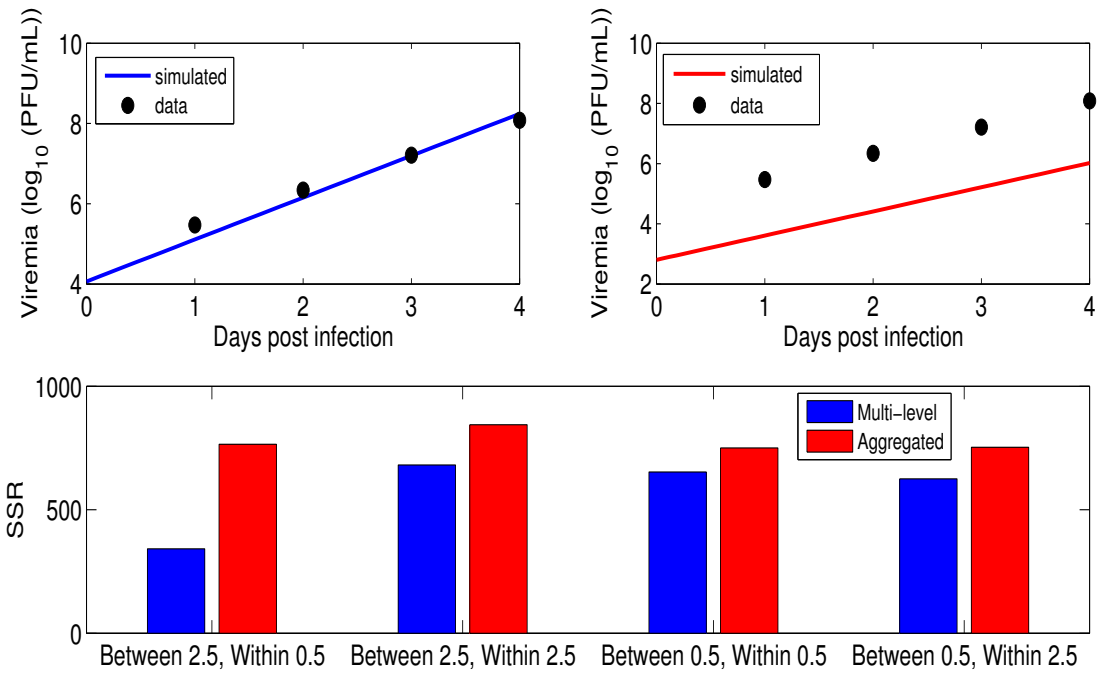

Figure 6.6: Top panel - A plot of the ODE model prediction for all species combined. Top Left panel - multi-level model, Top Right panel - aggregated model. X-axis - days post infection, Y-axis - ODE predicted virus concentration (line) and simulated data (points) in log_{10} PFU/mL. The multi-level model makes better predictions for virus concentration time course with respect to the simulated data. Bottom panel - Performance at predicting virus concentration in simulated data: Multi-level model (blue) vs. aggregated model (red). Shown are SSR (sum of squared residuals) for multi-level model predictions (species level SSR) and aggregated model predictions (individual level SSR) for different between and within-species variances (Table 6.1).

6.3.3 Estimates for ODE parameter a

The sum of squared residuals between predicted and actual mean at the species and genus level for a are shown in Fig. 6.5 (results shown for the case where there is high between-group and low within-group variance in M). Here the aggregated model is able to better predict the means at both the species and genus level than the multi-level model. The results shown here are for the case where there is high

between-group variance and low within-group variance in M. The results for a were similar given other variations in M.

6.3.4 Predictions of time course of virus concentration

The multi-level model is able to make better predictions of virus concentration over time with respect to the simulated data. We generated a new set of simulated data in the following manner. The data generation phase (see Simulated Data) generates 10 different distributions (V_{dose},a,M) at the species level. We take the means of each of these 10 distributions (separately) and create 10 different tuples (V_{dose},a,M). These species level ODE parameters are given to the solver to generate simulated data sampled daily up to 4 days post infection.

We compare the multi-level and aggregated models to this simulated data using 3 methods:

1. Individual level SSR (multi-level): the multi-level model produces estimates (distributions) of (V_{dose},a,M) for each of the 30 individuals. For each species, we take the average of the distributions of (V_{dose},a,M) for the 3 individuals that belong to that species. These ODE parameters are then given as input to the solver that generates a virus concentration over time.

2. Species level SSR (multi-level): for each of the 10 species, the multi-level model produces estimates (distributions) of (V_{dose},a,M). We take the average of each of these 10 distributions (separately) and obtain 10 different tuples (V_{dose},a,M). These ODE parameters are then given as input to the solver that generates a virus concentration over time. We note that only the multi-level model produces a prediction at the species level.

3. Individual level SSR (aggregated): similar to the first method, the aggregated

model produces estimates (distributions) of (V_{dose},a,M) for each of the 30 individuals. For each species, we take the average of the distributions of (V_{dose},a,M) for the 3 individuals that belong to that species. These ODE parameters are then given as input to the solver that generates a virus concentration over time.

The comparisons between the multi-level and aggregated models are shown in Fig. 6.6. The multi-level model produces better predictions of the time course of virus concentration than the aggregated model (Fig. 6.6, Panel B), where the comparison is done using any of the three methods described above. Ultimately this leads to better predictions of time course of virus concentration after infection (Fig. 6.6, Panel A).

6.3.5 ODE parameter correlations

We have observed that parameter correlations help constrain the parameter space and produce narrower bounds on estimates [28]. Both the multiple level hierarchical and the aggregated model showed correlations between parameters at the individual level, e.g. $log_{10}V_{dose}$ and $log_{10}a$ had a statistically significant correlation ($r^2 = 0.44$, p-value = 0, OLS slope = -0.85) in the multi-level model for the case where there is less within-species and more between-species difference. These correlations were absent at the species and genus level in both the models.

6.4 Discussion

6.4.1 Summary of Results

Our analysis shows that the multi-level model makes more accurate predictions at the species and genus levels if there is large variation in ODE parameters at the

species level. We are interested in the species level parameter estimates since the hierarchical Bayesian model pools together information from diverse individuals at that level. The species level gives a more nuanced estimate of how an entire group of individuals behaves in response to infection.

6.4.2 Caveats and Limitations

We have larger variation (both on absolute and relative scales) in species mass (M) than exists in the experimental infection data. The larger variation is chosen in order to demonstrate the conditions under which the multi-level outperforms the aggregated model.

The results presented here change if the between group variation in a is increased. We believe that the dynamical system represented by the ODEs is especially sensitive to a. Such behavior, where some parameters may be more susceptible to perturbations in parameter space than others, is typical of biological systems where one or more parameters are stiff and account for a lot of variation in data [109, 110].

Finally, the analysis presented here is from one run of the hierarchical Bayesian models. Although one run generates large amounts of data, since the Bayesian models are stochastic, multiple independent runs would give more confidence in the generality of the results.

6.4.3 Discussion

The multi-level model makes more accurate estimates of ODE parameters at the species level and genus level when there is more between-species difference than within-species difference in those parameters. For example, consider the case where the ODE parameter M has more variation between species (2.5) than within (0.5).

The multi-level model makes more accurate estimates of M at the species and the genus level (Fig. 6.4).

The multi-level model also more accurately predicts time course of virus concentration with respect to simulated data (Fig. 6.6). The simulated data is generated by taking species level estimates of ODE parameters from the data generation phase and giving them as input to the ODE solvers.

We also observed that if an inferred parameter does not have phylogenetic dependence (say V_{dose}) and is not hierarchically distributed then the aggregated model outperforms the multi-level model in inferring estimates of that parameter (results not shown).

Both the multi-level and aggregated models preserved ODE parameter correlations at the individual level. However these correlations were absent at the population level in the multi-level model. This is of interest since we have observed that parameter correlations help constrain the parameter space and produce narrower bounds on estimates [28]. In the absence of parameter correlations at the species and genus levels, meaningful priors at these levels (such as we have in the multi-level model) may help constrain parameter estimates to narrower and more biologically realistic regimes.

Generally, a multi-level model applied to data with large between species variation makes more accurate predictions than an aggregated model. This appears to be due to the ability of the multi-level model to incorporate realistic priors at the species level and more accurately simulate the hierarchical nature of a multi-species dataset.

Accurate predictions about time course of virus concentration (with respect to simulated data, Fig. 6.6) enables the multi-level model to make better predictions of parameters (Figures 6.4 and 6.5). The ability to make accurate predictions of ODE parameters from data is important. Our analysis suggests that the multi-level model

will outperform an aggregated model on experimental data in which the true values of ODE parameters are unknown.

The next chapter will examine the performance of the multi-level model in the following realistic scenarios: we will have a more complex and biologically realistic ODE model and the model will be trained on actual experimental data. We will focus on a case where ODE parameters have more between-species variation than within-species for all parameters (except V_{dose}). Our objective will be to test model parameters characterizing WNV infection and host immune response for dependence on host (species) body mass.

Chapter 7

A Hierarchical Bayesian Model of Body Size Effects on Pathogen Replication and Immune System Response

7.1 Introduction

Many emerging pathogens infect multiple host species [8], and multi-host pathogens may have very different dynamics in different host species [9]. Diseases that jump the species barrier from animals to humans (zoonotic diseases) cause 2.5 billion cases of human illness and 2.7 million human deaths per year [10]. Many emerging diseases are zoonotic in origin.

Understanding how quickly pathogens replicate and how quickly the immune system responds is important for predicting the epidemic spread of emerging pathogens. Host body size, through its correlation with metabolic rates, is theoretically predicted

to impact pathogen replication rates and immune system response rates [6]. Prior work suggests that body mass affects pathogen replication rates [9, 38, 26], but immune response times are either independent of mass or increase only very slowly as mass increases [26, 57]. Here, I use mathematical models of viral time courses from multiple species of birds infected by WNV to test more thoroughly how disease progression and immune response depend on mass and phylogeny.

Phylogeny is an important determinant of the pathogenesis of WNV. Passerine species sustain more viremia than non-Passerine species [5]. Corvid species are particularly susceptible to WNV infection [5]. Therefore, any analysis of disease dynamics in multi-host pathogens like WNV should take phylogeny into account. We accomplish this using hierarchical Bayesian models that incorporate the hierarchical nature of phylogeny.

The role of phylogeny in determining WNV infection outcome is known qualitatively [5]. We aim to provide a quantitative prediction for viral competency for Passerines and corvids in particular. Further, the fits to experimental data using our mathematical models enable us to form hypotheses as to why WNV viremia is higher in these groups.

Hierarchical Bayesian models enable modelers to encapsulate knowledge about the underlying biology as priors. Suitable priors in a hierarchical Bayesian framework can help reduce variance of parameter estimates [13] and possibly produce more accurate parameter estimates. The previous chapter validated the hierarchical Bayesian models and showed that a model that incorporates the hierarchal nature of phylogeny and encodes this information as priors in a hierarchical Bayesian model, may enable more accurate estimates of parameters characterizing WNV infection. The present chapter extends the models in the previous chapter by applying them to actual experimental data.

We also calculate a reservoir competence index that indicates the relative number of infectious mosquitoes that would be derived from feeding on these hosts.

This chapter extends the work in the previous chapter by applying hierarchical Bayesian models to actual experimental data while using a more biologically realistic ODE model of WNV replication and immune response. The goals of this chapter are:

1. To test if a multi-level model produces more accurate estimates of virus concentration over time (with respect to experimental infection data) than an aggregated model.

2. To test model parameters characterizing WNV infection and host immune response for dependence on host (species) body mass and phylogeny.

7.2 Materials and Methods

7.2.1 Overview of Methods

The multi-level hierarchical Bayesian model mimics the hierarchical nature of phylogeny. There are three levels in the hierarchical tree representation: individual, species and order (Fig. 6.3). Each level of the tree has an equation describing the distribution of differential equation model parameters. The differential equations and hierarchical Bayesian models are explained in greater detail in the next section.

Our goal is to compare two different hierarchical Bayesian models: a multi-level model that has three levels of hierarchy (for individual, species and order) and an aggregated model with two levels of hierarchy (all individuals of all species pooled together under a single top level entity) (Fig. 6.2). Each of these Bayesian models

is run on 3 different kinds of experimental data: all Passerine and non-Passerine species combined, Passerine and non-Passerine species separately and finally only corvid species (a subset of Passerines).

7.2.2 Ordinary Differential Equation Model

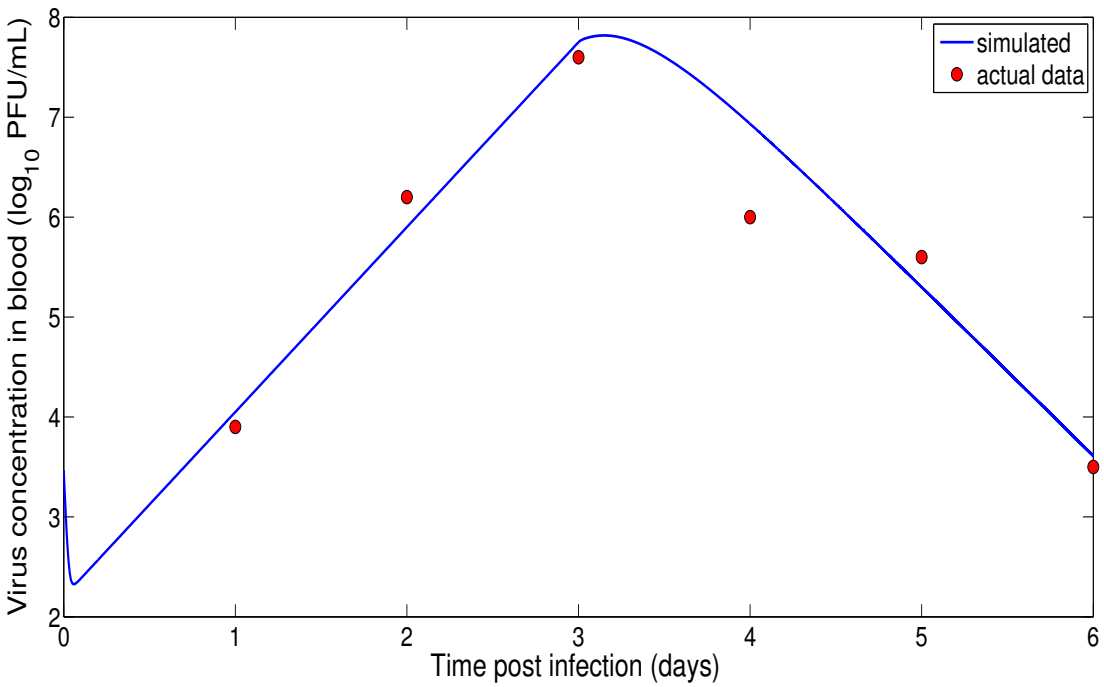

Figure 7.1: A sample ODE prediction for virus concentration (in log_{10} PFU/mL) over time post infection (blue) and experimental data on virus concentration (red). Data show viremia of great-horned owls from [5].

We use two models that simulate viremia in serum. The first model assumes that the infection is target-cell limited in birds, i.e. the concentration of virus reaches a peak and then declines when few susceptible target cells remain. The model is the same as the target-cell limited model for mice (Chapter 5, Eqs. 5.1-5.4). The Bayesian model infers (V_0,β,p,δ) from the viral titer data. The ordinary differential

equations describing our viral kinetic models were solved numerically in Matlab [31]. The Runge-Kutta 4 method of integration was employed. All model parameters and virus concentration are logged (base 10) in order to stabilize variance and ensure positive estimates from the Bayesian inference. A sample plot of the ODE prediction of virus concentration over time (compared to observed data about virus concentration) is shown in Fig. 7.1.

We also use a more sophisticated model that assumes viral decline is due to an adaptive antibody (induced IgM) response (same as the adaptive immune response model in mice, Chapter 5, Eqs. 5.7-5.11). The Bayesian model infers (V_0,β,p,δ,ρ,t_i) from the viral titer data.

7.2.3 Constraints on Model Parameters

The model constraints are summarized in Table 7.2. The initial density of uninfected target cells, $T(0)$, is fixed to 2.3×10^5 /mL (mean of the estimated range in mice, Chapter 5, [28]). The rate of clearance of free infectious virus,γ, is set to 44.4 /day (upper bound of estimate in mice, [28]) for all species except three corvids (Fish crows, Blue jays and American crows) for which we could get good fits with only a lower value (1 /day).

The eclipse phase of virus, $1/k$, is fixed to the lower bound of a range from wild-type mice (6 hours, see Chapter 5, [28]). Similarly, based on calculations in wildtype mice (Chapter 5), the lifetime of productively infected cells, $1/\delta$, is constrained to be greater than 1 hour while obeying the relationship $1/\delta + 1/k = 24$ hours. Finally, the rate of antibody production (η) is fixed at 54.7 /day [28] and the time of initiation of antibody, t_i, is bounded between 2 and 4 days [28] based on experimental data or model fits to experimental data in wildtype mice.

The infectious virion burst size, p/δ, is constrained to not exceed 10^{12} PFU based

on fits of the target cell limited model to birds. Similarly, the efficacy of antibody neutralization, ρ, is bounded between 0.05 and 1000 $\text{PRNT}_{50}^{-1}\text{day}^{-1}$ based on model fits to experimental infection data on birds. The initial viral titer, V_0, is constrained to be within 0.1 and 10^{12} PFU/mL and the rate of production of virus, p, is constrained to lie within 0.5 and 10^{12} /day based on fits in birds.

7.2.4 Experimental data

WNV infects bird species ranging from 3 gm sparrows to a 3 kg geese. This wide range of species mass allows us to test the effects of animal body size on pathogen replication and immune response. We focus on data from a study which experimentally infected animals with the same strain of WNV (WNV NY99-6480). Komar et al [5] experimentally infected 25 species of birds with WNV NY99-6480 and took daily measurements of the concentration of infective virions in blood (viremia) over the course of infection (sample plot shown in Fig. 1, data points in red). Viremia was reported in Plaque Forming Units (PFU).

From this experimental dataset we excluded data on 2 species (Japanese quail and ring-necked pheasant). The virus kinetics in Japanese quail were erratic and viremia levels in the ring-necked pheasant were approximately constant over time; as such these species could not be simulated by our model.

The Passerine species are the common grackle, American robin, red-winged blackbird, house finch house sparrow and corvids. The corvid species are fish crows, blue jays, American crows and black-billed magpies.

The experimentalists also reported the Level of Detection (LOD) of their viral assay as $10^{1.7}$ PFU. The raw experimental data had reports of consecutive viral measurements at LOD in the declining phase of viremia for some species. In these cases we only considered the first occurrence of LOD in the time series and discarded

the remaining. Considering all LOD data points would have led our models to an underestimate of the slope of the declining phase due to the flat trajectory induced by multiple consecutive viremia measurements at the same level.

7.2.5 Hierarchical Bayesian Model

Aggregated model

Given a population of individuals that belong to the same group, the hierarchical Bayesian model assumes that the dynamics of infection of each individual is characterized by parameters (θ_i to θ_n for n individuals) that are drawn from a common species-level distribution (μ).

The aggregated model has 23 species. The species are aggregated to form a tree of height 2. The model is shown graphically in Fig. 6.2 (Left panel). There are two levels in the hierarchical tree representation: individual and all individuals (of all species) combined. Each level of the tree has an equation describing the distribution of ODE model parameters (Eq. 5.1-5.4 and Eq. 5.7-5.11). The ith individual has a parameter θ_i that represents the mean of (V_{dose},a,M) for a particular individual. This parameter θ_i is then drawn from a higher distribution (all species aggregated) with mean μ. The details of the model are given in the Appendix A.

Multi-level hierarchical model

We also devised a multi-level hierarchical model that has 23 groups (species). The groups are arranged hierarchically to form a tree of height 3. The model is shown graphically in Fig. 6.3 (Left panel). There are three levels in the hierarchical tree representation: individual, species and order (Fig. 6.3). Each level of the tree has an equation describing the distribution of ODE model parameters (Eq. 5.1-5.4 and

Eq. 5.7-5.11). The ith individual has a parameter θ_i that represents the mean of (V_{dose},a,M) for a particular individual. This parameter θ_i is then drawn from a species-level distribution with mean μ. Finally, the species-level estimate is itself drawn from a order-level distribution centered around η. The details of the model are given in the Appendix B.

MCMC implementation

The details of the MCMC implementation are described in Chapter 6. All models were run for 10,000 iterations. This constitutes a single "run" of the Bayesian model. The initial 1000 iterations were discarded (burn-in phase). Of the remaining 9,000 samples we retained every fifth sample.

Calculation of averages for ODE parameters at different levels of hierarchy

We use the posterior samples of ODE parameters to generate the averages in the following way: for each individual, species or order we have 10,000 samples originally (as described in the previous section) at that level of the hierarchy. After burn-in this is reduced to 9000 samples and thinning of the samples leads to a total of 1800 samples. The average of these samples (henceforth referred to as individual-level, species-level or genus-level averages) for each ODE parameter (V_0, β, p, δ) is used in the Results section.

Calculation of reservoir competencies

We calculate a reservoir competence index that indicates the relative number of infectious mosquitoes that would be derived from feeding on each host species and is calculated from the viremia that develops in the hosts after infection. We ex-

tend a competence index developed by Komar et al [5] to account for time-varying viremia. Species that sustain WNV viremia above 10^5 PFU/mL are considered infectious for mosquito vectors [5]. The reservoir competence index (C_i) is a function of susceptibility (s), the proportion of birds that become infected as a result of daily exposure; mean daily infectiousness (i), the proportion of exposed mosquito vectors that become infected per day; and the duration of infectious viremia above a threshold (d) [5]. Komar et al [5] calculate the competence as $C_i = s \times i \times d$ where $i = \frac{log_{10}(V_p)-5}{10} + 0.02$ and V_p is the peak viremia attained by a host; this assumes that hosts sustain a fixed viremia (at the level of peak viremia) throughout the duration of infectivity.

Our competency index for each species is calculated as follows:

$$C_i = s \times \int_0^{t_d} i(t)\mathrm{d}t \tag{7.1}$$

$$i(t) = \begin{cases} \frac{log_{10}V(t)-5}{10} + 0.02 & , \quad log_{10}V(t) \geq 5 \\ 0 & , \quad log_{10}V(t) < 5 \end{cases} \tag{7.2}$$

where t_d is the time until viremia is measured experimentally, $i(t)$ is the infectivity at time t and $V(t)$ is the ODE model predicted viremia at time t. Following bird mortality calculations made in Komar et al [5], we set the susceptibility (s) to be 0.7 for Budgerigars and 1 for all other species.

7.3 Results

7.3.1 Accuracy in viremia prediction

We estimated accuracy of viremia prediction by calculating three different estimates of a sum of squared residuals (SSR) between data and ODE prediction (for both the multi-level and aggregated Bayesian models):

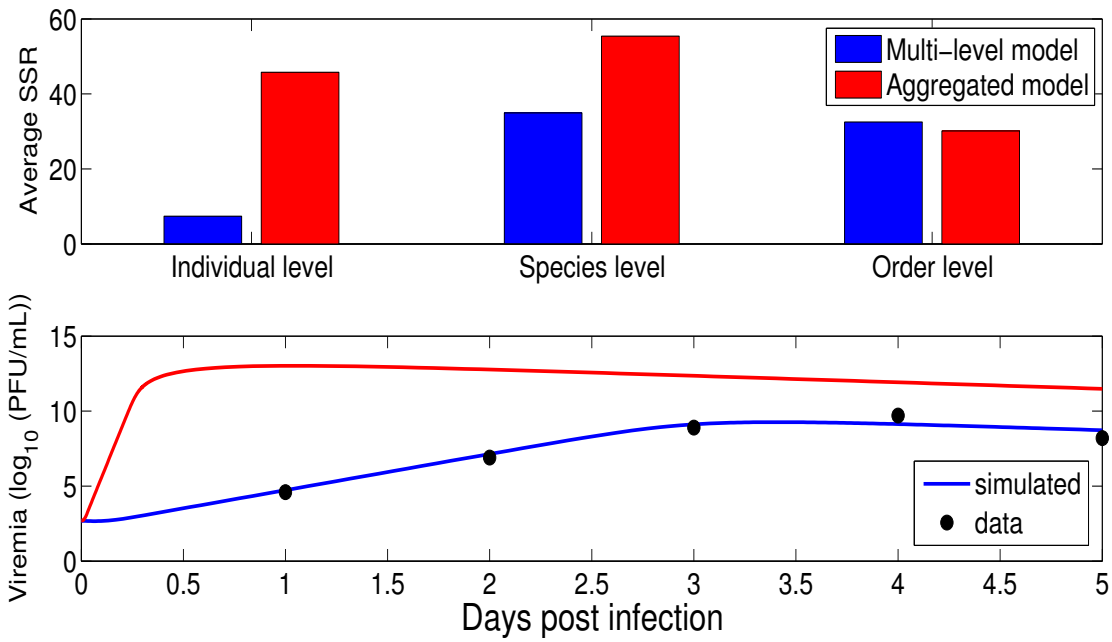

Figure 7.2: Top panel: Accuracy in viremia prediction between multi-level model (blue) and aggregated model (red) for three different levels - individual, species and order. SSR - sum of squared residuals between model predicted viremia and data. Bottom panel: A sample viremia prediction from the multi-level (blue) and aggregated model (red).

1. Individual-level SSR. We calculated individual-level averages of ODE parameters for each species as described in Section 7.2.5. For each individual, we used these individual-level ODE estimates to generate a SSR between data and model prediction in the following way: for each individual in a species, we gave the ODE solver the individual-level parameter estimates and calculated the SSR between model prediction and individual-level data. The SSR was then summed up for all individuals of all species and then divided by the number of individuals. We call this the individual-level SSR.

2. Species-level SSR. We calculated species-level averages of ODE parameters for each species as described in Section 7.2.5. For each species, we used these

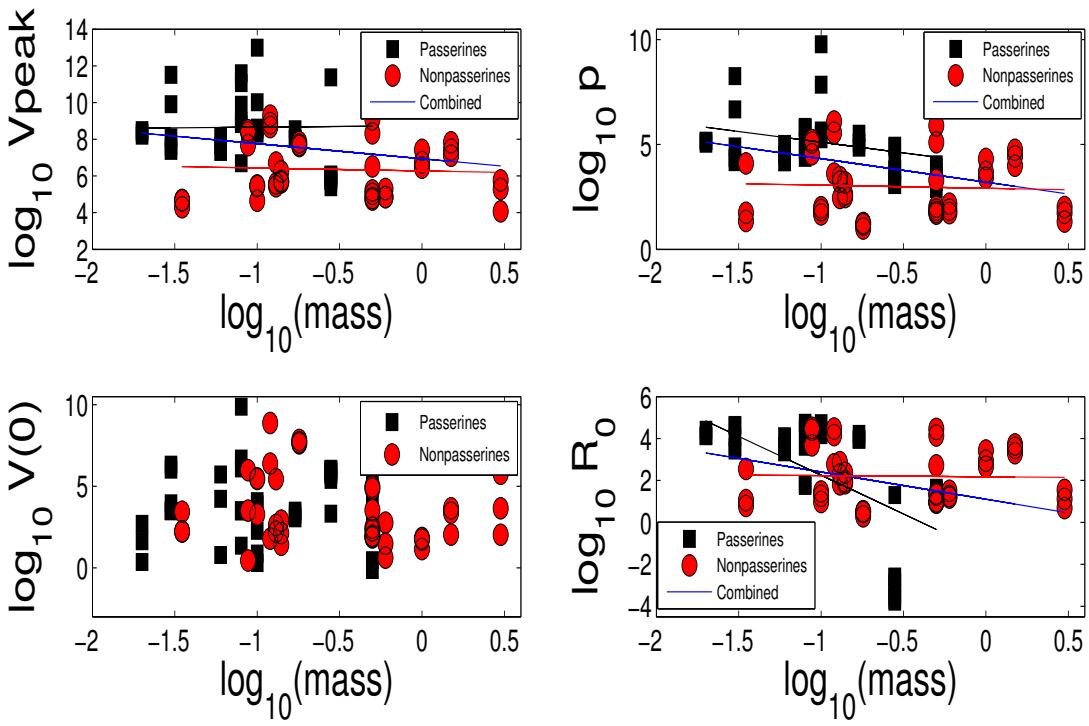

Figure 7.3: Scaling of biologically relevant quantities with host mass for the multi-level model: Passerines (black square and black regression line, non-Passerines (red circle and red regression line) and all combined (blue regression line). Top left: Peak viremia (V_p), slope = -0.82, p-value = 0.06, r^2 = 0.04. Top right: WNV production rate (p), slope = -1.1, p-value = 0.002, r^2 = 0.11. Bottom left: Inoculated density of virions (V_0), p-value = 0.35. Bottom right: R_0, slope = -1.3, p-value = 0.006, r^2 = 0.09.

species-level ODE estimates to generate a SSR between data and model prediction in the following way: for each individual in a species, we gave the ODE solver the species-level parameter estimates and calculated the SSR between model prediction and individual-level data. The SSR was then summed up for all individuals within a species and then for all species and then divided by the number of individuals. We call this the species-level SSR.

3. Order-level SSR. We calculated order-level averages of ODE parameters for

Table 7.1: Statistics of scaling relationships with species mass (all species combined) from multi-level model with target cell limitation (TCL) or adaptive immune response (AIR)

Parameters	Combined slope	p-value	r^2
p (TCL): WNV production rate	-1.1	0.002	0.11
p (AIR): WNV production rate	-0.84	0.04	0.05
R_0 (TCL): Basic reproductive number	-1.3	0.006	0.09
R_0 (AIR): Basic reproductive number	-0.57	0.08	0.04
p/δ (TCL): Burst size	-1.1	0.001	0.12
p/δ (AIR): Burst size	-0.86	0.03	0.06
V_p (TCL): Peak viremia	-0.82	0.06	0.04
V_p (AIR): Peak viremia	-	0.54	0.005
V_0 (TCL): Inoculated WNV density	-	0.35	0.1
V_0 (AIR): Inoculated WNV density	-	0.1	0.03
β (TCL): WNV infectivity	-	0.64	0.003
β (AIR): WNV infectivity	-	0.39	0.009
δ (TCL): Death rate of productively infected cells	-	0.6	0.003
δ (AIR): Death rate of productively infected cells	-	0.51	0.005
ρ (AIR): Rate of adaptive immune system mediated virus neutralization	-	0.11	0.03
t_i (AIR): Time of initiation of IgM response	-	0.56	0.004

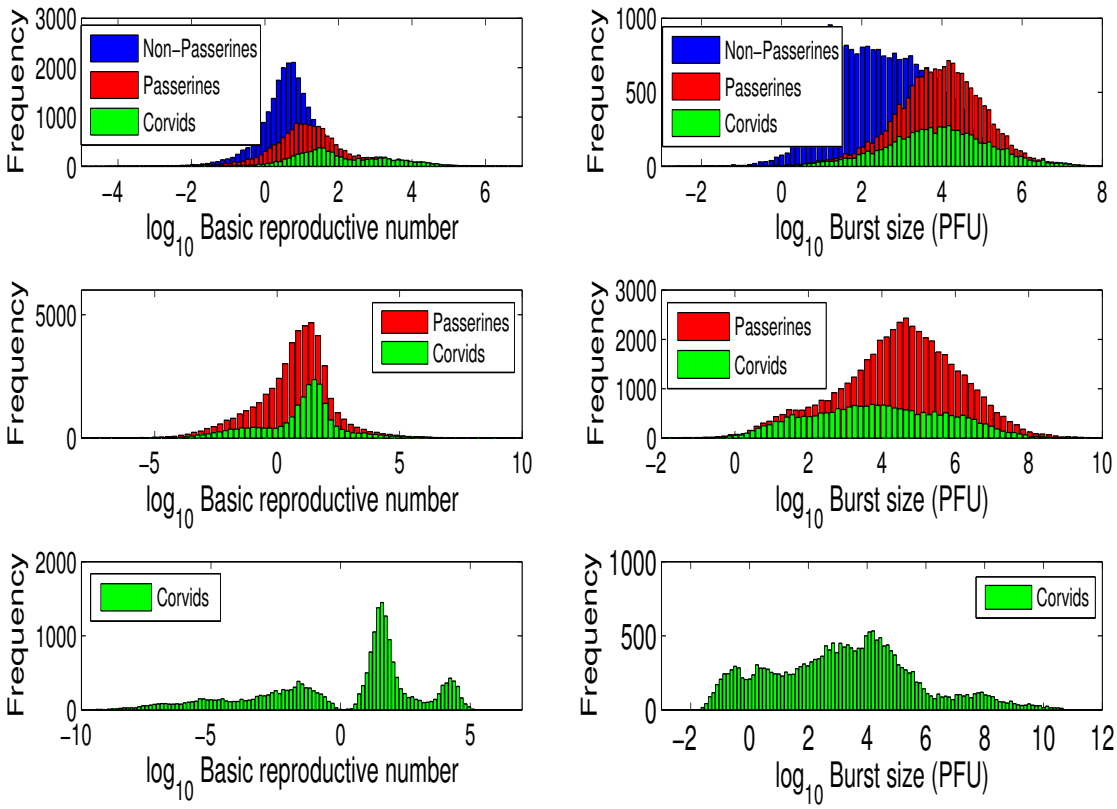

Figure 7.4: Posterior distribution of $log_{10}\ R_0$ and burst size ($log_{10}\ p/\delta$) for the multi-level model (target cell limited model). Top panel: Multi-level model with all Passerines (red), corvids (green) and non-Passerines (blue). Middle panel: Multi-level model with only Passerines (red) and corvids (green). Bottom panel: Multi-level model with only corvids (green).

each species as described in Section 7.2.5. For each individual, we used these order-level ODE estimates to generate a SSR between data and model prediction in the following way: for each individual in a species, we gave the ODE solver the genus-level parameter estimates and calculated the SSR between model prediction and individual-level data. The SSR was then summed up for all individuals of all species and then divided by the number of individuals. We call this the genus-level SSR.

We observed that the multi-level model produced more accurate estimates at the individual-level and species-level (Fig. 7.2, top panel). A representative viremia prediction for both the multi-level and aggregated model is also shown (Fig. 7.2, bottom panel). The performance of both the models at the order-level were similar.

7.3.2 Scaling of biologically relevant quantities

We looked at the correlation between individual-level averages of ODE parameters and species mass (Fig. 7.3) for the multi-level model. The scaling relationships and statistics are summarized in Table 7.1. We observed that the production rate of infective virions (p, PFU /day) is correlated with species mass (all species combined: p-value = 0.002, r^2 = 0.11, slope = -1.1; only Passerines: p-value = 0.04, r^2 = 0.1, slope = -1).

The basic reproductive number, R_0, had a significant overall correlation with mass (all species combined: p-value = 0.006, r^2 = 0.09, slope = -1.3; only Passerines: p-value = 7×10^{-5}, r^2 = 0.33, slope = -3.7). Peak viremia (P_v, the maximum viremia attained by an individual over the time course of infection) had a marginally significant correlation with species mass (all species combined: p-value = 0.06, r^2 = 0.04, slope = -0.82).

The burst size (p/δ, PFU) had a significant relationship with species body mass (all species combined: p-value = 0.001, r^2 = 0.12, slope = -1.1; only Passerines: p-value = 0.03, r^2 = 0.12, slope = -1.1). Also the viremia at day 1 ($V(1)$) was correlated with mass (all species combined, p-value = 0.003, r^2 = 0.1, slope = -1.1).

The density of inoculated virions (V_0) and the infectivity of WNV (β) had no significant relationship with species mass (all species combined: p-value = 0.35, r^2 = 0.1 and p-value = 0.64, r^2 = 0.003, respectively). Finally, the death rate of productively infected cells (δ, /day) had no relationship with mass (all species

combined, p-value = 0.6).

We also used the adaptive immune response model (Eqs. 6.5-6.9) to investigate how parameters related to the immune response scale with host body mass (multi-level model, Fig. 7.6 and Table 7.1). The rate of adaptive immune system mediated neutralization of virus (ρ, $\text{PRNT}_{50}^{-1}\text{day}^{-1}$) did not have a significant relationship with body mass (all species combined: p-value = 0.11, r^2 = 0.03, slope = -0.19), although we observed that in Passerines it declined significantly with mass (p-value = 0.04, r^2 = 0.1, slope = -0.51). The time of initiation of IgM response (t_i) also did not have a significant relationship with species mass (all species combined: slope = 0.002, p-value = 0.56, r^2 = 0.004; only Passerines: slope = 0.01, p-value = 0.07, r^2 = 0.08).

7.3.3 Effect of phylogeny on parameter estimates

We investigated the effect of phylogeny on two biologically relevant quantities - the basic reproductive number (R_0) and the burst size. The basic reproductive number represents the average number of second generation infections produced by a single infected cell placed in a population of susceptible cells. If R_0 is greater than 1, then an infection can be established, whereas an infection rapidly dies out if R_0 is less than 1. For the target cell limited model (Eqs. 5.1-5.4), R_0 is given by [99]:

$$R_0 = \frac{p\beta T_0}{\delta(\gamma + \beta \cdot T_0)} \tag{7.3}$$

The burst size, p/δ, represents the number of infectious virions released by an infected cell over its productively infected lifespan. Estimates of the mean values of R_0 from the multi-level model are higher for Passerine species (23.8) compared to non-Passerines (4.7) (Fig. 7.4, top panel). Within Passerines, corvid species (fish

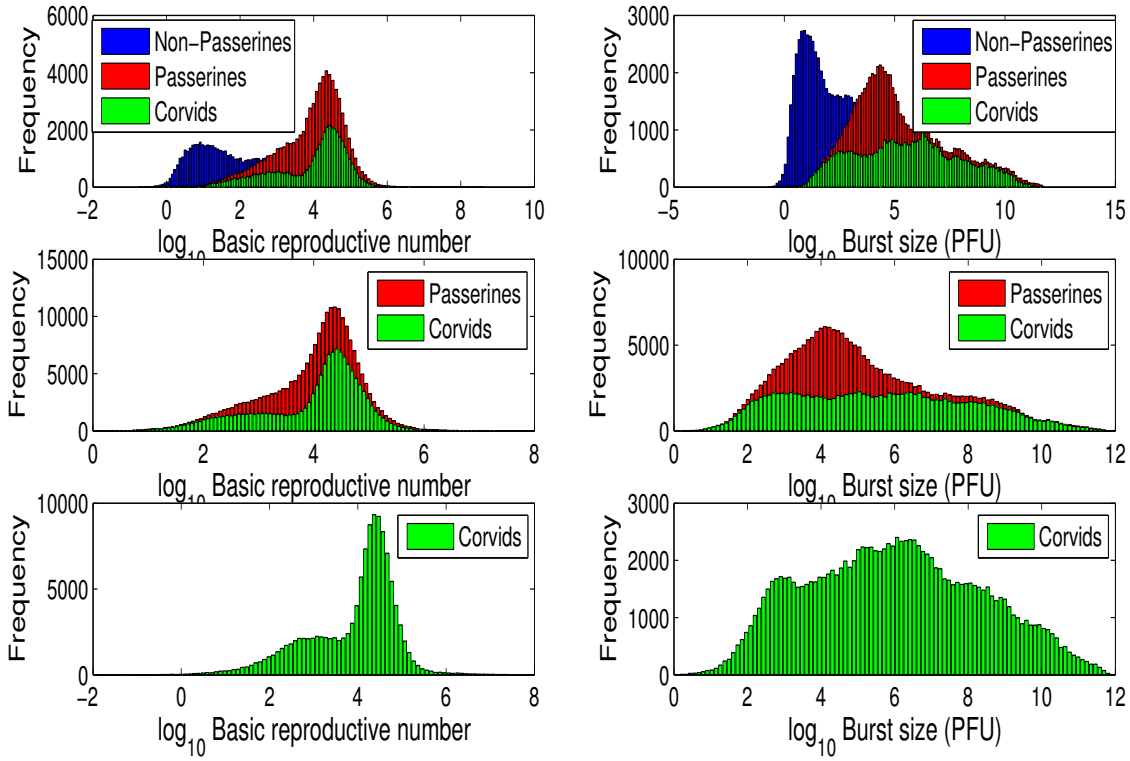

Figure 7.5: Posterior distribution of log_{10} R_0 and burst size (log_{10} p/δ) for the aggregated model (target cell limited model). Top panel: Aggregated model with all Passerines (red), corvids (green) and non-Passerines (blue). Middle panel: Aggregated model with only Passerines (red) and corvids (green). Bottom panel: Aggregated model with only corvids (green).

crows, blue jays, American crows and black-billed magpies) have the highest value of R_0 (93.2) (Fig. 7.4, top panel). Finally, estimates of R_0 in the aggregated model (Fig. 7.5) are orders of magnitude higher than in the multi-level model (Fig. 7.4).

7.3.4 Estimates of reservoir competence

We calculated a reservoir competence index that indicates the relative number of infectious mosquitoes that would be derived from feeding on these hosts (Section

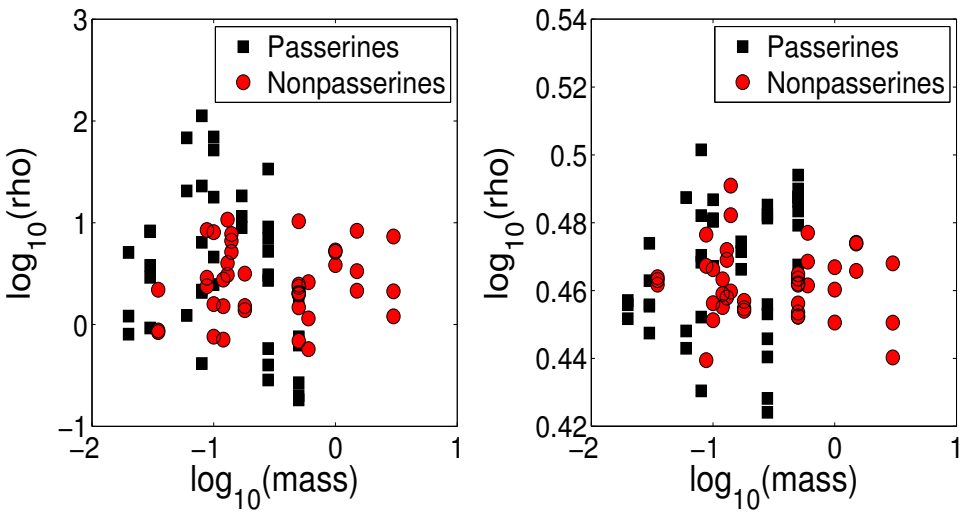

Figure 7.6: Scaling of immune response parameters with host mass for the multi-level model with immune response: Passerines (black square) and non-Passerines (red circle). Left panel: Rate of adaptive immune system mediated virus neutralization (ρ, $\text{PRNT}_{50}^{-1}\text{day}^{-1}$). Right panel: Time of initiation of IgM response (t_i, days) (combined and each group separately are non-significant).

7.2.5). The reservoir competency indices we calculate are correlated with and approximately half of the estimates in Komar et al [5] (Fig. 7.7, $r^2 = 0.94$, slope $= 0.54$, p-value $= 0$).

7.4 Discussion

7.4.1 Summary of Results

A multi-level hierarchical model informed by phylogeny more closely matches empirical viremia than an aggregated model (Fig. 7.2). The multi-level model also produces more reasonable estimates of biologically relevant quantities like the basic reproductive number and burst size (Fig. 7.4 and 7.5). The multi-level model pre-

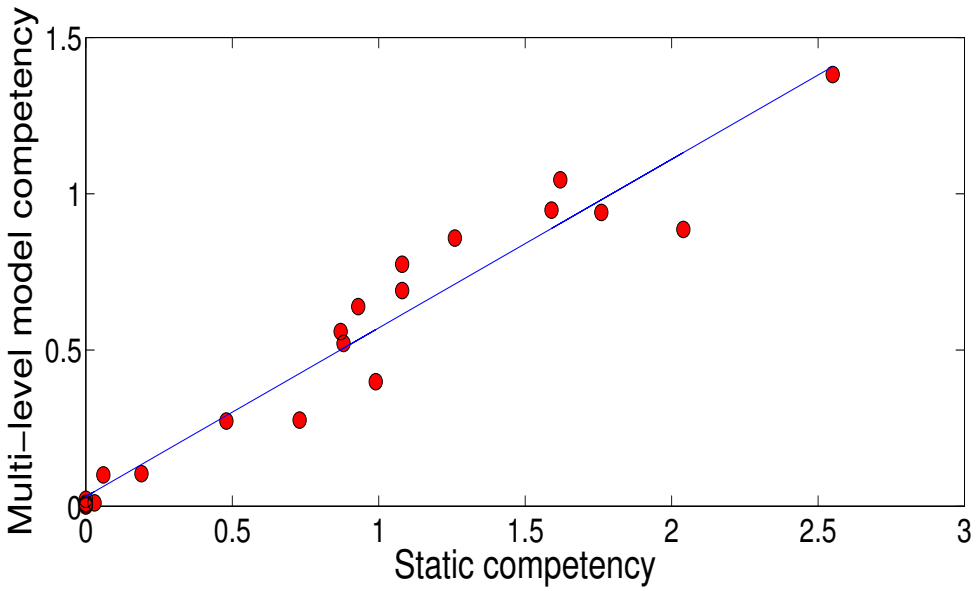

Figure 7.7: Correlation between multi-level model predicted competency and competency from Komar et al [5] assuming static viremia ($r^2 = 0.94$, slope $= 0.54$, p-value $= 0$)

dicted WNV production rate decreases with species mass, consistent with theoretical predictions from metabolic scaling theory (Fig. 7.3).

7.4.2 Discussion

Hierarchical Bayesian models are a principled method to aggregate data from multiple related individuals while still doing fits to data at the individual level. Here we use a multi-level hierarchical model to incorporate phylogeny and pool infection data from related species. We observe that the multi-level model produces more accurate predictions of viremia at the individual and species level when compared to hierarchical models that have fewer levels of hierarchy (Fig. 7.2).

Additionally, multi-level models with Passerines and non-Passerines or just

Passerines (Fig. 7.4, top and middle panels) produced more realistic and well peaked distributions of R_0 and burst size, than a multi-level model with only corvids (Fig. 7.4, bottom panel) and the aggregated model (Fig. 7.5). This appears to be due to the ability of multi-level models to pool information at the species level from disparate individuals both within and between different species.

The mean values of R_0 from the multi-level model are higher for Passerine species (23.8) compared to non-Passerines (4.7) (Fig. 7.4, top panel). Within Passerines, corvid species have the highest value of R_0 (mean 93.2). Burst sizes of Passerine species (8690 PFU) are much higher than those in non-Passerines (340 PFU) (Fig. 7.4, top panel). This appears to be consistent with experimental studies that found Passerines and corvids have higher reservoir competency (ability to transmit infection to mosquitoes) than non-Passerines [5]. Overall, phylogeny emerges as a key determinant of biologically relevant quantities like the basic reproductive number and burst size.

The mean values of R_0 from the multi-level model for Passerine species (23.8) is also higher than the corresponding model predicted value in mice (mean $R_0 = 2.5$, Chapter 5). The infectious virion burst size of Passerine species (8690 PFU) is also significantly higher than model estimates from fitting data in mice (mean infectious virion burst size = 3 PFU, Chapter 5).

Individual cellular metabolic rates and times, if constrained by host metabolism, are expected to scale with host body mass as $M^{-1/4}$ and $M^{1/4}$, respectively. We observe that the production rate of infectious virions (p, /day) declined significantly with host body mass. There is large scatter but the 95% confidence interval (CI) for the slope ([-1.5 0.03]) includes the theoretically predicted exponent of -0.25 (Fig. 7.3). However, the death rate of productively infected cells (δ, /day), also theoretically predicted to increases with mass, had no relationship with species mass. Lastly, the basic reproductive number (R_0), declined significantly with body mass (Fig. 7.3)

and the relationship is even more significant within Passerine species. This is most likely due to the fact that the production rate of virions (p), a component of the R_0 (Eq. 7.3), declined with mass.

We found that the mean of peak viral concentration in serum (peak viremia) declines with species body mass (Fig. 7.3) although the correlation was marginally significant. Additionally, most Passerine species had higher peak viremia than non-Passerines. This is likely due to the fact that most of the Passerine species had a higher value of production rate (p) than the non-Passerines. Overall, we observed scaling of some biologically significant parameters with mass which were modified from theoretical scaling predictions by the influence of phylogeny.

The density of inoculated virions (V_0) has no significant relationship with species mass (Fig. 7.3). This is surprising since if mosquitoes inoculated a fixed dose directly into the host bloodstream, the density of virions (V_0) would be expected to decline with host mass since the dilution would be higher in the larger blood volume of a larger species. Mosquito inoculated WNV, that is initially localized at the site of infection [34], is taken up by immune cells to nearby lymph nodes and thereby traffics to different organs via the bloodstream. Our results point to the importance of accounting for spatial patterns of viral spread, especially in the initial stages of an infection when virus is localized. However for computational efficiency we use differential equation models that ignore space and assume that all components are well mixed.

We calculated a reservoir competence index that indicates the relative number of infectious mosquitoes that would be derived from feeding on these hosts (Section 7.2.5). Our reservoir competency index is a refinement on previously published indices [5] since they take time-varying viremia and species relatedness (via the multi-level Bayesian model) into account. The reservoir competency indices we calculate are correlated with and approximately half of the estimates in Komar et al [5] (Fig.

7.7). The mean reservoir competence for Passerine species (0.8) is higher than that of non-Passerines (0.2).

We used the adaptive immune response model (Eqs. 5.7-5.11) to investigate how parameters related to the immune response scale with host body mass (multi-level model, Fig. 7.6). The rate at which the adaptive (antibody) immune response neutralizes virus (ρ) did not have a significant relationship with body mass, although we observed that in Passerine species it declined significantly with mass. The time of initiation of the adaptive (antibody) immune response (t_i) also did not have a significant relationship with species mass.

The target-cell limited and adaptive immune response models both produce similar scaling predictions (when coupled to the multi-level hierarchical model) (Table 7.1), e.g. both viral dynamics models predict that the production rate of WNV (p) declines with species mass.

In summary, we investigated the effect of body size in the immune system which is a complex, non-linear dynamical system. Previous scaling work has focussed on easily observable attributes such as lifespan or fertility rate [11, 12]. In contrast, in-vivo viral production rates and immune response rates must be inferred by fitting mathematical models to empirical data such as the viremia curves we use here.

Here we use a multi-level model hierarchical Bayesian model to infer parameters such as viral production rate for multiple species. This leads to new hypotheses about the mechanisms that cause certain taxonomic groups to have higher viremia. For example, our models suggest that higher burst sizes cause corvids to harbor higher WNV viremia (Fig. 7.4).

Our modeling also suggests that rates of WNV production decline with species mass whereas rates and times related to the adaptive immune response do not vary systematically with mass. Taken together, these results provide an understanding of

how epidemiological determinants like peak viremia vary with species body mass.

Peak viremia is an important epidemiological determinant for the spread of WNV [5]. Above a threshold peak viremia of 10^5 PFU/mL of blood, a host is capable of infecting an uninfected mosquito, and maintain WNV in an enzootic cycle [5]. Hence hosts that can sustain peak viremia above this threshold and for a longer duration are pathogen reservoirs. The dependence of peak viremia on host mass and phylogeny may give important insights into the role of mass and phylogeny on the spread of WNV. For example, larger non-Passerine species, predicted to have lower peak viremia, may be less competent as pathogen reservoirs.

Our viral dynamics models take complex non-linear interactions at the level of the immune system of individuals into account. The hierarchical Bayesian models then aggregate these dynamics across multiple disparate individuals and make predictions at different phylogenetic levels. The methods and approaches developed here are likely to be applicable to modeling of other multi-host pathogens that have significant differences in dynamics between species. These techniques may also be broadly applicable to modeling of other complex systems with non-linear interactions at different levels of organization.

Table 7.2: Parameter constraints of target cell limited and adaptive immune response model in birds

Parameters	Description	Estimated Ranges	Source
γ	WNV clearance rate	44.4/day for non-corvids and 1/day for corvids	Value for non-corvids estimated from fit to viral decay study in wildtype mice [4] (Chapter 5)
η	Rate of IgM production	54.7/day	Fit to antibody titer study in wildtype mice [73] (Chapter 5)
T_0	Initial target cell density	2.3×10^5 /mL	Average of estimated range in mice from [89] (Chapter 5)
k	Rate of transition from I_1 to I_2	4/day	Upper bound of estimate in mice from [90, 91] (Chapter 5)
$1/\delta$	Lifetime of productively infected cells	$\leq 24 - 1/k$ days	Calculations in mice (Chapter 5)
t_i	Time of initiation of IgM response (days post infection)	2 - 4 days	Estimates in mice [73] (Chapter 5)
V_0	Initial viral titer	0.1 - 10^{12} PFU/mL	Model constraint in birds
p	Rate of WNV production	0.5 - 10^{12} /day	Model constraint in birds
p/δ	Infectious virion burst size	$\leq 10^{12}$ PFU	Model constraint in birds
ρ	Efficacy of antibody neutralization	0.05 - 1000 $\text{PRNT}_{50}^{-1}\text{day}^{-1}$	Model constraint in birds

Chapter 8

Conclusions

How different is the immune system of a mouse from that of a human? Do pathogens replicate at the same rate in all species? Diseases that jump the species barrier from animals to humans affect millions worldwide. An understanding of how disease progression and immune response vary from species to species could have important public health consequences. This thesis attempts to understand how immune function scales with body size and is a foundation for future work to investigate scaling of immune response to other pathogens or in other animals. A theory of scaling for the immune system could also have implications for performance scaling in human-engineered systems that draw inspiration from the immune system.

This dissertation analyzed how species body mass and phylogeny affect the arms race between pathogens and the host immune system in the specific case of WNV. In Chapter 3, we showed immune response rates and times are nearly invariant with body mass and how the physical architecture of the immune system facilitates this. In Chapter 4, we showed how chemical signals in the immune system facilitate efficient search for infected cells. Chapter 5 showed that we can predict biologically relevant quantities characterizing WNV infection with precision despite uncertainty

in individual model parameters. In Chapter 6, we showed that using a hierarchical Bayesian model to reflect phylogenetic relationships can help make more accurate estimates of model parameters.

Finally, in Chapter 7, we applied our hierarchical model to empirical data and observed variation of biologically relevant quantities with species mass and phylogeny. The rate at which WNV is produced by infected cells declines with species mass. Since times scale inversely as rates, this is consistent with findings in Cable et al [9] who observed that time to death in WNV infections increased with species mass. Overall, we observed scaling of some biological significant parameters with mass which were modified from theoretical scaling predictions by the influence of phylogeny. Taken together, species mass and phylogeny provide mechanistic insights into why some species (for example, smaller Passerines) are pathogen reservoirs.

8.1 Implications for spread of zoonotic diseases

A critical level of viremia in blood is necessary for a host to infect to uninfected mosquitoes which can then sustain WNV in an enzootic cycle by potentially infecting other susceptible hosts. Some small Passerine species are presumed to be pathogen reservoirs.

Our analysis suggests an important role for both species mass and phylogeny in dictating epidemiological determinants like basic reproductive number, WNV production rate, peak viremia in blood and host competency to infect mosquitoes. Our model is based on a principled analysis and gives a quantitative prediction for key epidemiological determinants and how they vary with species mass and phylogeny. The WNV production rate (p) and the basic reproductive number (R_0) decline with host body mass (Fig. 7.3). The relationship is even more significant within Passerine species (Fig. 7.3).

Our models lend mechanistic insight into why some species (smaller Passerine species) are pathogen reservoirs and some (larger non-Passerine species) are potentially dead-end hosts for WNV. Our techniques give insights into the role of mass and phylogeny in the spread of WNV and potentially other zoonotic diseases.

8.2 How the immune system achieves scale-invariance

In sharp contrast to the vast majority of biological rates that slow systematically as body size increases [11, 12], the rate at which the adaptive (antibody) immune response clears WNV and the time at which it is initiated do not vary systematically with mass (Fig. 7.6). We suggest two plausible mechanisms for this scale-invariant search and response:-

1. The physical architecture of the immune system. In Chapter 3, we proposed that a sub-modular architecture of lymph nodes, that balances local pathogen detection and global antibody production, may lead to nearly scale-invariant search and response times. Reducing time taken to traffic pathogens from tissue to lymph nodes requires numerous small lymph nodes. However a larger lymph node can recruit more immune system cells and speed up response against the pathogen. The optimal architecture that balances the opposing demands of local pathogen detection and global response is one in which lymph node number and sizes both increase with animal size.

2. Signaling in the immune system. Chemical signals released from infected sites help guide immune system cells towards infected regions. Chapter 4 showed that these inflammatory signals lead to efficient search in the immune system and the speedup in search due to these signals is higher in larger animals.

Our model (Chapter 3) predicted time to initiate the adaptive antibody response (t_i) is a combination of: the time to detect WNV by dendritic cells (t^{DC}_{detect}), the time taken by antigen-loaded dendritic cells to migrate to the draining lymph node ($t^{DC}_{migrate}$), the time taken by dendritic cells to present antigen to the antigen-specific cognate T-cells ($t^{DC,cTcell}_{detect}$) and the time taken by the immune system to recruit a critical number of B-cells and then secrete a critical amount of antibody into blood ($t_{recruit}$). We suggest that the architecture of the immune system has evolved to minimize t_i. Minimizing $t^{DC}_{migrate}$ requires having more lymph nodes of smaller sizes since each lymph node would have a smaller draining region over which dendritic cells migrate. Minimizing $t^{recruit}$ requires having fewer but larger lymph nodes since a larger lymph node can recruit more immune system cells. The architecture that balances the opposing demands of local trafficking and global recruitment of immune system cells is one in which the number of lymph nodes and their sizes both increase with animal body size. Our modelling suggests that this would lead to nearly scale-invariant search and response: $t_i \propto M^{1/7}$, where M is the mass of the animal.

8.3 Implications for human-engineered distributed systems

The immune system can be viewed as a computational system that implements a remarkably efficient distributed search for pathogens. Our work suggests that immune responses are nearly as fast in small and large systems. Understanding how the immune system scales up efficiently is important in the design of human engineered systems that are inspired by the immune system. Many distributed systems are engineered to solve analogous problems, and the immune system demonstrates how such engineered systems can achieve desirable scalability. We propose that the physical architecture of the immune system can be emulated to design more efficient

human-engineered distributed systems [54, 26].

The immune system balances the opposing demands of local communication (pathogen detection) and global communication (antibody production). We showed that similar tradeoffs can exist in distributed systems like immune system inspired multi-robot systems and peer-to-peer systems [54, 26]. Taking inspiration from the architecture of the immune system, we proposed a modular RADAR (Robust Adaptive Decentralized search with Automated Response) strategy for distributed systems. We demonstrated how two existing distributed systems (a multi-robot control application and a peer-to-peer system) can be improved by a modular RADAR strategy. Such a sub-modular architecture is shown to balance the tradeoffs between local communication (within peer-to-peer clusters) and global communication (between peer-to-peer clusters), leading to efficient search for rare amounts of information.

Finally, our immune-inspired modular RADAR strategies can be extended to other distributed systems like intrusion detection systems and cellphone networks. Testing the modular RADAR strategy on an implemented mobile multi-robot system to verify our predictions could also be the subject of future investigations.

8.4 Modeling framework for studying multi-host pathogens

This thesis introduced a technique to infer parameters characterizing viral production and immune response across multiple species. The technique involves using hierarchical Bayesian models to encapsulate differences between species as priors. Suitable priors in a hierarchical Bayesian framework can help reduce variance of parameter estimates [13] and possibly produce more accurate parameter estimates, as shown in Chapter 6. To the best of our knowledge, Bayesian non-linear mixed effects models

with multiple levels of hierarchy have not been previously applied to within-host modeling.

Mathematical models that combine within-host experimental data from multiple species, such as the ones presented here, may be useful in studying other zoonotic diseases and help increase our understanding of these diseases. Hierarchical Bayesian models coupled to within-host viral dynamics models can be used to model other zoonotic diseases and multi-host pathogens. Our analysis also suggests that this approach will likely produce more accurate parameter estimates when there is more variation between species than within.

8.5 Implications for translational research

Most immunological experiments are conducted in mice. However immunological results in mice do not translate reliably to humans. There are significant differences in immunology and cell biology between these two species that hamper translational studies and vaccine trials. A theory that describes systematic differences in immune response as a function of mass and phylogeny could have implications for the translation of results of experimental animal studies to increase impact on human health.

Our work is the first to systematically study how the response of the immune system and the pathogen varies from species to species. We separated the inter-species differences into two categories: differences due to species body size and differences due to phylogeny. The differences attributable to phylogeny would subsume differences in immune system cell types, cell biology, activation pathways in immune system cells and types of normal cells susceptible to WNV infection.

Our models are a deliberate simplification of a very complex biological reality. These models reveal broad-scale patterns in pathogenesis and immune response :

1. Rates of WNV production decline with species body mass consistent with predictions from metabolic scaling theory [11, 12] (Fig. 7.3). These predictions are modified by differences in phylogeny, e.g. most Passerine species have a higher host competencies to infect mosquitoes.

2. Rates of adaptive antibody response do not vary systematically with species body mass (Fig. 7.6).

We view our theory as a first step towards understanding inter-specific differences in the immune system. Such a theory could constitute a critical first step in translating experimental studies in model organisms to humans. Our modeling framework is adaptable and can incorporate new immunological findings as they become available. It can also be extended to investigate host immune responses in other multi-host pathogens. We also suggest that experimental data from multiple species, pooled and analyzed using hierarchical Bayesian models, can better inform translational models and may lead to more accurate predictions of clinical trial end outcomes like vaccine efficacy.

8.6 Implications for predicting spread of WNV

WNV infection progresses along multiple scales: infection within hosts is related to dynamics of WNV spread between hosts by mosquito vectors. Coupling two different processes over multiple scales, from individual cells to epidemic spread in bird populations, is extremely challenging and could yield valuable insights. Our model predicted host competency to infect mosquitoes can be coupled to models of WNV spread between multiple species. Such an approach would help link within-host WNV dynamics to dynamics between hosts and may help produce accurate estimates of spread of WNV.

8.7 Benefits of mathematical modeling

We have used many different mathematical models in our work: ordinary differential equations and agent-based models; target-cell limited models and adaptive immune response models; and multi-level and aggregated hierarchical models. These models encapsulate different assumptions about biological mechanisms and allow us to test the robustness of model predictions to these assumptions. Therefore it is striking that our models produce similar predictions, e.g. the target-cell limited and adaptive immune response models both predict that the rate of WNV production declines with species mass (Chapter 7, Table 7.1).

Our models deliberately simplify the vast complexities of the immune system. Nevertheless, these models reveal broad-scale patterns, e.g. the rate of adaptive immune response mediated virus clearance does not vary systematically with species mass (Chapter 7, Fig. 7.6). The tight coupling of our mathematical models to experimental data produces insights that neither could have provided in isolation.

8.8 Caveats and limitations

The immune system has diverse cell types that mount different responses against pathogens. We have investigated the effect of body size on the innate and adaptive antibody (IgM) response against WNV. Although we have not investigated T-cell responses in our models of WNV (since they appear much later in the course of infection), we have simulated T-cell responses in influenza infection. Our modeling suggests that T-cell search for influenza infected cells in lung are facilitated by chemokine signals in tissue. The speedup in search due to these signals is also higher in larger animals. However we predict that time to traffic a critical number of T-cells to infected tissue will scale with body size; the ODE model in Chapter 4 predicts

that the number of activated T-cells that arrive at the site of infection in mice after 5 days post infection is 80,000 whereas in humans the number is predicted to be 190 (Chapter 4, Table 4.2). This is roughly consistent with experimental data suggesting that T-cell responses to HIV infection in macaques take around 1 to 2 weeks [111, 112]. Adapting our T-cell recirculation model (Chapter 4) to make predictions for T-cell response times in humans is an interesting avenue for future work.

Finally, in some cases our hierarchical Bayesian models produce parameter estimates that appear to be biologically unreasonable, e.g. the production rate of WNV from infected cells (p) for some corvid species is predicted to be approximately 10^8 PFU day^{-1}, which is extremely high. This could be due to the fact that the initial susceptible cell population (T_0 in our models) is much higher in corvids, and may suggest that other cell types are also available for infection. Further experimental data on the susceptible cell population in corvid species may lead to more realistic estimates of the production rate (since these two parameters are correlated in our models).

8.9 Concluding remarks

Ultimately, this thesis represents a first step towards an empirical scaling theory of the immune system. The mathematical framework presented here is an approach to uncover systematic differences in disease progression and immune response in animals that differ in body mass and phylogeny. There is potential for substantial impact on human health since mice are the principal model organisms for most immunological experiments. This could be extended to understand how drug and vaccine efficacy differ between humans and model organisms like mice.

Appendices

Appendix A

Bayesian Aggregated Model

The aggregated model has individuals of different species. The individuals are aggregated to form a tree of height 2. The model is shown graphically in Fig. 6.2 (Left panel).

We denote the number of individuals by n and the number of experimental measurements of virus concentration on the ith individual by m_i. $y_{ij}(t_j)$ represents the experimental measurements of logarithmic virus concentration in serum for the ith individual at times $t_j (j = 1, 2, 3, ..., m_i)$. For notational convenience, let $\mu = (log_{10}V_{dose}, log_{10}a, log_{10}M)^T$, $\theta_i = (log_{10}V_{0i}, log_{10}a_i, log_{10}M_i)^T$ (for the proof of concept model, Chapter 6), $\Theta = \{\theta_i, i = 1..n\}$, $Y = \{y_{ij}, i = 1..n, j = 1..m_i\}$ and $f_{ij}(\theta_i, t_j) = log_{10}V_{ij}(\theta_i, t_j)$ where $V_{ij}(\theta_i, t_j)$ denotes the numerical solution for $V(t)$ in Eq. (6.2) for the ith individual at time t_j.

The Bayesian non-linear mixed effects aggregated model can be written as the following three stages [113]:

1. Within-individual variation

$$[y_i|\theta_i, \sigma^2] \sim Normal(f_i(\theta_i), \sigma^2) \tag{A.1}$$

2. Between-individual variation

$$[\theta_i|\mu, \Sigma] \sim Normal(\mu, \Sigma) \tag{A.2}$$

3. Prior distributions

$$\sigma^{-2} \sim Gamma(a, b), \Sigma^{-1} \sim Wishart(\Omega, \nu), \mu \sim Normal(\eta, \Lambda) \tag{A.3}$$

The Normal, Wishart and Gamma distributions are chosen to simplify calculations [113, 114].

The full conditional distributions for θ_i, σ^{-2}, μ and Σ^{-1} can be written as [113, 114]:

$$\left[\theta_i|\sigma^{-2}, \mu, \Sigma, \eta, \Theta, Y\right] \propto exp\left(-\frac{\sigma^{-2}}{2}\sum_{j=1}^{m_i}[y_{ij} - f_{ij}(\theta_i, t_j)]^2 - \frac{1}{2}(\theta_i - \mu)^T\Sigma^{-1}(\theta_i - \mu)\right) \tag{A.4}$$

$$\left[\sigma^{-2}|\mu, \Sigma, \Theta, Y\right] \sim Gamma\left(a + \frac{\sum_{i=1}^{n} m_i}{2}, A^{-1}\right) \tag{A.5}$$

$$\left[\mu|\sigma^{-2}, \Sigma, \Theta, Y\right] \sim Normal\left(B^{-1}C, B^{-1}\right) \tag{A.6}$$

$$\left[\Sigma^{-1}|\sigma^{-2},\mu,\Theta,Y\right] \sim Wishart\left(D^{-1},n+\nu\right) \tag{A.7}$$

where $A = b^{-1} + \frac{1}{2}\sum_{i=1}^{n}\sum_{j=1}^{m_i}\left[y_{ij} - f_{ij}(\theta_i,t_j)\right]^2$, $B = n\Sigma^{-1} + \Lambda^{-1}$, $C = \Sigma^{-1}\sum_{i=1}^{n}\theta_i + \Lambda^{-1}\eta$ and $D = \Omega^{-1} + \sum_{i=1}^{n}(\theta_i - \mu)\cdot(\theta_i - \mu)^T$.

The priors for the model were provided in the following manner - Ω was initialized with the variance from the simulated data (all individuals aggregated),and the initial guess for θ was randomly generated from the top level distribution, $N(\eta,\Lambda)$ (same for the multi-level model). The inference process produces separate estimates of (V_{dose},a,M) even though these estimates are correlated with each other.

Appendix B

Bayesian Multi-level Model

The multi-level hierarchical model has groups (species) with individuals in each group. The groups are arranged hierarchically to form a tree of height 3. The model is shown graphically in Fig. 6.3 (Left panel). Let there be m distinct species indexed by k and the number of individuals in the kth group is represented by n_k. Let us represent the number of experimental measurements on the ith individual of the kth species by m_{ik}. $y_{ijk}(t_j)$ represents the experimental measurements of logarithmic virus concentration in serum for the ith individual belonging to the kth species at times $t_j (j = 1, 2, 3, ..., m_{ik})$.

For notational convenience, we define the individual level distribution (ith individual belonging to the kth species) by $\theta_{ik} = (log_{10}V_{0ik}, log_{10}a_{ik}, log_{10}M_{ik})^T$ (for the proof of concept model, Chapter 6). We define the kth species level distribution by $\mu_k = (log_{10}V_{dose,k}, log_{10}a_k, log_{10}M_k)^T$ and the genus level distribution by $\eta = (log_{10}V_0, log_{10}a, log_{10}M)^T$.

Let $\Theta = \{\theta_{ik}, i = 1..n_k, k = 1..m\}$, $Y = \{y_{ijk}, i = 1..n_k, j = 1..m_{ik}, k = 1..m\}$ and $f_{ijk}(\theta_{ik}, t_j) = log_{10}V_{ijk}(\theta_{ik}, t_j)$ where $V_{ijk}(\theta_{ik}, t_j)$ denotes the numerical solution for $V(t)$ in Eq. (6.2) for the ith individual (belonging to the kth species) at time t_j.

We write this Bayesian non-linear mixed effects multi-level model as the following four stages:

1. Within-individual variation

$$[y_{ik}|\theta_{ik}, \sigma_k^2] \sim Normal(f_{ik}(\theta_{ik}), \sigma_k^2) \tag{B.1}$$

for the ith individual belonging to the kth species.

2. Between-individual variation

$$[\theta_{ik}|\mu_k, \Sigma_k] \sim Normal(\mu_k, \Sigma_k) \tag{B.2}$$

3. Between species variation

$$\sigma_k^{-2} \sim Gamma(a, b), \Sigma_k^{-1} \sim Wishart(\Omega, \nu), \mu_k \sim Normal(\eta, \Lambda) \tag{B.3}$$

for the kth species. The Normal, Wishart and Gamma distributions are chosen to simplify calculations.

4. Genus level prior distributions

$$\eta \sim Normal(x, y), \Lambda^{-1} \sim Wishart(p, q) \tag{B.4}$$

Fig. 6.3 (right panel) represents these equations graphically in a plate diagram. In a graphical model like Fig. 6.3 (right panel), for any node u, we can represent the remaining nodes by U_{-u} and the full conditional distribution $P(u, U_{-u})$ is

$\propto P(u|parents[u]) \cdot \prod_{w \in children[u]} P(w|parents[w])$ [107]. The full conditional distribution for u contains a prior component (from the parents of u) and a likelihood component (from each child of u).

Following the principle above and simplifying, we derived the full conditional distributions for θ_{ik}, σ_k^{-2}, μ_k, Σ_k^{-1}, η and Λ^{-1}:

$$\begin{aligned}\left[\theta_{ik}|\sigma_k^{-2}, \mu_k, \Sigma_k, \eta, \Lambda^{-1}, \Theta, Y\right] \propto exp\Bigg(& -\frac{\sigma_k^{-2}}{2} \sum_{j=1}^{m_{ik}} \left[y_{ijk} - f_{ijk}(\theta_{ik}, t_j)\right]^2 \\ & -\frac{1}{2}(\theta_{ik} - \mu_k)^T \Sigma_k^{-1} (\theta_{ik} - \mu_k)\end{aligned} \tag{B.5}$$

$$\left[\sigma_k^{-2}|\mu_k, \Sigma_k, \eta, \Lambda^{-1}, \Theta, Y\right] \sim Gamma\left(a + \frac{\sum_{i=1}^{n} m_{ik}}{2}, A_k^{-1}\right) \tag{B.6}$$

$$\left[\mu_k|\sigma_k^{-2}, \Sigma_k, \eta, \Lambda^{-1}, \Theta, Y\right] \sim Normal\left(B_k^{-1} C_k, B_k^{-1}\right) \tag{B.7}$$

$$\left[\Sigma_k^{-1}|\sigma_k^{-2}, \mu_k, \eta, \Lambda^{-1}, \Theta, Y\right] \sim Wishart\left(D_k^{-1}, n_k + \nu\right) \tag{B.8}$$

$$\left[\eta|\sigma_k^{-2}, \mu_k, \Sigma_k^{-1}, \Lambda^{-1}, \Theta, Y\right] \sim Normal\left(z, Z\right) \tag{B.9}$$

$$\left[\Lambda^{-1}|\sigma_k^{-2}, \mu_k, \Sigma_k^{-1}, \eta, \Theta, Y\right] \sim Wishart\left(E, q + m\right) \tag{B.10}$$

where $A_k = b^{-1} + \frac{1}{2}\sum_{i=1}^{n_k}\sum_{j=1}^{m_{ik}}\left[y_{ijk} - f_{ijk}(\theta_{ik}, t_j)\right]^2$, $B_k = n_k\Sigma_k^{-1} + \Lambda^{-1}$, $C_k = \Sigma_k^{-1}\sum_{i=1}^{n_k}\theta_{ik} + \Lambda^{-1}\eta$, $D_k = \Omega^{-1} + \sum_{i=1}^{n_k}(\theta_{ik} - \mu_k)\cdot(\theta_{ik} - \mu_k)^T$, $Z = (U^{-1} + y^{-1})^{-1}$, $z = Z\,(U^{-1}u + y^{-1}x)$ and $E^{-1} = p^{-1} + \sum_{k=1}^{m}(\mu_k - \eta)\cdot(\mu_k - \eta)^T$.

The priors for the model were provided in the following manner - the initial guess for μ came from the generated data; Ω was initialized with the within group standard deviation from generated data, and the initial guess for θ was randomly generated from the top level distribution, $N(\eta, \Lambda)$ (same for the aggregated model).

The code for both the aggregated and multi-level model implementations is available online [33].

References

[1] N. Komar, S. Langevin, S. Hinten, N. Nemeth, E. Edwards, D. Hettler, B. Davis, R. Bowen, and M. Bunning, *Experimental infection of North American birds with the New York 1999 strain of West Nile Virus*, Emerging Infectious Diseases **9** (2003), 311–322.

[2] M. Bunning, R. Bowen, C. Cropp, K. Sullivan, B. Davis, N. Komar, M. Godsey, D. Baker, D. Hettler, D. Holmes, B. Biggerstaff, and C. Mitchell, *Experimental infection of horses with West Nile Virus*, Emerging Infectious Diseases **8** (2002), 380–386.

[3] L. Austgen, R. Bowen, M. Bunning, B. Davis, C. Mitchell, and G. Chang, *Experimental infection of cats and dogs with West Nile Virus*, Emerging Infectious Diseases **10** (2004), 82–86.

[4] L. Styer, K. Kent, R. Albright, C. Bennett, L. Kramer, and K. Bernard, *Mosquitoes inoculate high doses of West Nile virus as they probe and feed on live hosts*, PLoS Pathog **3** (2007), e132.

[5] N. Komar, S. Langevin, S. Hinten, N. Nemeth, E. Edwards, D. Hettler, B. Davis, R. Bowen, and M. Bunning, *Experimental infection of North American birds with the New York 1999 strain of West Nile virus.*, Emerg Infect Dis **9** (2003), 311–22.

[6] F. W. Wiegel and A. Perelson, *Some scaling principles for the immune system*, Immunology and Cell Biology **82** (2004), 127–131.

[7] P. Altman and D. Dittmer, *Biology data book*, Federation of American Societies for Experimental Biology, Bethesda, MD, 1974.

[8] M. Woolhouse, L. Taylor, and D. Haydon, *Population biology of multihost pathogens*, Science **292** (2001), 1109–1112.

[9] J. Cable, B. Enquist, and M. Moses, *The allometry of host-pathogen interactions*, PLoS ONE **2**.

[10] D. Grace, F. Mutua, P. Ochungo, R. Kruska, K. Jones, L. Brierley, L. Lapar, M. Said, M. Herrero, P. Phuc, et al., *Mapping of poverty and likely zoonoses hotspots: Report to the department for international development.*

[11] G. West, J. Brown, and B. Enquist, *A general model for the origin of allometric scaling laws in biology*, Science **276** (1997), 122–126.

[12] J. H. Brown, J. F. Gillooly, A. P. Allen, V. M. Savage, and G. B. West, *Toward a metabolic theory of ecology*, Ecology **85** (2004), 1771–1789.

[13] J. Rouder, J. Lu, and P. Speckman, *A hierarchical model for estimating response time distributions*, Psychonomic Bulletin & Review **12** (2005), 195–223.

[14] L. Fei-Fei and P. Perona, *A bayesian hierarchical model for learning natural scene categories*, in Computer Vision and Pattern Recognition, 2005. CVPR 2005. IEEE Computer Society Conference on, Vol. 2 IEEE, 2005, pp. 524–531.

[15] C. Wikle, *Hierarchical bayesian models for predicting the spread of ecological processes*, Ecology **84** (2003), 1382–1394.

[16] C. Wikle, L. Berliner, and N. Cressie, *Hierarchical bayesian space-time models*, Environmental and Ecological Statistics **5** (1998), 117–154.

[17] Y. Huang, D. Liu, and H. Wu, *Hierarchical Bayesian methods for estimation of parameters in a longitudinal HIV dynamic system.*, Biometrics **62** (2006), 413–23.

[18] C. Han, K. Chaloner, and A. Perelson, *Bayesian analysis of a population hiv dynamic model*, Lecture Notes in Statistics, New York, Springer Verlag.

[19] L. Canini and F. Carrat, *Population modeling of influenza A/H1N1 virus kinetics and symptom dynamics.*, Journal of Virology **85** (2011), 2764–70.

[20] C. Beauchemin and A. Handel, *A review of mathematical models of influenza a infections within a host or cell culture: lessons learned and challenges ahead*, BMC Public Health **11** (2011), S7.

[21] E. B. Hayes, N. Komar, R. S. Nasci, S. P. Montgomery, D. R. O'Leary, and G. L. Campbell, *Epidemiology and transmission dynamics of West Nile virus disease.*, Emerg Infect Dis **11** (2005), 1167–73.

[22] E. Deardorff, J. Franco, A. Brault, R. Lopez, A. Cortes, P. Ramirez, M. Hernandez, W. Ramey, C. Davis, D. W. Beasley, R. B. Tesh, A. D. Barrett, and S. C. Weaver, *Introductions of West Nile virus strains to Mexico*, Emerg Infect Dis **12** (2006), 314–318.

[23] N. Komar and G. G. Clark, *West Nile virus activity in Latin America and the Caribbean.*, Rev Panam Salud Publica **19** (2006), 112–7.

[24] R. S. Lanciotti, J. T. Roehrig, V. Deubel, J. Smith, M. Parker, K. Steele, B. Crise, K. E. Volpe, M. B. Crabtree, J. H. Scherret, R. A. Hall, J. S. MacKenzie, C. B. Cropp, B. Panigrahy, E. Ostlund, B. Schmitt, M. Malkinson, C. Banet, J. Weissman, N. Komar, H. M. Savage, W. Stone, T. McNamara, and D. J. Gubler, *Origin of the West Nile virus responsible for an outbreak of encephalitis in the northeastern United States.*, Science **286** (1999), 2333–7.

[25] M. A. Samuel and M. S. Diamond, *Pathogenesis of West Nile virus infection : a balance between virulence, innate and adaptive immunity, and viral evasion*, Journal of Virology **80** (2006), 9349–9360.

[26] S. Banerjee and M. Moses, *Scale Invariance of Immune System Response Rates and Times: Perspectives on Immune System Architecture and Implications for Artificial Immune Systems*, Swarm Intelligence **4** (2010), 301–318.

[27] S. Banerjee, D. Levin, F. Koster, S. Forrest, and M. Moses, *The Value of Inflammatory Signals in Adaptive Immune Responses*, in P. Lio et al. (Eds.) Artificial Immune Systems, 10th International Conference, ICARIS 2011, Lecture Notes in Computer Science, Vol. 6825, Springer Verlag, Berlin, Germany, 2011, pp. 1–14.

[28] S. Banerjee, J. Guedj, R. Ribeiro, M. E. Moses, and A. S. Perelson, *Towards a quantitative understanding of within-host dynamics of West Nile Virus infection.*, in preparation.

[29] C. Warrender, *Modeling intercellular interactions in the peripheral immune system*, PhD thesis, University of New Mexico, 2004.

[30] ——— *CyCells (Open source software)* http://sourceforge.net/projects/cycells, 2003.

[31] The MathWorks Inc. *MATLAB version 7.13.0.564*, 2011.

[32] R. I. Macey and G. Oster *Berkeley Madonna, version 8.0.* Technical report, University of California, Berkeley, California, 2001.

[33] S. Banerjee *Tools for Analysis and Modeling using Differential Equations and Hierarchical Bayesian Models Applied to Within-Host Viral Dynamics Models (Open source software)* https://sites.google.com/site/neelsoumya/software, 2013.

[34] L. Styer, K. Kent, R. Albright, C. Bennett, L. Kramer, and K. Bernard, *Mosquitoes inoculate high doses of West Nile virus as they probe and feed on live hosts*, PLoS Pathogens **3**.

[35] C. Janeway, P. Travers, M. Walport, and M. Shlomchik, *Immunobiology: The immune system in health and disease*, Garland Science, New York, NY, 2005.

[36] A. Soderberg, G. Payne, A. Sato, R. Medzhitov, S. Segal, and A. Iwasaki, *Innate control of adaptive immunity via remodeling of lymph node feed arteriole*, Proceedings of the National Academy of Sciences **102** (2005), 16315–16320.

[37] C. Jarque and A. Bera, *A test for normality of observations and regression residuals*, International Statistical Review **55** (1987), 163–172.

[38] S. Banerjee and M. Moses, *A hybrid agent based and differential equation model of body size effects on pathogen replication and immune system response*, in P.S. Andrews et al. (Eds.) Artificial Immune Systems, 8th International Conference, ICARIS 2009, Lecture Notes in Computer Science, Vol. 5666, Springer Verlag, Berlin, Germany, 2009, pp. 14–18.

[39] M. Diamond, E. Sitati, L. Friend, S. Higgs, B. Shrestha, and M. Engle, *A critical role for induced IgM in the protection against West Nile Virus infection*, Journal of Experimental Medicine **198** (2003), 1853–1862.

[40] M. Miller, A. Hejazi, S. Wei, M. Cahalan, and I. Parker, *T cell repertoire scanning is promoted by dynamic dendritic cell behavior and random T cell motility in the lymph node*, Proceedings of the National Academy of Sciences **101** (2004), 998–1003.

[41] G. Amdahl, *Validity of the single processor approach to achieving large-scale computing capabilities*, in AFIPS '67 (Spring): Proceedings of the April 18-20, 1967, Spring Joint Computer Conference, ACM, New York, NY, USA, 1967, pp. 483–485.

[42] C. Halin, R. M. J., C. Sumen, and U. H. von Andrian, *In vivo imaging of lymphocyte trafficking*, Annual Review of Cell and Developmental Biology **21** (2005), 581–603.

[43] T. Hildebrandt, R. Hermes, P. Ratanakorn, W. Rietschel, J. Fickel, R. Frey, G. Wibbelt, C. Reid, and F. Goritz, *Ultrasonographic assessment and ultra-sound guided biopsy of the retropharyngeal lymph nodes in Asian elephants (Elephas maximus)*, Veterinary Record **157** (2005), 544–548.

[44] M. Cohn and R. Langman, *The Protecton: the evolutionarily selected unit of humoral immunity*, Immunological Reviews **115** (1990), 9–147.

[45] J. Banchereau and R. Steinman, *Dendritic cells and the control of immunity*, Nature **392** (1998), 245–252.

[46] I. J. M. de Vries, D. J. E. B. Krooshoop, N. M. Scharenborg, W. J. Lesterhuis, J. H. S. Diepstra, G. N. P. van Muijen, S. P. Strijk, T. J. Ruers, O. C. Boerman, and W. J. G. Oyen, *Effective migration of antigen-pulsed dendritic cells to lymph nodes in melanoma patients is determined by their maturation state*, Cancer Research **63** (2003), 12–17.

[47] R. Peters, *The ecological implications of body size*, Cambridge University Press, Cambridge, 1983.

[48] M. Bajenoff, J. Egen, H. Qi, A. Huang, F. Castellino, and R. Germain, *Highways, byways and breadcrumbs: Directing lymphocyte traffic in the lymph node*, Trends in Immunology **28** (2007), 346–352.

[49] A. Itano and M. Jenkins, *Antigen presentation to nave CD4 T cells in the lymph node*, Nature Immunology **4** (2003), 733–739.

[50] A. Perelson and F. Wiegel, *Scaling aspects of lymphocyte trafficking*, Journal of Theoretical Biology **257** (2009), 9–16.

[51] J. Kleinberg, *Computing: The wireless epidemic*, Nature **449** (2007), 287–288.

[52] J. Timmis, E. Hart, A. Hone, M. Neal, A. Robins, S. Stepney, and A. Tyrrell, *Immuno-engineering*, Vol. 268, Springer US, 2008.

[53] S. Nair and W. Godfrey, *An immune system based multi-robot mobile agent network*, in P.J. Bentley et al. (Eds.) Artificial Immune Systems, 7th International Conference, ICARIS 2008, Lecture Notes in Computer Science, Vol. 5132, Springer Verlag, Berlin, Germany, 2008, pp. 424–433.

[54] S. Banerjee and M. Moses, *Modular RADAR: An immune system inspired search and response strategy for distributed systems*, in E. Hart et al. (Eds.) Artificial Immune Systems, 9th International Conference, ICARIS 2010, Lecture Notes in Computer Science, Vol. 6209, Springer Verlag, Berlin, Germany, 2010, pp. 116–129.

[55] ———, *A Hybrid Agent Based and Differential Equation Model of Body Size Effects on Pathogen Replication and Immune System Response*, in P.S. Andrews et al. (Eds.) Artificial Immune Systems, 8th International Conference, ICARIS 2009, Lecture Notes in Computer Science, Vol. 5666, 2009, pp. 14–18.

[56] E. R. Weibel, *Scaling of structural and functional variables in the respiratory system*, Annual Review of Physiology **49** (1987), 147–159.

[57] M. Moses and S. Banerjee, *Biologically Inspired Design Principles for Scalable, Robust, Adaptive, Decentralized Search and Automated Response (RADAR)*, in IEEE Symposium Series in Computational Intelligence 2011 (SSCI 2011), 2011.

[58] T. Paz, K. Letendre, W. Burnside, G. Fricke, and M. Moses, *How Ants Turn Information into Food*, in IEEE Symposium Series in Computational Intelligence 2011 (SSCI 2011), 2011.

[59] N. La Gruta and P. Doherty, *Influenza Virology Current Topics*, Caister Academic Press, 2006, Chap. Quantitative and qualitative characterization of the CD8+ T cell response to influenza virus infection.

[60] R. Saenz et al., *Dynamics of Influenza Virus Infection and Pathology*, Journal of Virology **84** (2010), 3974–3983.

[61] B. Moser and P. Loetscher, *Lymphocyte Traffic Control by Chemokines*, Nature Immunology **2** (2001), 123–128.

[62] H. Miao, J. Hollenbaugh, M. Zand, W. Holden, T. Mosmann, A. Perelson, H. Wu, and D. Topham, *Quantifying the Early Immune Response and Adaptive Immune Response Kinetics in Mice Infected with Influenza A Virus*, Journal of Virology **84** (2010), 6687–6698.

[63] C. Beauchemin, N. Dixit, and A. Perelson, *Characterizing T Cell Movement within Lymph Nodes in the Absence of Antigen*, The Journal of Immunology **178** (2007), 5505–5512.

[64] W. Calder, *Size, Function and Life History*, Dover Publications, 1984.

[65] H. Mitchell, D. Levin, S. Forrest, C. Beauchemin, J. Tipper, J. Knight, N. Donart, R. Layton, J. Pyles, P. Gao, K. Harrod, A. Perelson, and F. Koster, *Higher replication efficiency of 2009 (h1n1) pandemic influenza than seasonal and avian strains: kinetics from epithelial cell culture and computational modeling*, Journal of Virology **85** (2010), 1125–1135.

[66] E. Ceauu, S. Ercoiu, P. Calistru, D. Ispas, O. Dorob, M. Homo, C. Brbulescu, I. Cojocaru, C. V. Simion, C. Cristea, C. Oprea, C. Dumitrescu, D. Duiculescu, I. Marcu, C. Mociorni, T. Stoicev, I. Zolotuca, C. Calomfirescu, R. Rusu, R. Hodrea, S. Geamai, and L. Pun, *Clinical manifestations in the West Nile virus outbreak.*, Rom J Virol **48** (1997), 3–11.

[67] L. R. Petersen and A. A. Marfin, *West Nile virus: a primer for the clinician*, Ann Intern Med **137** (2002), 173–179.

[68] J. J. Sejvar, M. B. Haddad, B. C. Tierney, G. L. Campbell, A. A. Marfin, J. A. Van Gerpen, A. Fleischauer, A. A. Leis, D. S. Stokic, and L. R. Petersen, *Neurologic manifestations and outcome of West Nile virus infection.*, J Am Med Assoc **290** (2003), 511–5.

[69] A. M. Kilpatrick, *Globalization, land use, and the invasion of West Nile virus.*, Science **334** (2011), 323–7.

[70] K. C. Smithburn, R. M. Taylor, F. Rizk, and A. Kader, *Immunity to certain arthropod-borne viruses among indigenous residents of Egypt*, Am J Trop Med Hyg **3** (1954), 9–18.

[71] M. S. Diamond, E. M. Sitati, L. D. Friend, S. Higgs, B. Shrestha, and M. Engle, *A critical role for induced IgM in the protection against West Nile virus infection.*, J Exp Med **198** (2003), 1853–62.

[72] C. Ye, S. Abraham, H. Wu, P. Shankar, and N. Manjunath, *Silencing early viral replication in macrophages and dendritic cells effectively suppresses flavivirus encephalitis*, PloS One **6** (2011), e17889.

[73] M. S. Diamond, B. Shrestha, A. Marri, D. Mahan, and M. Engle, *B cells and antibody play critical roles in the immediate defense of disseminated infection by West Nile encephalitis virus*, Journal of Virology **77** (2003), 2578–2586.

[74] B. Shrestha and M. Diamond, *Role of CD8+ T cells in control of West Nile virus infection*, Journal of Virology **78** (2004), 8312–8321.

[75] D. D. Ho, A. U. Neumann, A. S. Perelson, W. Chen, J. M. Leonard, and M. Markowitz, *Rapid turnover of plasma virions and CD4 lymphocytes in HIV-1 infection.*, Nature **373** (1995), 123–6.

[76] A. S. Perelson, D. E. Kirschner, and R. De Boer, *Dynamics of HIV infection of CD4+ T cells.*, Math Biosci **114** (1993), 81–125.

[77] A. S. Perelson, A. U. Neumann, M. Markowitz, J. M. Leonard, and D. D. Ho, *HIV-1 dynamics in vivo: virion clearance rate, infected cell life-span, and viral generation time*, Science **271** (1996), 1582–1586.

[78] A. S. Perelson, P. Essunger, Y. Cao, M. Vesanen, A. Hurley, K. Saksela, M. Markowitz, and D. D. Ho, *Decay characteristics of HIV-1-infected compartments during combination therapy.*, Nature **387** (1997), 188–91.

[79] N. Dixit, J. Layden-Almer, and T. Layden, *Modelling how ribavirin improves interferon response rates in hepatitis C virus infection*, Nature **432** (2004), 922–924.

[80] A. U. Neumann, N. P. Lam, H. Dahari, M. Davidian, T. E. Wiley, B. P. Mika, A. S. Perelson, and T. J. Layden, *Differences in viral dynamics between genotypes 1 and 2 of hepatitis C virus.*, J Infect Dis **182** (2000), 28–35.

[81] A. U. Neumann, N. P. Lam, H. Dahari, D. R. Gretch, T. E. Wiley, T. J. Layden, and A. S. Perelson, *Hepatitis C viral dynamics in vivo and the antiviral efficacy of interferon-alpha therapy.*, Science **282** (1998), 103–7.

[82] M. Tsiang, J. F. Rooney, J. J. Toole, and C. S. Gibbs, *Biphasic clearance kinetics of hepatitis B virus from patients during adefovir dipivoxil therapy.*, Hepatology **29** (1999), 1863–9.

[83] M. Nowak, S. Bonhoeffer, A. Hill, R. Boehme, H. Thomas, and H. McDade, *Viral dynamics in hepatitis B virus infection.*, Proc Natl Acad Sci USA **93** (1996), 4398–402.

[84] S. R. Lewin, R. M. Ribeiro, T. Walters, G. K. Lau, S. Bowden, S. Locarnini, and a. S. Perelson, *Analysis of hepatitis B viral load decline under potent therapy: complex decay profiles observed.*, Hepatology **34** (2001), 1012–20.

[85] P. Baccam, C. Beauchemin, C. Macken, F. Hayden, and A. Perelson, *Kinetics of influenza A virus infection in humans*, Journal of Virology **80** (2006), 7590–7599.

[86] A. M. Smith and A. S. Perelson, *Influenza A virus infection kinetics: quantitative data and models.*, Wiley Interdiscip Rev Syst Biol Med **3** (2011), 429–45.

[87] C. A. A. Beauchemin and A. Handel, *A review of mathematical models of influenza A infections within a host or cell culture : lessons learned and challenges ahead*, BMC Public Health **11** (2011), S7.

[88] S. Halstead, C. Venkateshan, M. Gentry, and L. Larsen, *Heterogeneity of infection enhancement of dengue 2 strains by monoclonal antibodies*, Journal of Immunology **132** (1984), 1529–1532.

[89] P. Marti, S. R. Ruiz, G. Marti, F. Anjuère, H. H. Vargas, M. López-bravo, and C. Ardavi, *Dramatic increase in lymph node dendritic cell number during infection by the mouse mammary tumor virus occurs by a CD62L-dependent blood-borne DC recruitment*, Blood **99** (2002), 1282–1288.

[90] W. Purtha, K. Chachu, H. Virgin, and M. S. Diamond, *Early B-cell activation after West Nile virus infection requires alpha/beta interferon but not antigen receptor signaling*, Journal of Virology **82** (2008), 10964–10974.

[91] M. C.-J. Cheeran, S. Hu, W. S. Sheng, A. Rashid, P. K. Peterson, and J. R. Lokensgard, *Differential responses of human brain cells to West Nile virus infection.*, J Neurovirol **11** (2005), 512–24.

[92] M. Stafford, Y. Cao, D. Ho, and L. Corey, *Modeling plasma virus concentration and CD4+ T cell kinetics during primary HIV infection*, J Theor Biol **203** (2000), 285–301.

[93] M. S. Diamond, B. Shrestha, and E. Mehlhop, *Innate and adaptive immune responses determine protection against disseminated infection by West Nile encephalitis virus*, Viral Immunol **16** (2003), 259–278.

[94] P.-Y. Lim, M. J. Behr, C. M. Chadwick, P.-Y. Shi, and K. A. Bernard, *Keratinocytes are cell targets of West Nile virus in vivo.*, Journal of Virology **85** (2011), 5197–201.

[95] W. Van den Broeck, A. Derore, and P. Simoens, *Anatomy and nomenclature of murine lymph nodes: descriptive study and nomenclatory standardization in BALB/cAnNCrl mice.*, J Immunol Methods **312** (2006), 12–9.

[96] A. C. Riches, J. G. Sharp, D. B. Thomas, and S. V. Smith, *Blood volume determination in the mouse.*, J Physiol **228** (1973), 279–84.

[97] D. E. Wilson and S. Ruff, *The Smithsonian book of North American mammals*, Smithsonian Institution Press, Washington, D.C., USA., 1999.

[98] J. J. H. Chu and M. Ng, *The mechanism of cell death during West Nile virus infection is dependent on initial infectious dose*, J Gen Virol **84** (2003), 3305–3314.

[99] M. Nowak and R. M. May, *Virus dynamics: mathematical principles of immunology and virology*, Oxford University Press on Demand, 2000.

[100] M. C. Parquet, A. Kumatori, F. Hasebe, K. Morita, and A. Igarashi, *West Nile virus-induced bax-dependent apoptosis.*, FEBS Lett **500** (2001), 17–24.

[101] B. Shrestha, D. Gottlieb, and M. S. Diamond, *Infection and injury of neurons by West Nile encephalitis virus*, Journal of Virology **77** (2003), 13203–13213.

[102] A. M. Smith, F. R. Adler, J. L. McAuley, R. N. Gutenkunst, R. M. Ribeiro, J. a. McCullers, and A. S. Perelson, *Effect of 1918 PB1-F2 expression on influenza A virus infection kinetics.*, PLoS Comput Biol **7** (2011), e1001081.

[103] B. Hancioglu, D. Swigon, and G. Clermont, *A dynamical model of human immune response to influenza A virus infection.*, J Theor Biol **246** (2007), 70–86.

[104] H. Dahari, R. M. Ribeiro, C. M. Rice, and A. S. Perelson, *Mathematical modeling of subgenomic hepatitis C virus replication in Huh-7 cells.*, Journal of Virology **81** (2007), 750–60.

[105] G. Ludwig, P. Calle, J. Mangiafico, B. Raphael, D. Danner, J. Hile, T. Clippinger, J. Smith, R. Cook, and T. McNamara, *An outbreak of west nile virus in a new york city captive wildlife population.*, The American journal of tropical medicine and hygiene **67** (2002), 67–75.

[106] B. Carlin and T. Louis, *Bayes and empirical bayes methods for data analysis*, Statistics and Computing **7** (1997), 153–154.

[107] W. Gilks, S. Richardson, and D. Spiegelhalter, *Markov Chain Monte Carlo in practice: interdisciplinary statistics*, Vol. 2, Chapman & Hall/CRC, 1995.

[108] A. Gelfand and A. Smith, *Sampling-based approaches to calculating marginal densities*, Journal of the American statistical association **85** (1990), 398–409.

[109] K. Brown and J. Sethna, *Statistical mechanical approaches to models with many poorly known parameters*, Physical Review E **68** (2003), 1–9.

[110] R. N. Gutenkunst, J. J. Waterfall, F. P. Casey, K. S. Brown, C. R. Myers, and J. P. Sethna, *Universally sloppy parameter sensitivities in systems biology models.*, PLoS Computational Biology **3** (2007), 1871–78.

[111] M. P. Davenport, R. M. Ribeiro, D. L. Chao, and A. S. Perelson, *Predicting the impact of a nonsterilizing vaccine against human immunodeficiency virus*, Journal of Virology **78** (2004), 11340–11351.

[112] R. J. De Boer and A. S. Perelson, *Quantifying t lymphocyte turnover*, Journal of theoretical biology.

[113] M. Davidian and D. Giltinan, *Nonlinear models for repeated measurement data*, Vol. 62, Chapman & Hall/CRC, 1995.

[114] A. Gelfand, S. Hills, A. Racine-Poon, and A. Smith, *Illustration of bayesian inference in normal data models using gibbs sampling*, Journal of the American Statistical Association **85** (1990), 972–985.